

Polarizability effects due to low-energy enhancement of the gamma-strength function

Cebo Ngwetsheni



UNIVERSITY *of the*
WESTERN CAPE

A thesis is submitted in fulfillment of the requirements of the Masters in Science degree in the Department of Physics and Astronomy, University of the Western Cape.

supervised by:
Prof. J.N. Orce, University of the Western Cape.
March 18, 2019

Declaration

I declare that *Polarizability effects due to low-energy enhancement of the gamma-strength function* is my own work, that it has not been submitted for any degree or examination in any other university, and that all the sources I have used or quoted have been indicated and acknowledged by complete references.

Full name : Ngwetsheni Cebo

Signed :



Date : 26 November 2018

1



¹email: 3344489@myuwc.ac.za
web: nuclear.uwc.ac.za

Abstract

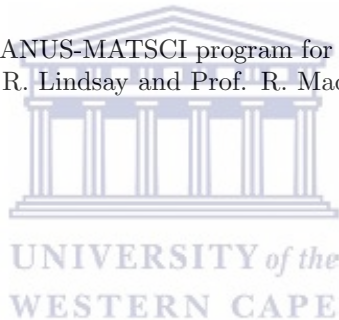
The nuclear dipole polarizability is mainly governed by the dynamics of the isovector giant dipole resonance. An additional contribution may, arise from the effect of the recently observed enhancement of the photon strength function at low energies for nuclides in the $A \approx 50, 90$ mass regions. Empirical drops observed from photoabsorption cross section measurements in ground-state nuclear polarizabilities indicate deviations from the effect of giant dipole resonances and reveal the presence of shell effects in semi-magic nuclei with neutron magic numbers $N = 50, 82$ and 126 . Similar drops of polarizability in the quasi-continuum of nuclei with, or close to, magic numbers $N = 28, 50$ and 82 , reflect the continuing influence of shell closures up to the nucleon separation energy. These findings are presented for the first time in this work and strongly support recent large-scale shell-model calculations in the quasi-continuum region describing the origin of the low-energy enhancement of the radiative or photon strength function as induced paramagnetism, and assert the Brink-Axel hypothesis as more universal than originally expected.



Acknowledgement

I would like to express my sincere gratitude towards,

- Prof. J.N. Orce “*mi amigo*”, for continuous guidance and support throughout this work. Looking forward to working with you on another project.
- My parents, Mr Z.A. Ngwetsheni (*Ahh.. Mbona! Tshay'ingwe!*) and Mrs F.E. Ngwetsheni (*Mamzondi! Yirhakazi!*), for encouragement and support throughout my studies.
- My family and friends, the long hours spent at the mysterious lab have finally payed off.
- My dearest, Sinegugu (*Mamthembu!*), for motivation and support.
- Dr. A. Pastore, for helpful advices and discussion.
- The UWC Coulex group, *Warriors!*, you have made this learning curve much smoother.
- Lastly, the NRF MANUS-MATSCI program for financial support offered. Particularly, Prof. R. Lindsay and Prof. R. Madjoe as representatives of the program.



Contents

1	Introduction	1
1.1	Scientific Motivation	2
2	Theory and Literature Review	9
2.1	Giant Resonances	9
2.1.1	Damping of giant resonances	14
2.1.2	Photon Strength Functions	15
2.1.3	GDR Models	16
2.2	Nuclear Polarizability	18
2.2.1	The S.H.O. model of polarizability	19
2.2.2	Quantum mechanical polarizability	21
2.2.3	Hydrodynamic polarizability	24
2.2.4	Polarizability and Deformation	25
2.3	Low-energy enhancement of the photon-strength functions	27
2.4	Photo-nuclear Cross sections	34
3	Data Analysis and Results	38
3.1	Systematics	39
3.1.1	Interpolation Method	39
3.2	Results	41
4	Discussion and Conclusion	52
4.1	Discussion	52
4.1.1	Photo-proton cross section	52
4.1.2	LEE and shell effects	53
4.1.3	Paramagnetism in the quasi-continuum	56
4.2	Conclusion	56
	Appendix A	58
A.1	Nuclear Symmetry Energy	58
	Appendix B	61
B.1	Interpolation Code	61
B.2	Saclay annihilation photon method	64

List of Figures

1.1	The nuclear chart. Black squares represent the line of β -stability. The majority of nuclei are unstable and decay by β^- (pink), β^+ /electron-capture (blue) and alpha (yellow) decay [1].	2
1.2	Experimental photo-nuclear cross sections for ^{12}C and ^{236}U	3
1.3	The polarizability parameter κ determined from the Dietrich & Berman compilation. Equation 1.6 for $\kappa = 1$ is represented by the horizontal line (black).	5
1.4	Illustrating the enhancement of the photon strength function at low energies.	6
1.5	Maxwellian-averaged capture reaction (n, γ) rates for the Cd, Mo and Fe isotopic chains from parametrized generalized Lorentzian functions with $T_f = 0.3$ MeV (left) and including the LEE (right) [48].	7
2.1	Types of GRs characterized according to L, S and T.	10
2.2	A simplified illustration of the GT-mode of vibration, the smaller sphere represents the proton distribution whose motion is indicated by the bold continuous arrow. The vibration cycle is shown as time evolves [56].	11
2.3	The SJ-mode of vibration. Plus signs indicate density excess and minus signs indicate density reduction [56].	11
2.4	Variation of the centroid energy E_{GDR} with nuclear mass number. Semi-magic and magic nuclei are represented by black squares. The resonance energy saturates at $E_{GDR} \approx 13$ MeV.	12
2.5	Schematic illustration of the harmonic oscillator SM, states are labeled by the principal quantum number N.	13
2.6	Comparison of the macroscopic and microscopic description of GDR energies. The 2p-2h excitations present twice the energy of the 1p-1h excitations and reproduce the E_{GDR} for nuclei above $A \approx 150$	13
2.7	Gamma-ray strength functions for the molybdenum isotopes $^{93-98}\text{Mo}$. The blue solid line represent the SLO Eq. 2.14 and the dashed blue line corresponds to Eq. 2.16 the GLO. The (black) dash-dot line was reproduced using the GLO-up2 model [64], discussed in §2.3.	18

2.8	Deformed nucleus in an electric field. The interaction between the electric field \mathbf{E} and the electric dipole moment \mathbf{D} , which tends to align with the symmetry axis, produces a torque which causes rotation.	25
2.9	Calculated $f(E_\gamma)$ for ^{208}Pb , ^{126}Cs and ^{160}Dy showing a GDR shape with a single peak (spherical), two peaks (oblate) and three unequal peaks (tri-axially deformed), respectively. The strength functions are computed within the QRPA model [77, 78].	28
2.10	The comparison of ^{95}Mo $f(E_\gamma)$ s measured using the Oslo method (filled blue diamonds) and the alternative technique using primary γ -ray decay from the quasi-continuum to individual low-lying discrete levels [84].	29
2.11	The polarization asymmetry A_o as a function of primary γ -ray energies. The red-solid line represents expected A_o assuming a linear polarization $P = 0.30$ with corresponding uncertainty range denoted by the red band, the grey band represents the statistical uncertainty of measuring a uniform distribution [86].	29
2.12	Lowest-energy single-quasi-particle transitions from excited states in a compound nucleus ($T > 0$) and those from the frozen states in the ground-state nucleus ($T = 0$), where $n(E)$ is the effective occupation probability distribution and ε_F the Fermi energy [87].	30
2.13	$f(E_\gamma)$ for ^{94}Mo reproduced by the TCQRPA model at finite and $T = 0$ (ground state) temperatures compared with experimental data [87].	31
2.14	$f(E_\gamma)$ for ^{94}Mo obtained from (γ, n) (green squares) and $(^3\text{He}, ^3\text{He}')$ (blue circles) measurements and the M1 strength function extracted from SM calculations (black solid line) [88].	31
2.15	Comparison of experimental $f(E_\gamma)$ and SM calculations for ^{44}Sc [95].	32
2.16	Experimental $f(E_\gamma)$ (open and shaded squares) compared with (red solid line) combined contributions of the GDR, M1 spin-flip, SR and the up-bend. The SR and the up-bend are represented by the red-dashed line [83].	33
2.17	Schematic photonuclear reactions, showing photon scattering and single particle emission.	34
2.18	Schematic illustration of open proton and neutron channels for the isobar residual nuclei ^{44}Sc and ^{44}Ca	36
3.1	Interpolation function (solid red-line) of $f(E_\gamma)$ for ^{45}Sc and the low energy tail of a Lorentzian function (solid orange-line) in the LEE region.	40
3.2	Showing the spin distribution of g_J for dipole transitions between states with $J = 1$ to $J = 12$	42
3.3	Experimental photo-nuclear cross section for ^{50}V , ^{51}V , ^{56}Fe and ^{76}Ge interpolated with a cubic-spline function (red solid line). Experimental data were obtained from references given in Table 3.2.	43

3.4	Experimental photo-nuclear cross section for ^{92}Zr , ^{95}Mo , ^{138}La and ^{135}Sm interpolated with a cubic-spline function (red solid line). Experimental data were obtained from references given in Table 3.2.	44
3.5	Photo-nuclear cross section data for ^{45}Sc including (γ, n) and (γ, p) reaction cross sections. The total cross section (red) line is the sum of these reaction channels. The sudden drop of the total cross section results from missing (γ, p) data at $E_\gamma \geq 25\text{MeV}$. . .	45
3.6	$f(E_\gamma)$ for ^{50}V , ^{51}V , ^{56}Fe and ^{76}Ge fitted with a cubic polynomial. . .	47
3.7	$f(E_\gamma)$ for ^{92}Zr and ^{135}Sm fitted with a cubic polynomial. The lanthanum isotopes, $^{138,139}\text{La}$, were fitted with a 4 th order polynomials due to the large RMS when fitted with cubic polynomials. . .	48
3.8	$f(E_\gamma)$ for ^{45}Sc fitted with a cubic polynomial, the dash blue line represents the extrapolated data region.	49
3.9	Comparison of the obtained results with the hydrodynamic model predictions with mass dependent symmetry $a_{sym}(A)$ and $a_{sym} = 23\text{ MeV}$. The blue circles represent δ values and black diamonds κ values, with a similar pattern.	51
4.1	Second moment of photo-nuclear cross sections of self-conjugate nuclei, with and without the $\sigma(\gamma, p)$ cross sections, emphasizing the significance of photo-proton cross sections.	53
4.2	Nucleon threshold energy differences for magic and semi-magic nuclei (black circles) for $N = 20, 28, 50, 82$ and 126 isotones. A significant fraction of these nuclei have low S_p energies compared to S_n in concordance with closed shells properties	54
4.3	σ_{-2} vs A on a log-log scale from the photo-neutron cross-section evaluation (solid circles) [25] and σ_{-2} data listed in Table 3.2 excluding (squares) and including (diamonds) the LEE contributions. For comparison, Eq. 1.6 (dashed line) is plotted.	55
4.4	$f(E_\gamma)$ vs E_γ on a log scale showing the interpolation to the data (solid line) for ^{45}Sc and ^{153}Sm	57
A.1	Symmetry energy extracted from GDR parameters (blue circles), the color line is the fit using Eq. A.4.	59
A.2	Symmetry energy extracted from σ_{-2} (blue circles), fitted using Eq. A.2.	60
B.1	Photonuclear cross section of ^{138}La showing the interpolation function $f(E_\gamma)$, red solid line.	62
B.2	Schematic of the Saclay linac, accelerating positrons [132] at desired energies towards a low-Z target.	64
B.3	Schematic view of the Saclay experimental set up, showing positron and photon beam transport elements [131].	65
B.4	The annihilation process shown in lab reference frame [131].	65

List of Tables

3.1	The σ_{-2} and σ_{total} values obtained from Ref. [25] (upper part) and the interpolation method (lower part). A thick solid line separates the two methods.	41
3.2	Low-energy enhancement contribution to the (-2) moment of the total photo-absorption cross section, σ_{-2} , and to the nuclear polarizability parameter, κ . Data have been extracted from EXFOR [103] and ENDF [104]. An asterisk indicates that the calculation includes $\sigma(\gamma, p)$ and C is the percentage contribution of $\sigma_{-2}(\text{LEE})$ to $\sigma_{-2}(\text{total})$	46
3.3	Approximate threshold energies of the enhancement of experimental $f(E_\gamma)$	48
3.4	Low-energy enhancement contribution to the nuclear polarizability parameter, κ	50
4.1	Ratios of proton to neutron emission reaction cross sections, particle threshold energies, experimental (γ, p) and (γ, n) cross sections. The cross sections were calculated using the interpolation method in this work.	53

Chapter 1

Introduction

Physics is the study of natural phenomena. Nuclear physicists have since the discovery of the nucleus been working on understanding its dynamics. The nuclear chart, analogous to the periodic table of elements, is illustrated in Fig. 1.1 and color coded according to decay modes. Several theoretical models, based on various hypothesis, have been developed during the years in order to understand nuclear phenomena such as nucleon-nucleon (n-n) interactions, binding energies, radii, excited states, etc. Unfortunately, no-unique model is actually able to grasp all nuclear phenomena at the desired level of accuracy.

Among the different models, we notice that two distinct hypotheses can be used to describe nuclear properties. Firstly, the independent particle shell model (IPSM) + the n-n residual interaction, which assumes that a nucleon moves independently in a potential generated by other nucleons. Secondly, the macroscopic models, where a nucleus is considered as a whole, i.e. neutrons and protons behave cooperatively and are mutually coupled to each other; highlighting the short-ranged character of the nuclear force. The liquid-drop model is an example of such macroscopic models. Refinement of these models is dependent on experimental observations that are better detailed for nuclei along the line of β -stability, making up a small fraction of the known isotopes, as shown in Fig. 1.1.

In practice, various techniques for studying exotic nuclei up to neutron and proton drip-lines have been devised, including the use of radioactive ion beams. However, the main challenges are the synthesization and short lived periods of these exotic nuclei resulting in insufficient data collection from which the characteristics and structural information are extracted. In general, nuclei have unique structures represented by a particular configuration as given by the shell model (SM). These structures impact a number of physical quantities, e.g. transition probabilities, cross sections and photon-strength functions. Experimental methods such as Coulomb excitation or electromagnetic radiation are used to probe these structures without invoking the nuclear force.

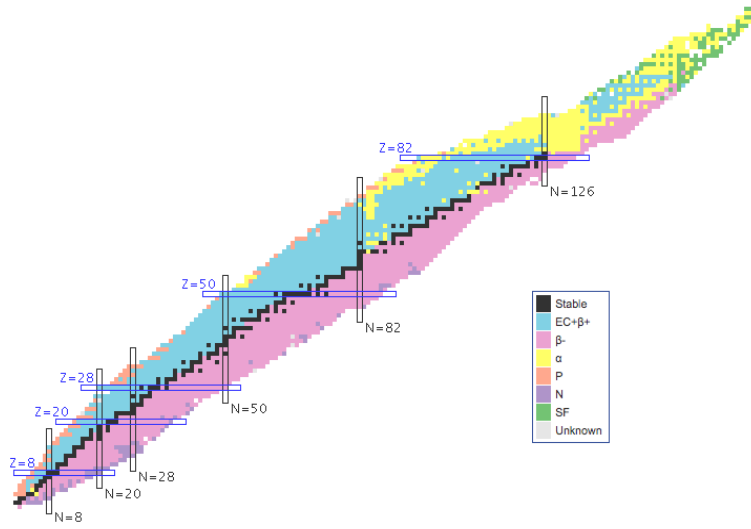


Figure 1.1: The nuclear chart. Black squares represent the line of β -stability. The majority of nuclei are unstable and decay by β^- (pink), β^+ /electron-capture (blue) and alpha (yellow) decay [1].

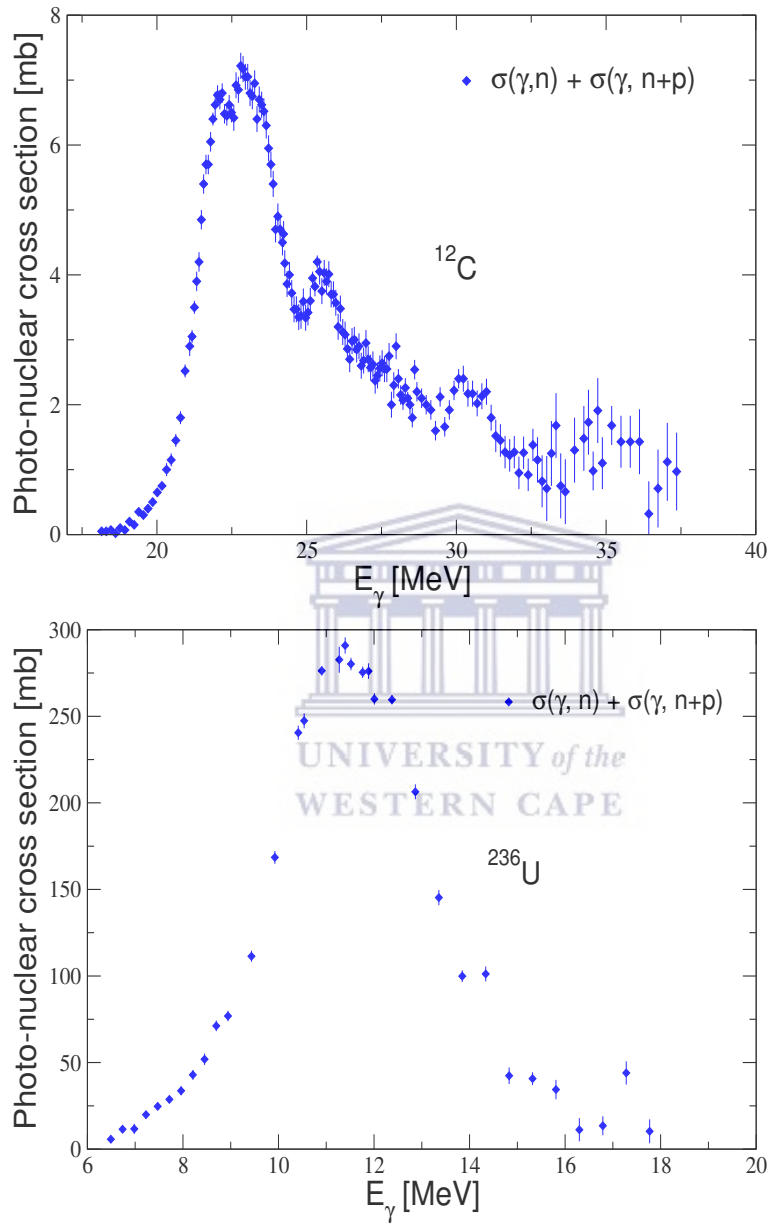
1.1 Scientific Motivation

When matter is subjected to an electromagnetic field, polarization occurs as a perturbation of the charge distribution. Common to all nuclear systems is the existence of giant resonance (GR) motions – giant because it involves many if not all nucleons. The nuclear polarizability is dominated by the isovector giant dipole resonance (GDR) [2, 3, 4] – observed as a wide peak in photo-nuclear cross-section measurements, whose width is on average around 7 MeV. The GDR was the first quantum collective excitation discovered in mesoscopic systems [5]. Figure 1.2 illustrates the GDR peaks for the nuclei ^{12}C and ^{236}U , including structural effects such as alpha-clustering observed as bumps at $E_\gamma \approx 26, 30$ MeV for ^{12}C . The GDR can be initiated by any type of mechanism that transmits enough energy for a nucleus to resonate, such as ion collision and irradiation with γ rays.

The ability for a nucleus to be polarized is driven by the dynamics of the GDR, i.e. the inter-penetrating motion of proton and neutron fluids out of phase [2]. This motion results from the nuclear symmetry energy acting as a restoring force,

$$a_{sym}(A)(\rho_n - \rho_p)^2/\rho, \quad (1.1)$$

in the Bethe-Weizsäcker semi-empirical mass formula, acting as a restoring force [2, 6]; where ρ_n, ρ_p, ρ and A are the neutron, proton and total densities and the atomic mass, respectively. The final form of the symmetry energy parameter $a_{sym}(A)$ is key to understanding the elusive equation of state of neutron-rich matter, which impacts three-nucleon forces [7], neutron skins [8, 9], neutron stars and supernova cores [10, 11, 12, 13, 14].

Figure 1.2: Experimental photo-nuclear cross sections for ^{12}C and ^{236}U .

Migdal [6] calculated the ground-state nuclear polarizability, $\alpha = \frac{\mathbf{D}}{\mathbf{E}}$, where \mathbf{D} is the electric dipole moment and \mathbf{E} the electric field strength, induced by a constant electric field using a semi-classical treatment of inter-penetrating proton and neutron fluids. Migdal assumed that nuclei have a well-defined surface of radius $R = r_0 A^{1/3}$ fm where $r_0 = 1.2$ fm with a potential energy governed by the collective variable ρ_p . It was deduced that α is proportional to the size of the nucleus by the following power law,

$$\alpha = \frac{e^2 R^2 A}{40 a_{sym}} = 2.25 \times 10^{-3} A^{5/3} \text{ fm}^3, \quad (1.2)$$

with $a_{sym} = 23$ MeV being the symmetry energy parameter [15, 16] and $e^2 = 1.44$ MeV·fm. The nuclear polarizability can also be determined using second-order perturbation theory¹

$$\alpha = 2e^2 \sum_n \frac{\langle i \| \hat{E}1 \| n \rangle \langle n \| \hat{E}1 \| i \rangle}{E_\gamma} = \frac{\hbar c}{2\pi^2} \sigma_{-2}, \quad (1.3)$$

where $\hat{E}1$ is the electric dipole operator, $|n\rangle$ and $|i\rangle$ the final (GDR) and initial (ground) states E_γ the transition energy and σ_{-2} the inverse square energy weighted sum rule of the total photo-absorption cross-section [17, 18].

$$\sigma_{-2} = \int_{E_{threshold}}^{E_{\gamma max}} \frac{\sigma_{total}(E_\gamma)}{E_\gamma^2} dE_\gamma. \quad (1.4)$$

The total photo-absorption cross section, $\sigma_{total}(E_\gamma)$, generally includes $\sigma(\gamma, n) + \sigma(\gamma, p) + \sigma(\gamma, np) + \sigma(\gamma, 2n) + \sigma(\gamma, 3n)$ cross sections. Alternatively, α can be well described by microscopic mean-field approaches using the random-phase approximation (RPA) with various effective interactions [19, 20, 21, 22, 23, 24].

The σ_{-2} values have been determined above neutron threshold to an upper limit of $E_{\gamma max} \approx 20 - 50$ MeV from the 1988 photo-neutron cross-section evaluation [25], which excludes relevant $\sigma(\gamma, p)$ contributions for $A \lesssim 50$ nuclei. These data include the GDR region and are representative of nuclei above $A \gtrsim 50$, where, because of the high Coulomb barrier, neutron emission is generally the predominant decay mode. From Eqs. 1.2 and 1.3, σ_{-2} can be defined as,

$$\sigma_{-2} = 2.25 A^{5/3} \mu\text{b}/\text{MeV}. \quad (1.5)$$

This relation was qualitatively confirmed by Levinger [26] from a fit to the available photoabsorption cross-section data in 1957, and further refined by Orce [27] from the 1988 photo-neutron cross-section evaluation [25],

$$\sigma_{-2} = 2.38 \kappa A^{5/3} \mu\text{b}/\text{MeV}, \quad (1.6)$$

¹A complete quantum mechanical treatment of polarizability is presented in chapter 2, related to the static nuclear polarizability α via σ_{-2}

where κ is the polarizability parameter and represents deviations between the actual GDR effects and the hydrodynamic model. The value of κ can be determined experimentally from the comparison of the measured σ_{-2} values with the empirical formula in Eq. 1.6, $\frac{\sigma_{-2}}{2.38A^{5/3}}$.

A value of $\kappa = 1$ generally holds for the ground state of nuclei with $A \gtrsim 50$, and probably for even lighter nuclei with $A \gtrsim 20$ once $\sigma(\gamma, p)$ contributions are taken into account [26, 27]. In contrast, values of $\kappa > 1$ are generally found for light nuclei with $A < 20$ where surface effects are not negligible [26, 27, 28, 29, 30, 52, 32]. Therefore Eq. 1.6 is applicable to heavy nuclear systems. An implicit study of self-conjugate nuclei will be conducted in order to show the significance of (γ, p) cross-section measurements and its contribution to σ_{-2} , in particular for light nuclei.

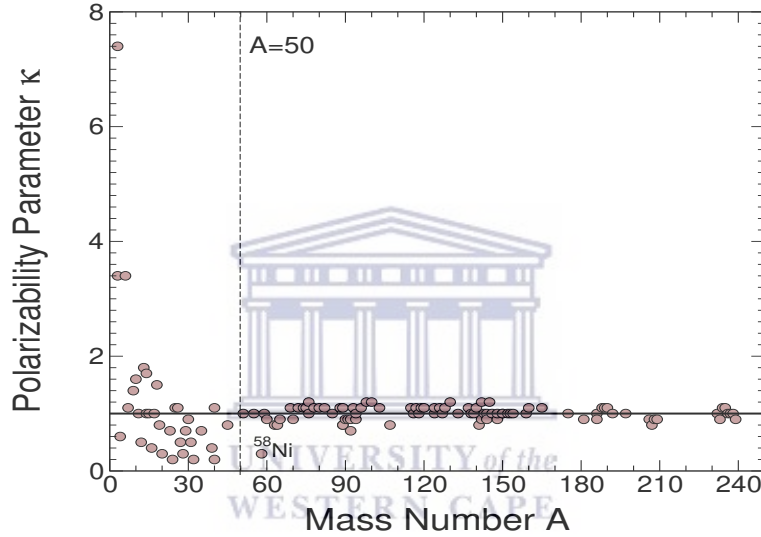


Figure 1.3: The polarizability parameter κ determined from the Dietrich & Berman compilation. Equation 1.6 for $\kappa = 1$ is represented by the horizontal line (black).

There are other resonances below the neutron threshold that may substantially contribute, because of the $1/E_\gamma^2$ dependence in Eq. 1.4, to the nuclear polarizability and σ_{-2} . For instance, von Neuman-Cosel suggested that the pigmy dipole resonance (PDR) may contribute $\approx 5 - 10\%$ to the final σ_{-2} value [33]. The PDR is an electric dipole, $E1$, resonance is believed by some authors to arise from the oscillation of a symmetric proton-neutron core ($N \approx Z$) against the neutron skin. It follows that the PDR is only observed in nuclei with neutron excess, where the neutron skin thickness is not negligible [34], the case of ^{48}Ca suggests that the neutron skin exists for medium-mass nuclei [35]. Other ground-state soft resonances such as the $M1$ scissors mode and spin-flip will also contribute to a lesser extent. Contrarily, because of the $1/E_\gamma^2$ energy weighting in Eq. 1.4, σ_{-2} values are less sensitive to the contribution of nucleon resonances arising at $E_\gamma \gtrsim 140$ MeV. Such pion exchange currents accounts for less than

5% of the total σ_{-2} contribution [26, 36, 37, 38]. In fact, an upper limit of integration below 50 MeV approximates the σ_{-2} asymptotic value for light and medium-mass nuclei [38]. Therefore, σ_{-2} values are extremely sensitive measures of low-energy long-range correlations in the nuclear wave functions, which are common feature for all nucleon-nucleon potentials, and fundamental for SM calculations of heavy nuclei [39] using low-momentum interactions [40].

Furthermore the photon or radiative strength function, $f(E_\gamma)$, characterizes average electromagnetic decay and absorption properties of excited (and ground state) nuclei, indicating the ability (or average reduced probability) of atomic nuclei to emit and absorb photons with energy E_γ . According to the Brink-Axel hypothesis, $f(E_\gamma)$ is independent of the particular structure and only depends on E_γ [41, 42]. Therefore $f(E_\gamma)$ can be measured at various excitation energies including the ground state. This was verified by Guttormsen and co-workers in ^{238}Np using different excitation-energies in the quasi-continuum region [43]. Recent findings of a low-energy enhancement (LEE)² of $f(E_\gamma)$ at low $E_\gamma \approx 1-4$ MeV for medium and heavy-mass nuclei along the line of β -stability [45, 46, 47] may affect our understanding of the nuclear polarizability.

The physical origin of the LEE remains ambiguous and its observation seems to be generally associated to nuclei in the $A \approx 50$ and 90 mass regions which are not well deformed. All LEE have in common that they occur at high excitation energies in the quasi-continuum region. This enhancement is shown for ^{45}Sc in Fig. 1.4, where the enhancement starts at $E_\gamma \approx 3.5$ MeV.

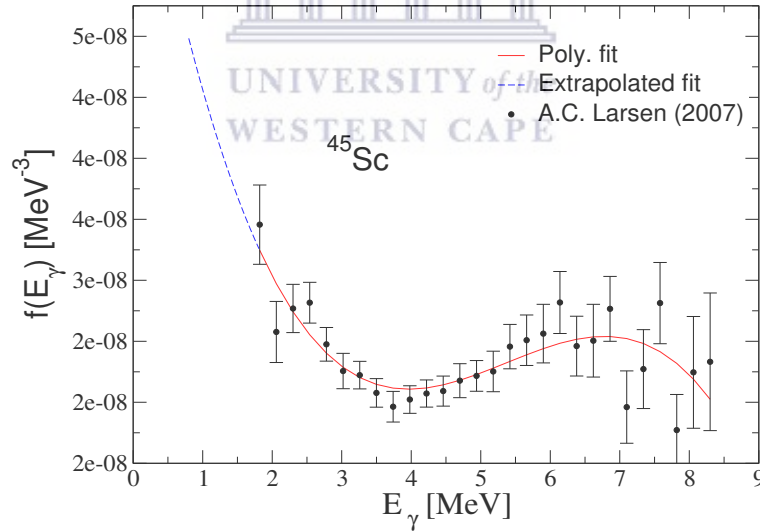


Figure 1.4: Illustrating the enhancement of the photon strength function at low energies.

²A detailed theoretical description of the LEE and its suggested origin are presented in Chapter 2.5

If this enhancement persists for exotic neutron-rich nuclei, its influence on neutron capture reaction rates and cross sections could change the predicted abundance of some of the elements by up to two orders of magnitude [48]. The effect of the enhanced $f(E_\gamma)$ is smaller in stable nuclei compared to nuclei approaching the drip line with low neutron separation energies, particularly for Fe, Mo and Cd isotopic chains as shown in Fig. 1.5.

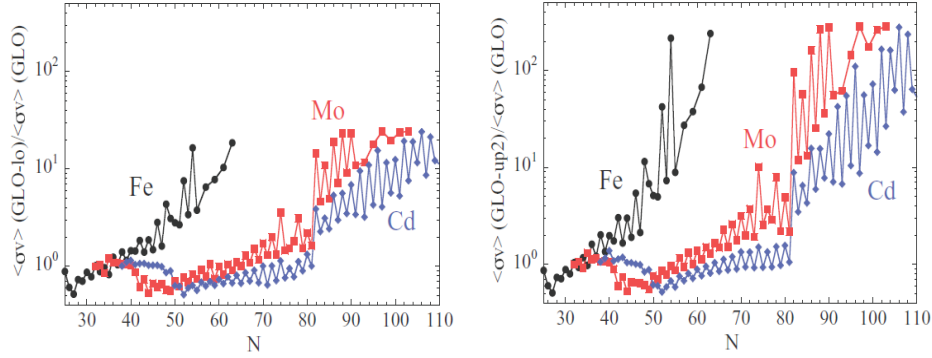


Figure 1.5: Maxwellian-averaged capture reaction (n,γ) rates for the Cd, Mo and Fe isotopic chains from parametrized generalized Lorentzian functions with $T_f = 0.3$ MeV (left) and including the LEE (right) [48].

The LEE described above results from measurements at high excitation energies and for the purposes of this work the LEE data will be combined with existing total $f(E_\gamma)$ and photo-absorption cross sections measured in the ground state. This comparison, typically used in the literature, is somewhat, misleading, as the former corresponds to γ -ray transitions between excited states in the quasi-continuum, whereas the latter involves transitions to the ground state.

Nonetheless, the study of (p,γ) and (n,γ) reactions for light nuclei and fusion-evaporation reactions for heavy nuclei have shown that GDRs can also be built on excited states (GDR^{exc}) [49, 50, 51]. The GDRs^{exc} present – at least for moderate average temperature T and spin J – similar centroid energies, E_{GDR}^{exc} , and resonance strengths, S_{GDR}^{exc} , relative to the Thomas-Reiche-Kuhn (TRK) $E1$ sum rule [44], as those found for the ground-state counterparts ($\text{GDR}^{g.s.}$) [49, 50]. The TRK $E1$ sum rule will be described in the following chapter.

These similar features suggest a common physical origin for all GDRs in concordance with the Brink-Axel hypothesis, which also indicates that a GDR can be built on every state in a nucleus [41, 42]. Moreover, the sum rule in Eq. 1.3 can also be applied to final excited states $|f\rangle$ [28, 32, 52]. Henceforth, one could assume similar resonance strengths for GDRs built on the ground and excited states. This may explain the nice fit between the high γ -ray energy part of the measured $f(E_\gamma)$ and the left tail of the $\text{GDR}^{g.s.}$ (see e.g. [53]). The observed stability of the GDR allows study of excited nuclei properties i.e. nuclear polarizability in this work.

The purpose of this work is to show how the combined dynamics of the LEE and GDRs affect σ_{-2} and κ values and provide evidence for the continuing influence of shell effects at high-excitation energies. The study will be conducted in the following manner. In chapter two a review on GRs, $f(E_\gamma)$, α and LEE will be done. Various models- classical, semi-classical and quantum mechanical- descriptions of α will be discussed. Noting the fundamental assumptions affecting the description of α is crucial. Chapter three entails data analysis systematics and results presented in tabular and graphic format. Finally, chapter four discusses and summarizes the results, including remarks and future work. The appendices A & B contain related work.



Chapter 2

Theory and Literature Review

2.1 Giant Resonances

Precisely eighty years ago Bothe and Gentner noted the evidence of the GR type phenomenon. They measured the radioactivity induced by bombardment of various samples of material with γ radiation obtained using the $\text{Li}(p,\gamma)$ reaction. To their surprise the measured cross sections were much larger than expected; this was because of the lack of analytic and systematic studies of resonances at that time which were later systematically studied by Baldwin and Klaiber [5, 54].

A GR can be described as a high frequency, damped, nearly harmonic shape of vibration around the equilibrium shape of a nuclear system. Macroscopically the GR vibration frequency is in the 10^{21}Hz range, particularly the GDR [54]. Giant resonances correspond to collective motion involving many if not all particles in the nucleus [2, 54, 55], and are generally described by three parameters, E_R , Γ_R and S_R , which correspond to the resonance energy, width and strength of the resonance, respectively. There are many types of resonances, among others, the isovector (IV) giant electric dipole resonance (GDR), isoscalar (IS) giant magnetic dipole resonance (GMDR) and giant quadrupole resonance (IV and IS GQR). Other soft resonances include the PDR, scissors-mode resonance (SR). Isovector in this case indicates out of phase oscillations, whereas isoscalar indicates in phase oscillations. Alternatively, GRs are characterized by polarity (L), spin (S) and isospin (T) as shown in Fig. 2.1. The isospin quantum number $T = \frac{1}{2}(N - Z)$, serves as a measure of the charge independence of the nuclear force that is violated by the electromagnetic interaction.

The idea of collective dipole oscillations was first proposed by Migdal in 1944 [2] using the hydrodynamic model. Assuming that the nucleus behaves like an incompressible fluid whose total density ρ_o is constant and the intrinsic potential energy V_i due to protons, is governed by ρ_p ,

$$\rho_o = \rho_p + \rho_n = \frac{A}{V}, \quad (2.1)$$

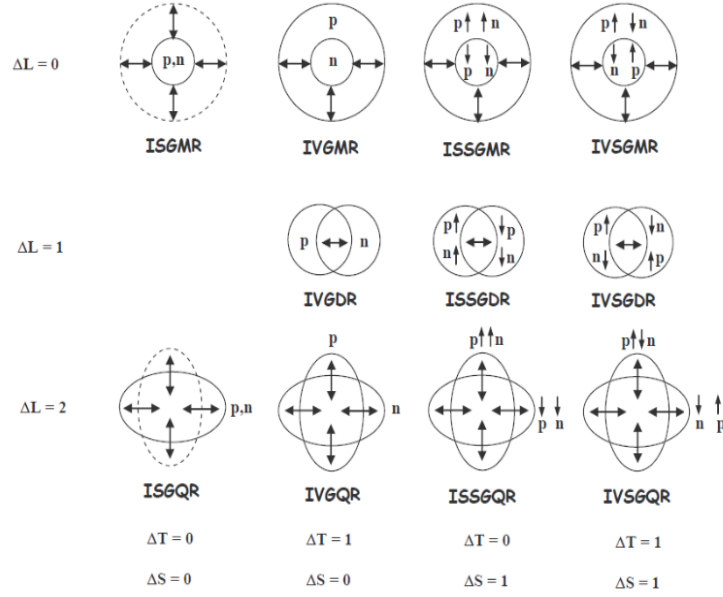


Figure 2.1: Types of GRs characterized according to L, S and T.

where $\rho_o = 0$ for $r > R$, with R being the spherical nuclear radius and V the volume. The potential energy is finite at $r = 0$ and varies inside the nucleus in absence of an external electric field as follows,

$$\frac{dV_i}{dr} = -4\pi\rho_p, \quad (2.2)$$

where ρ_p takes the form,

$$\rho_p = \rho_p(0) \left[1 + \frac{\lambda^2 r^2}{6} + \frac{\lambda^4 r^4}{120} + \dots \right], \quad (2.3)$$

with $\lambda^2 = \frac{\rho_o \pi}{2a_{sym}}$. Note that according to Eq. 2.3, $\rho_p(r = R) - \rho_p(r = 0) > 0$, indicating a higher proton density on the periphery of the nucleus, which is a crude and unrealistic property of a nucleus.

This notion was further analyzed by Goldhaber and Teller, who suggested among their three models [4], that protons and neutrons might behave like two separate but inter-penetrating spherical density distributions. The resulting resonance consists of small harmonic displacements of these distributions with respect to each other, as illustrated in Fig. 2.2. They showed, according to the vibrational model that the resonance energy E_{GDR} is estimated by [4, 56],

$$E_{GDR} = \hbar\omega = \sqrt{\frac{3\varphi\hbar^2}{r_0 m_{nu} \epsilon}} A^{-\frac{1}{6}}, \quad (2.4)$$

where φ is the energy needed to extract one proton from its neutron environment or a neutron from its proton environment. Note that $\varphi \neq S_n$ or S_p , the neutron

and proton separation energies, respectively, ϵ is the length (range of the nuclear force) at which the neutron-nucleus interaction changes from zero outside the nucleus to a higher value and m_{nu} is the single nucleon mass. This is known as the Goldhaber-Teller (GT) model.

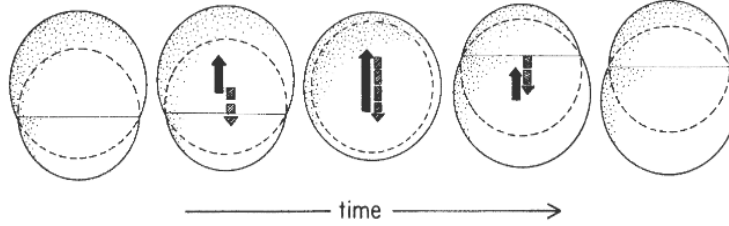


Figure 2.2: A simplified illustration of the GT-mode of vibration, the smaller sphere represents the proton distribution whose motion is indicated by the bold continuous arrow. The vibration cycle is shown as time evolves [56].

Amongst the three models by Goldhaber and Teller [4] one was later analyzed further by Steinwedel and Jensen [3]. The Steinwedel-Jensen (SJ) model suggested that the GDR might consist of density vibrations of the neutron and proton fluids against each other within a fixed spherical surface. This motion is shown in Fig. 2.3. and corresponds to the lowest distinguishable mode in a spherical distribution with E_{GDR} given by [3, 56],

$$E_{GDR} = \hbar\omega = \sqrt{\frac{4NZ}{A^2}} 60A^{-\frac{1}{3}} \text{ MeV}. \quad (2.5)$$

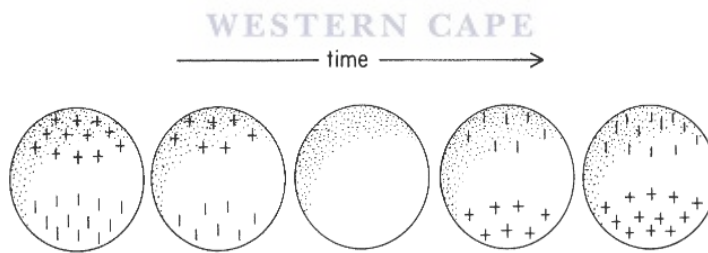


Figure 2.3: The SJ-mode of vibration. Plus signs indicate density excess and minus signs indicate density reduction [56].

Independent of the model, it results that heavy nuclei resonate at lower energies compared to light nuclei, as observed in Fig. 1.2 for ^{12}C and ^{236}U . One can note that the SJ mode at peripherals of nuclei is the GT mode of vibration, regardless of the restrictions in Eq. 2.1. However, both models are based on crude assumptions and E_{GDR} data show both $A^{-\frac{1}{3}}$ and $A^{-\frac{1}{6}}$ dependences, indicating that resonances are collective phenomena.

An acceptable macroscopic definition of the GDR results from considering it as a superposition of GT and SJ modes of vibration. Figure 2.4 and Eq. 2.6 illustrate the nature of the mass dependence,

$$E_{GDR} = 30.2A^{-\frac{1}{3}} + 20.6A^{-\frac{1}{6}} \text{ MeV.} \quad (2.6)$$

The GT+SJ model shows some interesting structural features when compared with experimental data. In particular, single and double magic nuclei are well predicted by GT+SJ model represented as black squares in Fig. 2.4. This follows from the fact that magic nuclei are mostly spherical in their ground state. Experimental centroid energies, on the other hand, show a slight increase in the region $A \sim 150 - 175$, known as a region of super-deformation. This implies that super-deformed nuclei are not ideal vibrational systems and they are susceptible to other modes of excitation such as rotation. Additionally, one can infer from Fig. 2.4 that the GT+SJ model does not coincide with both SJ and GT models predictions.

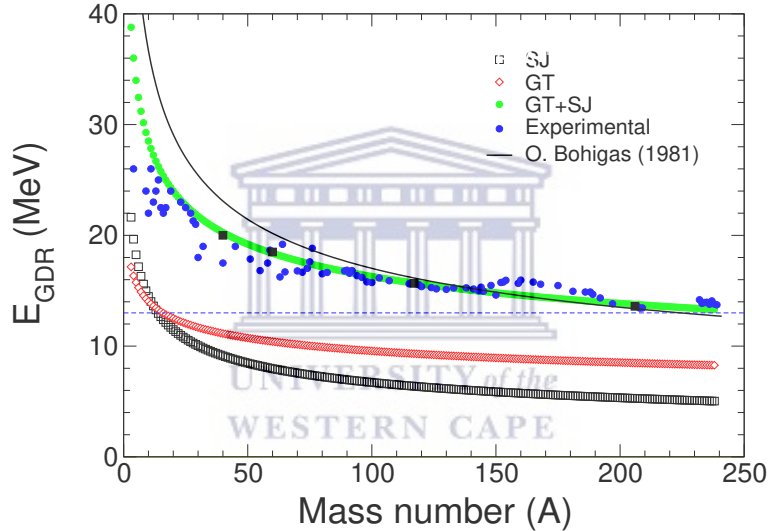


Figure 2.4: Variation of the centroid energy E_{GDR} with nuclear mass number. Semi-magic and magic nuclei are represented by black squares. The resonance energy saturates at $E_{GDR} \approx 13$ MeV.

To this point, the GDR has been described as a collective phenomenon, thus ignoring structural effects arising from the n-n interaction. The GDR can also be interpreted microscopically by the SM as a superposition of one-particle-one-hole (1p-1h) excitations, that are in phase [57]. The 1p-1h excitation in the simplest harmonic oscillator SM correspond to the jump of a nucleon to the upper adjacent shell (unperturbed excitations), grouped in energies around $41A^{-1/3}$ MeV for dipole excitations, as shown in Fig. 2.5, where N is the principal quantum number corresponding to a particular shell. Contrarily, it is experimentally known that the GDR is concentrated at about twice the energy predicted by the harmonic oscillator model, in particular for heavy nuclei, as shown in Fig. 2.6 which approximates 2 times $41A^{-1/3}$. A better prediction

of E_{GDR} results from the IPSM calculations by Bohigas, as $E_{GDR} = 79A^{-1/3}$ MeV [19], represented by a black solid line in Fig. 2.4. It is worth noting that both the macroscopic and microscopic (2p-2h) interpretations of the GDR are complementary, particularly in the $A \gtrsim 100$ mass region, as observed in Fig. 2.4 and Fig. 2.6.

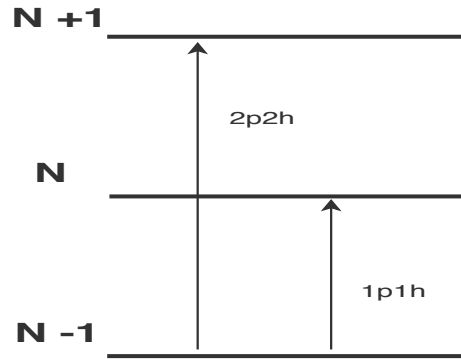


Figure 2.5: Schematic illustration of the harmonic oscillator SM, states are labeled by the principal quantum number N .

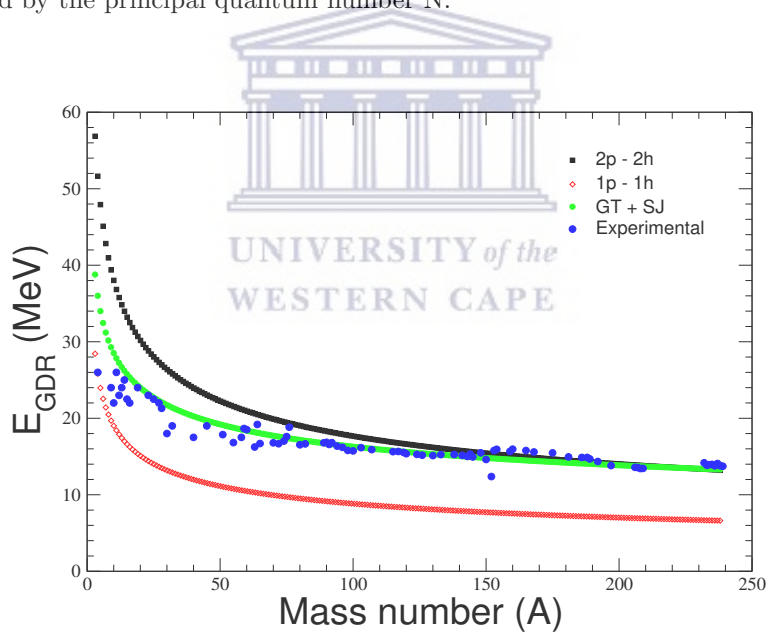


Figure 2.6: Comparison of the macroscopic and microscopic description of GDR energies. The 2p-2h excitations present twice the energy of the 1p-1h excitations and reproduce the E_{GDR} for nuclei above $A \approx 150$.

2.1.1 Damping of giant resonances

Among the parameters describing GRs is the width Γ_R . Understanding Γ_R is quite demanding because of the different excitation mechanisms being involved and their admixture (e.g. multi-phonon mixing) that contributes non-negligibly to the resonance width. Herein, Γ_R is described according to the SM in terms of particle-hole (p-h) excitations and referring Γ_{GDR} to the GDR width. Experimental observations show that the width has three components [58]:

$$\Gamma_{total} = \Gamma_{inh} + \Gamma_{esc} + \Gamma_{spr} . \quad (2.7)$$

The inherent width Γ_{inh} characterizes the width due to spreading in the excitation energy of the 1p-1h strength function. This occurs if many non-collective 1p-1h configurations and the collective state (i.e. the GDR state) have similar quantum numbers and the 1p-1h configurations excitation energies are close to E_{GDR} . As an example, the non-collective $1\hbar\omega$ 1p-1h states energies are increased to energy regions between $1\hbar\omega$ and $2\hbar\omega$ due to the repulsive character of the residual p-h interaction [54], thus comparable to E_{GDR} . This results in to fragmentation of the resonance state.

It is known that on average E_{GDR} 's are located around 16 MeV for heavy nuclei. At these energies a high density of 2p-2h configurations of the same spin and parity as collective 1p-1h configurations lie at resonance energies [54], this is also shown in Fig. 2.6 at $A > 150$ where E_{GDR} is well reproduced by the 2p-2h excitations. Due to coupling of the 1p-1h and 2p-2h configurations the giant resonance acquires a width defined as spreading width, which for a state spin-parity $J^\pi = 1^-$ is defined by [58],

$$\Gamma_{spr} = 2\pi \langle 2p \cdot 2h | V_{int} | 1p \cdot 1h \rangle \rho(E_{GDR}) , \quad (2.8)$$

where fundamentally $\rho(E_{GDR})$ is the density of states at the E_{GDR} and V_{int} the interaction potential of the two configurations.

In general, the collective 1p-1h excitations are well above particle threshold energies e.g. S_n , thus we define an escape width Γ_{esc} acquired by particle emission. Γ_{esc} results from two processes, firstly the direct decay of the collective 1p-1h state by emission of a nucleon forming a compound nucleus (A-1). Secondly, the 1p-1h states can mix with 2p-2h states that results in complicated 3p-3h states and further np - nh states, $n \geq 4$. However, this width is noted to be negligible for $A \geq 90$ nuclei where $\frac{\Gamma_{esc}}{\Gamma_{total}} < 10\%$ [54, 58]. In light p and sd-shell nuclei Γ_{esc} is dominant [54], since these nuclei are loosely bound with low particle thresholds. Hence, this in one of the reasons the GDR cross section of ${}^3\text{He}$, for example, has an irregular distribution and a larger total width.

Therefore the width Γ_{total} is affected by the structure of a nuclear system and corresponds with the full width at half maximum (FWHM) of the GDR when observed in GDR cross sections. It can also be used to predict the shape or deformation of nuclear surfaces at resonance energies, as described in section 2.2.4. The width Γ_{total} or Γ_{GDR} is the key parameter in defining $f(E_\gamma)$, as shown in the following section.

2.1.2 Photon Strength Functions

In the process of studying nuclear structures various reactions are applied, the result by any of the considered reaction is the emission of particles and γ rays. Common to most reaction channels is the emission of γ rays. When a nucleus is excited, it de-excites in order to reach its equilibrium; generally in its ground state. In the process of de-excitation it emits energetic particles and γ rays with energy E_γ . Amongst the discrete states, there is a probability associated with each transition: transition probability. Fermi's golden rule states that the transition probability λ_{if} is proportional to the square of a transition matrix element and the level density at the final state $\rho(E_f)$,

$$\lambda_{if} = \frac{2\pi}{\hbar} \rho(E_f) |\langle f | \hat{H} | i \rangle|^2 . \quad (2.9)$$

The γ -ray emission or absorption channel herein is described by photon strength functions, further modeled by a continuous probability distribution function – the Lorentzian distribution – described in the following section. These photon strength functions characterizes average electrodynamic decay or absorption properties of excited nuclei. Leading to classifying the photon strength functions according to the method of extraction and reaction channel under consideration; that is, absorption (γ, A^*) or emission (A, γ) of γ rays. For a reaction where γ rays are used to excite nuclei, strength functions are called photo-excitation strength functions. Whereas, when γ rays are being emitted by an excited nucleus the strength functions are referred to as radiative (γ decay) strength functions. Gamma-rays are known to have two types of multi-polarity, i.e. electric and magnetic. It follows that photon strength functions are characterized by the γ -ray type and multi-polarity e.g. E1, M1, E2, etc.

Furthermore, the excitation and de-excitation involve two states of a certain spin and parity. Therefore allowing classification or grouping of γ -strength functions according to spin and parity. The strength functions can be expressed in terms of parameters or quantities with intrinsic probability dependence, such as photo-nuclear cross sections, transmission coefficients and radiation widths dependent on E_γ . The photo-excitation strength function, requiring high-resolution of γ rays may be written as [59],

$$f_{0fXL}^{J_0\uparrow} = \rho_J(E_f) \frac{\bar{\Gamma}_{0fXL}}{E^{(2L+1)}} , \quad (2.10)$$

for an excitation from the ground state of spin J_0 to an excited state of energy E_f , where $\bar{\Gamma}_{0fXL}$ is the average partial width, averaged over states $|f\rangle$ of a particular spin and parity around E_f . The radiative (γ decay) strength functions of states with spin and parity J^π , from E_i to E_f energy states may be written as follows [59],

$$f_{ifXL}^{J\downarrow} = \rho_J(E_f) \frac{\bar{\Gamma}_{ifXL}}{E^{(2L+1)}} . \quad (2.11)$$

The averages in the preceding two equations are taken over a large number of levels with spin and parity J^π . Alternatively, the photon strength function can be extracted from photo-absorption cross sections in the following manner [59],

$$f_{0fXL}^{J_0\uparrow}(E_\gamma) = \frac{2J_0 + 1}{(2J_f + 1)\pi^2(\hbar c)^2} \frac{\bar{\sigma}_{\gamma aXL}^J(E_\gamma)}{E_\gamma^{(2L-1)}} \text{ MeV}^{-3}, \quad (2.12)$$

where J_0 and J_f are the spins for the ground and excited states, respectively. $\bar{\sigma}_{\gamma aXL}^J(E_\gamma)$ is the photo-absorption cross section of a nucleus of interest. This relation Eq. 2.12 will be used to convert photon strength function data, LEE data, to cross sections required to compute the nuclear polarizability.

It is known from the single particle model that at high excitation energies there is a large number of configurations implying large level densities or small average spacing between energy levels. Thus yielding high statistics and allows us to have a broad distribution of reduced widths or more accurate averages, implying low Porter-Thomas fluctuations [60].

For simplicity $f(E_\gamma)$ will be used instead of f_{ifXL}^J , referring to electric dipole E1 polarity strength function unless stated otherwise. There are different types of models that are used to describe $f(E_\gamma)$, and will be discussed in the next section.

Photon strength functions are important in nuclear and astrophysics calculations. Particularly for model dependent calculations such as the Hauser-Feshbach statistical cross section for radiative neutron capture that is described in terms of total gamma transmission coefficients [61], reaction rates and when assessing the competition between particle and γ -ray emission [62].

The LEE of the $f(E_\gamma)$ will be related to cross sections in the following chapter, in order to calculate polarizability values from photo-nuclear cross sections data.

2.1.3 GDR Models

The original Brink hypothesis at intermediate energies proposed that the GDR shape can be described using the standard Lorentzian function (SLO), whose width Γ_o (FWHM) is independent of energy and temperature [63],

$$f(E_\gamma)^{SLO} = 8.68 \cdot 10^{-8} \frac{\sigma_o \Gamma_o^2 E_\gamma}{(E_\gamma^2 - E_o^2)^2 + E_\gamma^2 \Gamma_o^2} \text{ MeV}^{-3}, \quad (2.13)$$

where σ_o and E_o are the peak cross section and centroid energy, respectively. One of the problems of this model is the overestimation of $f(E_\gamma)$ at and below the neutron threshold S_n . Therefore, an improvement to this model was proposed, where the width $\Gamma(E_\gamma)$ is energy dependent and $f(E_\gamma)^{SLO}$ is expressed as follows [63],

$$f(E_\gamma)^{SLO} = 8.68 \cdot 10^{-8} \frac{\sigma_o \Gamma_o \Gamma(E_\gamma) E_\gamma}{(E_\gamma^2 - E_o^2)^2 + E_\gamma^2 \Gamma_o^2} \text{ MeV}^{-3}. \quad (2.14)$$

The idea of energy dependent width originates from spreading of 1p-1h states into 2p-2h states, thus increasing the magnitude of the total width. Further improvements were done by modifying the width to have both energy and temperature dependence as follows [63],

$$\Gamma(E_\gamma, T) = \Gamma_o \frac{E_\gamma^2 + 4\pi^2 T^2}{E_o^2} \text{ MeV} , \quad (2.15)$$

where $T = \sqrt{\frac{S_n - E_\gamma}{a_F}}$ is the temperature of the state at which the GDR is built, and a_F the Fermi gas level density parameter. There are still discrepancies between predicted and experimental strength functions when approaching zero energy, i.e. $E_\gamma \rightarrow 0$. To accommodate the discrepancy when approaching low energy limits, a generalized Lorentzian function (GLO) was proposed, indeed the GLO reproduces the experimental $f(E_\gamma)$ at low energies fairly well for nuclei in the mass region $A \sim 55 - 197$ [63]. This is shown for the molybdenum isotopes $^{93-98}\text{Mo}$ in Fig. 2.7, where the GLO – discussed below – fairly reproduces the strength functions down to $E_\gamma \sim 1$ MeV. Comparatively, the SLO prediction underestimates $f(E_\gamma)$. The GLO is expressed as follows,

$$f(E_\gamma)^{GLO} = 8.68 \cdot 10^{-8} \sigma_o \Gamma_o \left[\frac{\Gamma(E_\gamma, T) E_\gamma}{(E_\gamma^2 - E_o^2)^2 + E_\gamma^2 \Gamma(E_\gamma, T)^2} + 0.7 \frac{\Gamma(E_\gamma = 0, T)}{E_o^3} \right]. \quad (2.16)$$

However, the GLO underestimates $f(E_\gamma)$ for strongly deformed nuclei by up to a factor of 4 [65]. Taking into consideration the deformation of nuclei another Lorentzian function was derived and referred to as the enhanced generalized Lorentzian function (eGLO) in order to describe the GDR shape. In the eGLO the width is modified to have dependence on parameters k_o and E_o^γ that can be adjusted to reproduce the deformed GDR shape [65],

$$\Gamma(E_\gamma, T) = \left[k_o + \frac{E_\gamma - E_o^\gamma}{E_o - E_o^\gamma} (1 - k_o) \right] \Gamma_o \frac{E_\gamma^2 + 4\pi^2 T^2}{E_o^2}. \quad (2.17)$$

The enhancement of the width is purely empirical, note that when $k_o = 1$ the eGLO returns to the GLO. Flexibility of the eGLO function lies in the parameter k_o which varies smoothly with mass number. From a large number of calculations the behavior of k_o was studied applying the Kataris-Ramamurty-Kapoor (K RK) model [66, 67],

$$k_o = \begin{cases} 1.0 & A < 148 \\ 1.0 + 0.09(A - 148)^2 \exp[0.180(A - 148)] & A \geq 148 \end{cases}$$

So far the discussion only describes the electric part of $f(E_\gamma)$. The $f(E_\gamma)$ for magnetic dipoles, M1, may also be described by a Lorentzian shape as follows,

$$f_{M1}(E_\gamma) = \frac{\sigma_{M1} \Gamma_{M1}^2}{3(\pi \hbar c)^2} \frac{E_\gamma^2}{(E_\gamma^2 - E_{M1}^2)^2 + E_\gamma^2 \Gamma_{M1}^2}, \quad (2.18)$$

where σ_{M1} , Γ_{M1} and E_{M1} are the peak cross section, width and resonance energy of the giant magnetic dipole resonance, respectively. The M1 resonances in general occur at lower energies compared to the E1 (GDR) resonance energy E_{GDR} .

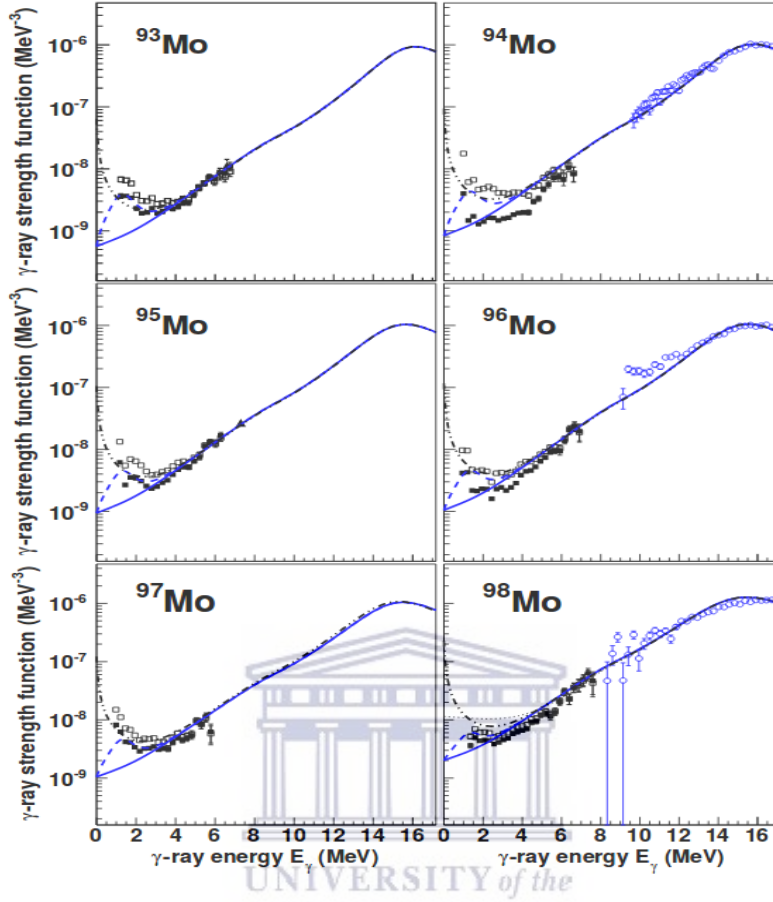


Figure 2.7: Gamma-ray strength functions for the molybdenum isotopes $^{93-98}\text{Mo}$. The blue solid line represent the SLO Eq. 2.14 and the dashed blue line corresponds to Eq. 2.16 the GLO. The (black) dash-dot line was reproduced using the GLO-up2 model [64], discussed in §2.3.

The models discussed above, which are based on Lorentzian distributions do not reproduce the LEE of $f(E_\gamma)$ at low energies – except perhaps for the GLO – whose effects are being investigated. Therefore an alternative interpolation method of computing the total cross sections including the enhancement region will be implemented in this work and elaborated in the following chapter.

2.2 Nuclear Polarizability

What happens to matter in an electric field? To answer this question consider a case whereby a neutral atom is subjected to an electric field. An atom consists of a nucleus (positively charged core) surrounded by the electron cloud. In the electric field the nucleus is displaced in the direction of the field and the electrons in the opposite direction [68]. This implies that charge is displaced

by an electric field, with reference to the equilibrium of a neutral atom. At the macroscopic level, the atom is polarized. A dipole moment \mathbf{D} , in the direction of the electric field \mathbf{E} is attained by the atom. The scalar dipole moment is defined as follows [68],

$$\mathbf{D} = \alpha \mathbf{E}. \quad (2.19)$$

The parameter α is the atomic polarizability. A similar argument applies for nuclei, where protons are displaced with respect to the center of the nucleus.

An electromagnetic field induces polarizability both electrically and magnetically. Electric polarizability is the relative tendency of a charge distribution to have its charges displaced by an electric field. Magnetic polarizability (or susceptibility) or simply magnetization mainly concerns spin interactions of atomic electrons and nucleons.

The electric polarizability will be evaluated for various cases. In §2.2.1 the case of a system modeled by a simple harmonic oscillator (S.H.O.) [69], with and without damping is discussed mainly for analogy purposes. This model can also be used to describe the GDR from a classical perspective. In §2.2.2 a quantum mechanical description of α is revised. The hydrodynamic model description of α , first introduced by Migdal [2] is also revised in §2.2.3.

2.2.1 The S.H.O. model of polarizability

Suppose that an electron is bound to a fixed point by a restoring Hooke force, $-kx$, and subjected to an external constant electric field with strength E . Applying Newton's second law of motion at equilibrium and considering the motion in one dimension,

$$-kx + eE = 0. \quad (2.20)$$

Thus,

$$x = \frac{eE}{k}, \quad (2.21)$$

where x describes small oscillations or the position of the oscillating body, e the electric charge and k the spring oscillation constant. Defining the angular frequency of oscillation as ν_o and m_e as the mass of the electron, k can be defined as [69],

$$k = 4\pi^2 m_e \nu_o^2. \quad (2.22)$$

The oscillating electron creates a dipole moment in the direction of the electric field, defined by,

$$D = ex. \quad (2.23)$$

Using Eq. 2.23 one can easily define the charge density of a certain charge distribution. Combining Eqs. 2.21, 2.22 and 2.23 the dipole moment is found as [68],

$$D = \frac{e^2 E}{4\pi^2 m_e \nu_o^2}. \quad (2.24)$$

Therefore the dipole moment depends on the characteristic frequency of oscillation, and can also be expressed in terms of α by combining Eqs. 2.19, 2.23 and 2.24,

$$\alpha = \frac{e^2}{4\pi^2 m_e \nu_o^2}. \quad (2.25)$$

It is relevant to note that systems with a large oscillation constant, i.e., with a large restoring force, are difficult to polarize. In the case of nuclei, this is analogous to a large symmetry energy acting as the restoring force.

To make the SHO model more realistic, a time dependent electric field with amplitude E_o can be introduced, then by Newton's second law we have the following equation of motion,

$$m_e \frac{d^2 x}{dt^2} + kx = eE_o \cos(\omega t). \quad (2.26)$$

Upon solving Eq. 2.26, two solutions are obtained, a particular solution,

$$x_p(t) = \frac{eE_o}{m_e(\omega_o^2 - \omega^2)} \cos(\omega t), \quad (2.27)$$

and a complementary one, $x_c(t) = x_p(t)$, with $\omega_o^2 = k/m_e$ being the threshold frequency. This is analogous to the complete overlap of eigenstates before and after perturbation in quantum mechanics, for example the ground state (s-orbital) in the nuclear SM. Once again, the combination of Eqs. 2.19, 2.23 and 2.24 yields,

$$x_p(t) = \frac{e^2}{4\pi^2 m_e(\omega_o^2 - \omega^2)}. \quad (2.28)$$

Another realization of the SHO model is including damping, critical damping in particular. A damping system is described by,

$$\frac{d^2 x}{dt^2} + 2\beta \frac{dx}{dt} + \omega_o^2 x = \frac{eE_o}{m_e} \cos(\omega t). \quad (2.29)$$

A complementary solution of Eq. 2.29 represents transient effects for $t \gg 1/\beta$, where β is the damping coefficient determining the damping force magnitude. Equation 2.29 has a particular solution of the type,

$$x_p(t) = \frac{eE_o \cos(\omega t - \delta)}{m_e \sqrt{(\omega_o^2 - \omega^2)^2 + 4\beta\omega^2}}, \quad (2.30)$$

where a driving force induced by an external electric field is included, δ is the phase difference between the resultant motion and the electric field [69]. Polarization occurs due to oscillations which we assume to have sufficiently small displacements so that the elastic limits are not exceeded. Once more the polarizability is given by [69],

$$\alpha = \frac{e^2}{2\pi\sqrt{m_e(\omega_0^2 - \omega^2) + \frac{\beta\omega^2}{\pi^2}}}, \quad (2.31)$$

where an assumption that $\delta = 0$ was made. Under this assumption the time dependence of α vanishes.

Moreover, a resonance is now allowed contrary to the cases with no damping. The GDR is one of the damping mechanisms of the restoring force generated by the isovector density $(\rho_n - \rho_p)/\rho$. The latter is analogous to the classical case discussed above. So far only the classical description of polarizability is considered. Microscopic systems such as atoms and nuclei manifest quantum effects. Therefore it is equally important to also consider a quantum mechanical description of α .

2.2.2 Quantum mechanical polarizability

Suppose that a hydrogen atom is subjected to a uniform external electric field with coordinates (x, y, z) . The external field interacts with the atom, with a perturbation Hamiltonian H' i.e., the potential energy of the atom in the electric field, $H' = -eEz$, is added to the initial Hamiltonian H_o . A Hamiltonian describing the system is [70],

$$H = H_o - eEz. \quad (2.32)$$

Then the Schrödinger equation of the perturbed system is,

$$H\psi = -\frac{\hbar^2}{2m}\nabla^2\psi - \frac{e^2}{r}\psi + eErcos\theta\psi. \quad (2.33)$$

The calculations are done in the Coulomb field described in the spherical coordinate system, where $z = rcos\theta$ and a complete solution of the preceding equation has been carried out in [70]. The wave function is,

$$\psi = e^{-\frac{r}{a}} \left[1 - \frac{a^2 E}{e} cos\theta \left(\frac{r}{a} + \frac{r^2}{2a^2} \right) \right]. \quad (2.34)$$

An alternative treatment of polarizability can be done by invoking non-degenerate second order perturbation theory, where the wave function is given by [70],

$$\Psi = \psi_o + eE \sum_n \frac{Z_{on}\psi_n}{E_n - E_o}, \quad (2.35)$$

where ψ_o is the ground state wave function and ψ_n the wave function of the n^{th} excited state, both dependent on (r, θ, ϕ) , and,

$$Z_{on} = \int \psi_n^* \hat{E} 1 \psi_o d\tau \equiv \langle \psi_n | \hat{E} 1 | \psi_o \rangle. \quad (2.36)$$

The perturbation by the electric field causes a change in the charge distribution, which can be described by the charge density distribution,

$$\rho(r, \theta, \phi) = e|\psi_o|^2 + eE \sum_n \left(\frac{Z_{on}\psi_n\psi_o^*}{E_n - E_o} + \left(\frac{Z_{on}\psi_n\psi_o^*}{E_n - E_o} \right)^* \right). \quad (2.37)$$

As the sum consists of non-symmetric terms $\psi_n\psi_o^*$, a dipole moment is generated due to the non-symmetric charge distribution. The dipole moment is given by,

$$D = \int z\rho(r, \theta, \phi)d\tau . \quad (2.38)$$

Upon substitution for charge density and integrating Eq. 2.38, the scalar electric dipole polarizability is given by,

$$\alpha = 2e^2 \sum_n \frac{|Z_{on}|^2}{E_n - E_o} . \quad (2.39)$$

Note that Eq. 2.39 indicates structural reliance; hence allowing the calculation of α , at a specific n^{th} excited state, and yielding a discrete definition of α dependent on energy and the strength of the dipole operator $\hat{E}1$. Furthermore, strong dipole transitions (generating the GDR) dominate the sum rule (Eq. 2.39) at energies $E_\gamma \geq S_n$ due to the high transition probability $|Z_{on}|^2$. At lower energies there is a strong competition between electric and magnetic dipole transitions particularly for medium-mass and light nuclei.

In order to relate the classical and quantum mechanical pictures of α a dimensionless quantity, the oscillator strength function f_{0n} [70], is introduced,

$$f_{0n} = \frac{2m}{\hbar^2} (E_n - E_o) |Z_{on}|^2 . \quad (2.40)$$

This is an oscillator strength for a transition $|n\rangle \rightarrow |0\rangle$. One can write $E_n - E_o = h\nu = E_\gamma$, then polarizability can be defined as,

$$\alpha = \frac{e^2}{4\pi^2 m} \sum_n \frac{f_{0n}}{\nu_n} . \quad (2.41)$$

Alternatively,

$$\alpha = \frac{e^2}{4\pi^2 m} \sum_n \frac{f_{0n}}{E_\gamma^2} . \quad (2.42)$$

This result can be directly applied to a nuclear system, where E_γ is the transition energy from the n^{th} state to the ground state, resulting in another discrete definition of α .

According to non-degenerate and time-independent perturbation theory the change in energy of eigenstates characterized by quantum numbers n, l and m in the presence of an electric field E is,

$$\Delta E_{nlm} = eE \langle nlm | \hat{E}1 | nlm \rangle + e^2 E \sum_{n'l'm'=nlm} \frac{|\langle nlm | \hat{E}1 | n'l'm' \rangle|^2}{E_{nlm} - E_{n'l'm'}} . \quad (2.43)$$

The sum in the RHS of Eq. 2.43 can be reduced by the fact that most of the terms in the sum are zero. Reduction of the sum results from applying the selection rules derived from the $[L_z, \hat{E}1]$ and $[L^2, \hat{E}1]$ commutator rules as follows,

$$\langle nlm|\hat{E}1|n'l'm'\rangle = \begin{cases} 0 & m' \neq m \\ 0 & l' \neq l+1 \end{cases}$$

First order perturbation in Eq. 2.43 vanishes. The result is known as the quadratic Stark Effect.

$$\Delta E_{nlm} = e^2 E^2 \sum_{n'l'=l\pm 1} \frac{|\langle nlm|\hat{E}1|n'l'm'\rangle|^2}{E_{nlm} - E_{n'l'm'}}. \quad (2.44)$$

It follows that α can then be defined in terms of the energy shifts between eigenstates,

$$\Delta E_{nlm} = -\frac{\alpha_{nlm}}{2} E^2. \quad (2.45)$$

Therefore,

$$\alpha_{nlm} = 2e^2 \sum_{n'l'=l\pm 1} \frac{|\langle nlm|\hat{E}1|n'l'm'\rangle|^2}{E_{n'l'm'} - E_{nlm}}. \quad (2.46)$$

Note the independence of α_{nlm} from the magnetic quantum number m , constant in the sum rule above, which implies the existence of magnetic polarizability or susceptibility.

When matter is subject to a magnetic field the response to the field is represented by the magnetic susceptibility χ_{M1} composed of paramagnetic (χ_p) and diamagnetic (χ_d) components and characterizes the strength of magnetic polarizability $\beta_{M1} = \chi_{M1} \cdot \mathbf{B}$, where \mathbf{B} is the magnetic field strength,

$$\begin{aligned} \chi_{M1} &= \chi_p + \chi_d \\ &= 2 \sum_n \frac{\langle i \| \hat{M}1 \| n \rangle \langle n \| \hat{M}1 \| i \rangle}{E_\gamma} - \frac{Ze^2}{6Mc^2} \langle r^2 \rangle. \end{aligned} \quad (2.47)$$

Thus we have for the total σ_{-2} values [72],

$$\sigma_{-2} = \int \frac{\sigma(E_\gamma)}{E_\gamma^2} dE_\gamma = \frac{2\pi^2}{\hbar c} (\alpha_{E1} + \beta_{M1}). \quad (2.48)$$

We can deduce from Eq. 2.47 that paramagnetic susceptibility is prominent in nuclei with strong $M1$ transitions to the ground state $|i\rangle$. This is typical of spin-flip transitions with low E_γ . Alternatively prominent paramagnetic susceptibility arises from the enhancement of permanent magnetic dipole moments. This was observed on light nuclei with $A < 20$, particularly on ${}^6,7\text{Li}$ [72]. Paramagnetism is supposed to be negligible for heavy nuclei with $A > 60$, where the diamagnetic susceptibility dominates as predicted by the IPSM [71]. Additionally, it is evident that diamagnetism according to its definition in Eq. 2.47 is present in all nuclei and negative due to energy conservation or Lenz's law. That is, the current induced by the magnetic field \mathbf{B} on the nucleus generates a magnetic field opposing \mathbf{B} , otherwise one could generate infinite energy from electromagnetic interactions.

2.2.3 Hydrodynamic polarizability

The hydrodynamic model of the nucleus was first proposed by Migdal in 1944 [2]. Migdal's calculations of α using a semi-classical treatment will be revised in this section. He proposed that the nucleus is a system of inter-penetrating proton and neutron fluids with densities ρ_p and ρ_n , respectively. The fluid is spherically shaped with radius R such that $\rho = \rho_n + \rho_p$ is constant. Furthermore, the nuclear symmetry energy is assumed to be uniformly distributed throughout the nucleus and defined as [2, 26],

$$a_{sym}(A) = a_{sym} \frac{(N - Z)^2}{A}, \quad (2.49)$$

which corresponds to a symmetry energy density,

$$F_\rho = a_{sym} \frac{(\rho_n - \rho_p)^2}{\rho}. \quad (2.50)$$

In the presence of an electric field with strength E , a dipole moment is created due to a linear increase in the proton fluid density in the direction of E assumed to be the positive z -direction. In absence of an electric field the proton fluid density is represented by ρ_{op} . Therefore [2, 26],

$$\rho_p = \rho_{op} + \rho' z, \quad (2.51)$$

It was shown in [2] that the residual interaction (proton-proton) is negligible, contributing less than 6% to the total nuclear polarizability. The energy density at any point in the nucleus is given by [2],

$$F_\rho = \frac{4\pi R^3}{3} \left[\frac{a_{sym}(\rho - 2\rho_{op})}{\rho} + \frac{4a_{sym}r^2}{5\rho} - \frac{e\rho'ER^2}{5} \right]. \quad (2.52)$$

To determine the parameter ρ' , the nuclear symmetry energy density F_ρ is minimized with respect to ρ_p . It follows from Eq. 2.52 that,

$$\rho' = \frac{eE\rho}{8a_{sym}}. \quad (2.53)$$

Therefore the incremented dipole moment density is,

$$e(\rho - \rho_{op})z = e\rho'z^2. \quad (2.54)$$

Finally, the polarizability of the nucleus is found by using Eq. 2.54 as [2, 26],

$$\alpha = \frac{e}{E} \int \rho' z^2 = \frac{e^2 R^2 A}{40a_{sym}}. \quad (2.55)$$

In the previous section α was calculated by second order perturbation theory. Migdal and co-workers showed that α is proportional to σ_{-2} (see Chapter 1 [2, 18]),

$$\alpha = \frac{\hbar c}{2\pi^2} \sigma_{-2} = \frac{\hbar c}{2\pi^2} \int_0^{E_{\gamma max}} \frac{\sigma_{total}(E_\gamma)}{E_\gamma^2} dE_\gamma. \quad (2.56)$$

Comparing Eqs. 2.55 and 2.56 yields the following definition of σ_{-2} ,

$$\sigma_{-2} = 2.25A^{5/3} \mu\text{b}/\text{MeV} , \quad (2.57)$$

which can also be described discretely [26],

$$\sigma_{-2} = \frac{2\pi^2}{\hbar c} \left(\frac{e^2 \hbar^2}{m} \right) \sum_n \frac{f_{on}}{(E_n - E_o)^2}. \quad (2.58)$$

Therefore total α can be measured experimentally using the σ_{-2} values according to the linear relationship (Eq. 2.56). The hydrodynamic model discussed above is built under the assumption that nuclei are spherical. However, it is known that nuclei are generally deformed in both excited and ground states with some manifesting shape coexistence [73], implying spontaneous symmetry breaking. Therefore, in order to build a more realistic and complete picture of α , the deformation of the nucleus has to be taken into consideration.

2.2.4 Polarizability and Deformation

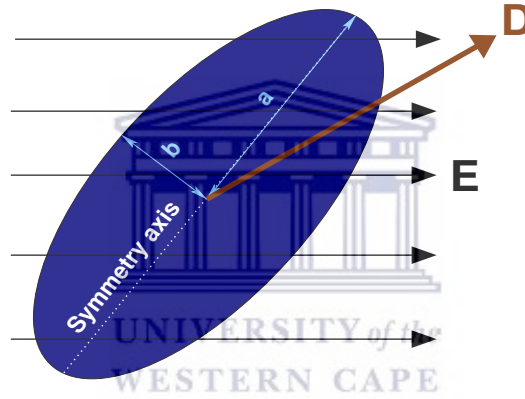


Figure 2.8: Deformed nucleus in an electric field. The interaction between the electric field \mathbf{E} and the electric dipole moment \mathbf{D} , which tends to align with the symmetry axis, produces a torque which causes rotation.

As shown in Fig. 2.8, suppose that an axially deformed nucleus (i.e., with only quadrupole deformation) is subjected to an external homogeneous electric field \mathbf{E} with strength E . The field induces a dipole moment \mathbf{D} which can only be in the direction of \mathbf{E} if the polarization vector of \mathbf{E} is parallel to one of the three principal axes defined for a deformed nucleus [74]. It is known that the GDR shape of a deformed nucleus splits into different peaks. According to the hydrodynamic model, this means that a fraction of nucleons oscillate along one of the principal axes, hence the split of the GDR shape. The parameter that approximates this fraction will be defined later. Additionally, the splitting indicates polarizability in the direction of the i^{th} principal axis, $i = x, y, z$. Thus, polarizability is defined by [18],

$$\alpha_{xx} = \frac{e^2 \epsilon_o p_o}{6\pi a_{sym}} \int_{\tau} x^2 d\tau = \frac{a^2}{R^2} \frac{e^2 R^2}{40 a_{sym}} = \frac{a^2}{R^2} \alpha_o. \quad (2.59)$$

Similarly,

$$\alpha_{yy} = \frac{b^2}{R^2} \frac{e^2 R^2}{40a_{sym}} = \frac{b^2}{R^2} \alpha_o, \quad (2.60)$$

where α_o is the static nuclear polarizability calculated for a spherical nucleus (Eq. 2.55), a and b are the length of the major and minor semi-axis of an ellipsoid describing the nuclear shape. Therefore α can be defined as a rank-2 tensor [18, 74].

Migdal [18] calculated the nuclear photo-effect which was later modified by Levinger [26]. It was found that E_{GDR} can be given by,

$$E_{GDR}^2 = \frac{\int_0^\infty \sigma_{total}(E_\gamma) dE_\gamma}{\int_0^\infty \frac{\sigma_{total}(E_\gamma)}{E_\gamma^2} dE_\gamma} = \int_0^\infty \frac{\sigma(E_\gamma)}{2\pi^2 \alpha_o} dE_\gamma = \frac{\sigma_{total}}{\sigma_{-2}}. \quad (2.61)$$

Using Eq. 2.61 we can find the position of the resonance along each axis, expressed in terms of the polarizability tensor components [18],

$$E_{GDR(x)}^2 = \int_0^\infty \frac{\sigma_{total}(E_\gamma)}{2\pi^2 \alpha_{xx}} dE_\gamma. \quad (2.62)$$

Similarly,

$$E_{GDR(y)}^2 = \int_0^\infty \frac{\sigma_{total}(E_\gamma)}{2\pi^2 \alpha_{yy}} dE_\gamma. \quad (2.63)$$

The resonance energies along the two principal axis can be approximated using the parameters defining the nuclear shape as,

$$E_{GDR(y)} \sim E_{GDR(x)} = E_{GDR} \left(\frac{R}{b} \approx \frac{R}{a} \right). \quad (2.64)$$

In nearly-spherical and non super-deformed nuclei Eq. 2.55 is valid since $\frac{E_{GDR(x)}}{E_{GDR(y)}} \approx 1$. Note that $\left(\frac{E_{GDR(x)}}{E_{GDR(y)}} \right)^2 \sim \left(\frac{b}{a} \right)^2$ is also known as the deformation parameter. This parameter can be accurately defined by [75],

$$\frac{E_{GDR(x)}}{E_{GDR(y)}} = 0.911 \frac{a}{b} + 0.039. \quad (2.65)$$

A more realistic case would be assuming that the nucleus is randomly oriented, i.e. the polarization vector is not necessarily parallel to any of the principal axes. Therefore the mean photo-absorption cross section is calculated as follows [75],

$$\langle \sigma(E_\gamma) \rangle = \frac{1}{4\pi} \int [\sigma_x(E_\gamma) \cos^2 \theta + \sigma_y(E_\gamma) \sin^2 \theta] d\Omega, \quad (2.66)$$

where it was assumed that x is the rotational symmetry axis, σ_x and σ_y are the photo-absorption cross sections along the principal axes x and y , respectively. Note the dependence of the cross section on spacial angles due to the random orientation of the nucleus.

Another remarkable feature of the GDR is that it allows the determination of nuclear shapes from its splitting using the resonance width and strength. When $E_{GDR(x)} - E_{GDR(y)} < \frac{1}{2}\bar{\Gamma}$, the GDR shape consists of one broadened peak (see Fig. 2.9). Here $\bar{\Gamma}$ is the average resonance width of the two peaks centered at $E_{GDR(x)}$ and $E_{GDR(y)}$. The single broad peak implies a spherically shaped nucleus (charge distribution). Whereas if $E_{GDR(x)} - E_{GDR(y)} > \bar{\Gamma}$ two peaks appear in the GDR shape. For tri-axially shaped nuclei three peaks appear as shown at the bottom of Fig. 2.9. Treating the x -axis (major axis) as a rotational symmetry axis, it follows that for prolate nuclei with intrinsic quadrupole moment $Q_o > 0$, (i.e., $a > b$) the larger peak is centered at a higher energy. For oblate nuclei, $Q_o < 0$, $b > a$, the large peak is centered at a lower energy as for the case of ^{126}Cs shown in Fig. 2.9. At this point it is equally important to note the fact that the E1 dipole polarizability is a second order effect in Coulomb excitation theory and competes with the reorientation effect. One can evaluate the nuclear polarizability first excited state in ^{17}O which has $J = \frac{1}{2}$, implying that the spectroscopic quadrupole moment $Q_s(1/2^+) = 0$ [76].

The polarization potential V_{pol} resulting from considering deformation of nuclei is defined by [74],

$$V_{pol} = -\alpha_o E^2 \left[1 + 2 \sum_{\mu} \alpha_{2\mu} Y_{2\mu}(\theta, \phi) \right], \quad (2.67)$$

where $\alpha_{2\mu}$ is the deformation parameter corresponding with μ state, $Y_{2\mu}(\theta, \phi)$ are the real spherical harmonics dependent on spacial angles θ and ϕ . V_{pol} tends to reduce the total quadrupole interaction,

$$V_Q = V_{pol}(t) + V_{E2}(t), \quad (2.68)$$

where $V_{E2}(t)$ is the electric quadrupole potential. Particularly for light nuclei, where large α or κ values are generally observed for the ground and first excitation levels. This is the case for ^{10}Be with $\kappa(g.s.) = 2.7$ [52] and ^{12}C with $\kappa(g.s.) = 1.5$ and $\kappa(2_1^+) = 2.1$ [32]. It is also interesting to note that κ seems to increase with increasing excitation energy.

2.3 Low-energy enhancement of the photon-strength functions

As stated in §1.1 the LEE of the photon strength function $f(E_\gamma)$ is observed as an up-bend in the low energy tail below $E_\gamma \approx 4$ MeV in light and medium mass nuclei such as $^{44,45}\text{Sc}$ [79], $^{93-98}\text{Mo}$ [80] and recently in heavy mass nuclei $^{151,153}\text{Sm}$ [83]. The Oslo method [81, 82] was applied when the LEE was observed for the first time, using nuclear reactions such as ($^3\text{He}, ^3\text{He}'$), (p,d) and (d,p). To verify if the up-bend was not due to systematic errors in the Oslo method an utterly different experimental design and analysis technique was employed [84], which confirmed the existence of the LEE. This was done for ^{95}Mo , as shown in Fig. 2.10 below, where $f(E_\gamma)$ was measured at various initial excitation energies.

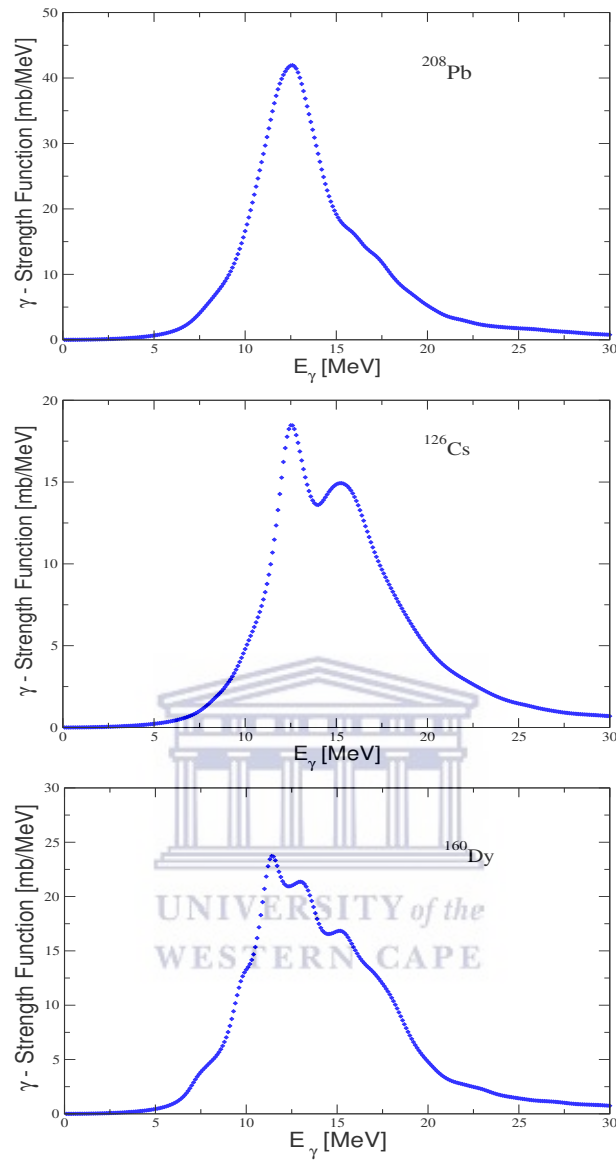


Figure 2.9: Calculated $f(E_\gamma)$ for ^{208}Pb , ^{126}Cs and ^{160}Dy showing a GDR shape with a single peak (spherical), two peaks (oblate) and three unequal peaks (triaxially deformed), respectively. The strength functions are computed within the QRPA model [77, 78].

The physical origin of this up-bend of $f(E_\gamma)$ at low E_γ remains unknown. Experimentally, it is clear that the LEE presents a dominant dipole radiation [47, 85], but whether its nature is either electric or magnetic remains unresolved [86]. The recent polarization asymmetry measurements of γ rays in ^{56}Fe using GRETINA tracking detectors yield inconclusive results, although rather suggests an admixture of electric and magnetic dipole radiation, with a small bias towards a

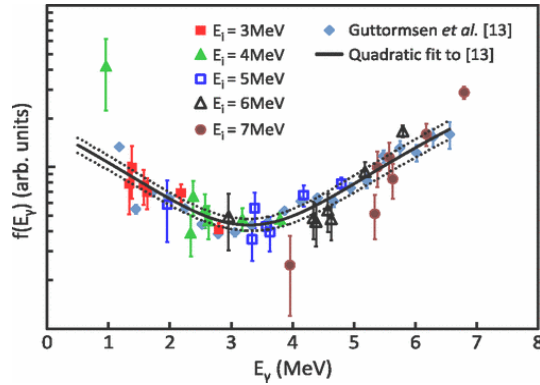


Figure 2.10: The comparison of ^{95}Mo $f(E_\gamma)$ s measured using the Oslo method (filled blue diamonds) and the alternative technique using primary γ -ray decay from the quasi-continuum to individual low-lying discrete levels [84].

magnetic character at $E_\gamma = 1.5 - 2.0$ MeV [86], as shown in Fig. 2.11.

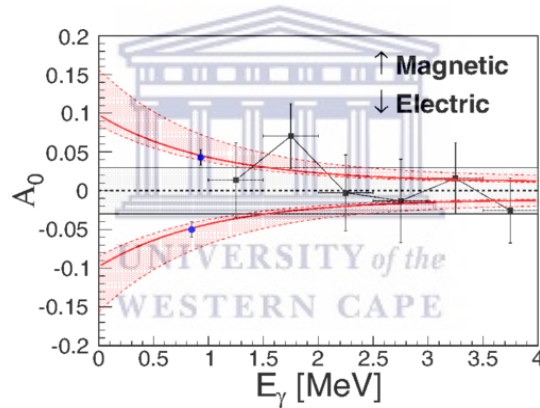


Figure 2.11: The polarization asymmetry A_o as a function of primary γ -ray energies. The red-solid line represents expected A_o assuming a linear polarization $P = 0.30$ with corresponding uncertainty range denoted by the red band, the grey band represents the statistical uncertainty of measuring a uniform distribution [86].

Two competing scenarios are theoretically proposed to explain the low- E_γ anomaly. Using the thermal continuum quasi-random phase approximation (TCQRPA), Litvinova and Belov propose that low-frequency electric-dipole $E1$ excitations from the hot-quasi-continuum to the continuum give rise to the up-bend in $f(E_\gamma)$ [87], as denoted by red dashed and solid lines in Fig. 2.12. Assuming spherically shaped nuclei, where the excitations (decays) are interpreted conceptually in terms of a microscopic many-body approach built on the thermal mean-field description of the compound nucleus, by requiring well defined single-particle states at moderate temperatures (i.e. in the quasi-continuum)

and elimination of the translational degree of freedom. Figure 2.13 illustrates $f(E_\gamma)$ calculation from the TCQRPA model for even-even Mo isotopes at various temperatures.

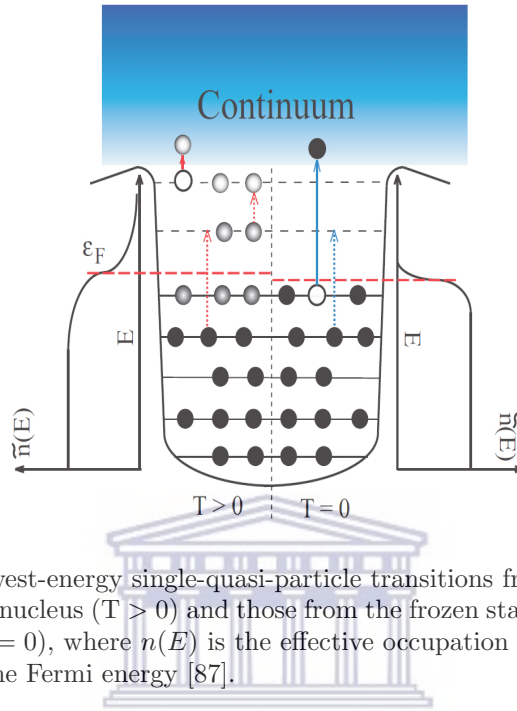


Figure 2.12: Lowest-energy single-quasi-particle transitions from excited states in an compound nucleus ($T > 0$) and those from the frozen states in the ground-state nucleus ($T = 0$), where $n(E)$ is the effective occupation probability distribution and ε_F the Fermi energy [87].

Contrarily, SM calculations predict that such an enhancement has a magnetic-dipole $M1$ character. Schwengner and collaborators suggest that the up-bend arises from active high- j proton and neutron orbits near the Fermi surface with magnetic moments adding up coherently [88]; a similar mechanism to the magnetic rotation [89, 90] or two-phonon mixed-symmetry states [91, 92] found for nearly spherical nuclei in the mass $A = 90$ region. Figure 2.14 presents $f(E_\gamma)$ obtained from SM calculations and compared with experimental data. Specifically, these calculations included only the pf shell yielding more than $6 \cdot 10^6$ states up to excitation energies of ≈ 8 MeV. In a complementary picture, Brown and Larsen suggest that the up-bend arises because of the large $M1$ diagonal matrix elements of high- ℓ orbitals [93].

Additionally as illustrated in Fig. 2.15, Sieja computed both $E1$ and $M1$ strengths in ^{44}Sc on equal footing from large-scale SM calculations in the $sd - pf - gds$ model space and also supported the $M1$ character of the LEE in the $A \sim 50$ region against $E1$ contributions [94, 95].

Recently, large-scale SM calculations of neutron-rich ^{70}Ni using various effective interactions also support the $M1$ character for the LEE [96]. In principle, the validation of these SM predictions in the quasi-continuum region may be arguable as, for instance, they are structure dependent; hence, posing a fundamental

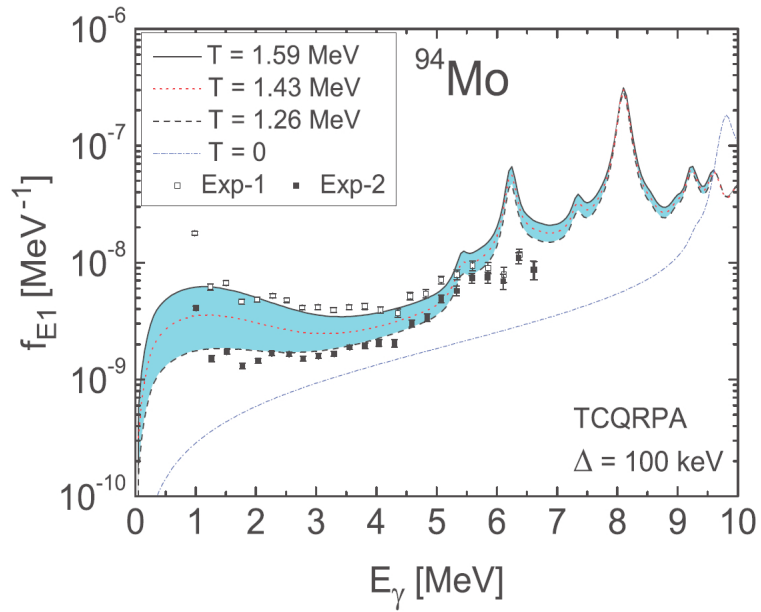


Figure 2.13: $f(E_{\gamma})$ for ^{94}Mo reproduced by the TCQRPA model at finite and $T = 0$ (ground state) temperatures compared with experimental data [87].

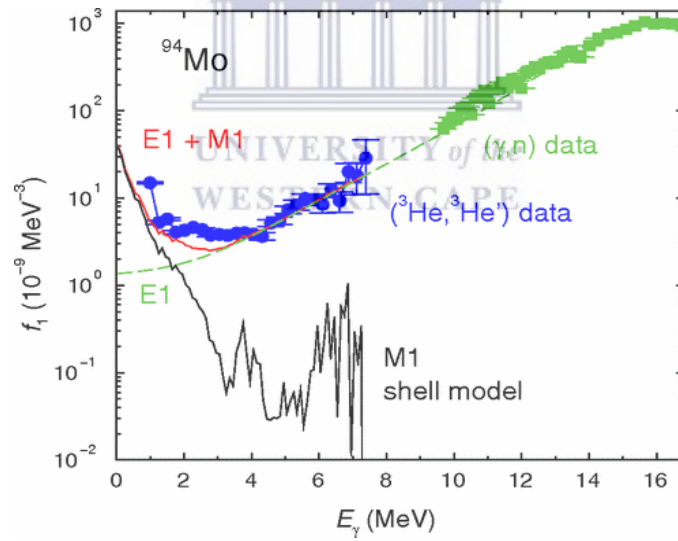


Figure 2.14: $f(E_{\gamma})$ for ^{94}Mo obtained from (γ, n) (green squares) and $(^3\text{He}, ^3\text{He}')$ (blue circles) measurements and the M1 strength function extracted from SM calculations (black solid line) [88].

question about the validity of the Brink-Axel hypothesis [41, 42]. The Brink-

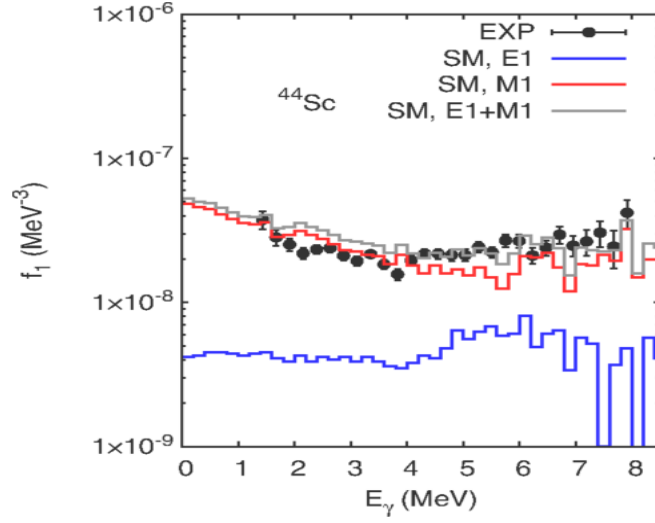


Figure 2.15: Comparison of experimental $f(E_\gamma)$ and SM calculations for ^{44}Sc [95].

Axel hypothesis¹ has been broadly confirmed experimentally with similar $f(E_\gamma)$ determined for different excitation-energy ranges around the quasi-continuum and above [43].

Amongst the GDR models discussed above, none is able to predict the LEE as an up-bend of the $f(E_\gamma)$ low energy tail without empirical modifications to reproduce the LEE. One could make an immediate deduction from the preceding: the LEE does not result from the collective behavior of the whole nucleus. Simon and coworkers [83] modeled the up-bend by applying the M1 and GDR spin-flip parametrization, resulting in an exponential $f(E_\gamma)$ as shown in Fig. 2.16,

$$f_{upbend}(E_\gamma) = C \exp(-\eta E_\gamma). \quad (2.69)$$

The coefficients in Eq. 2.69, were reported to be $C = 20 \cdot 10^{-7} \text{ MeV}^{-3}$ and $\eta = 5.0 \text{ MeV}^{-1}$, as determined for the $^{151,153}\text{Sm}$ isotopes.

However, Larsen and Goriely [64] modified the second term of the GLO in Eq. 2.16 to reproduce the up-bend by adjusting the temperature dependent width $\Gamma(E_\gamma, T_f)$ in the following way,

$$\Gamma(E_\gamma, T_f) = \frac{\Gamma_{GDR}}{E_{GDR}} \left(E_\gamma^2 + \frac{4\pi^2 T_f^2 E_{GDR}}{E_\gamma + \delta} \right). \quad (2.70)$$

Here they introduced the E_γ^{-1} dependence in the second term of the GLO, thus enhancing $f(E_\gamma)$ as $E_\gamma \rightarrow 0$. The constant parameter δ assures finite value of

¹The Brink-Axel hypothesis states that a GDR can be built on every state in a nucleus, and has recently been validated for γ -ray energies as low as 2 MeV [41, 42, 43]

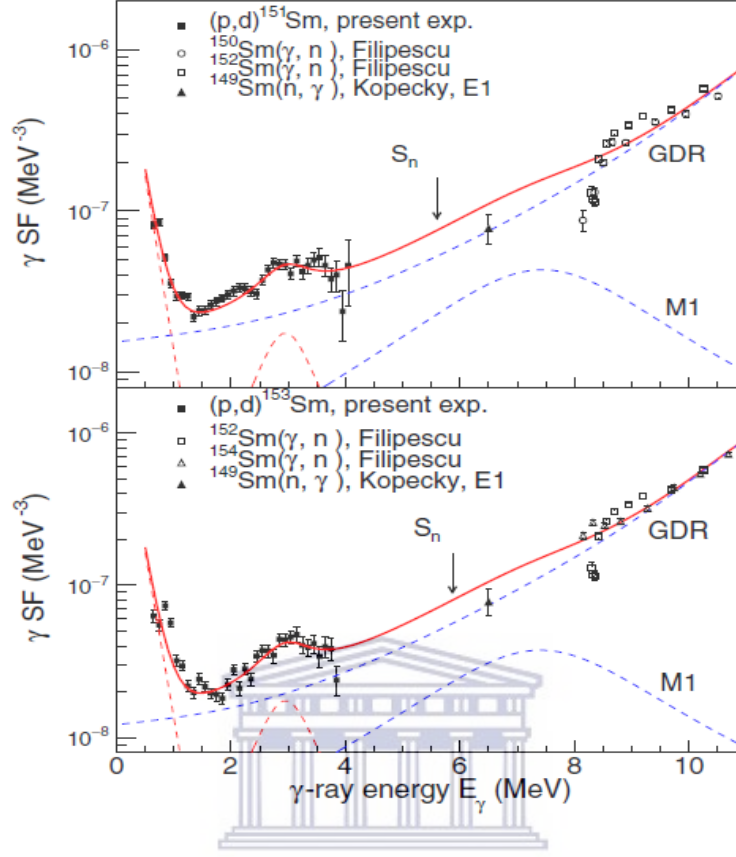


Figure 2.16: Experimental $f(E_\gamma)$ (open and shaded squares) compared with (red solid line) combined contributions of the GDR, M1 spin-flip, SR and the up-bend. The SR and the up-bend are represented by the red-dashed line [83]

the $f(E_\gamma)$. They also assume that T_f remains constant, which is not necessarily true. The final temperature is defined as,

$$T_f = \sqrt{\frac{E_i - \Delta - E_\gamma}{a}}, \quad (2.71)$$

where Δ is the pairing correction energy, and a the level density parameter at S_n . In their analysis of isotopes $^{93-98}\text{Mo}$ it was assumed that $\delta = 0.05$ MeV and $T_f = 0.16$ MeV. Indeed this model reproduces the up-bend with small discrepancies when compared with the experimental data, represented by the black dash-dot line in Fig. 2.7.

It is evident that the LEE can be reproduced by the SM [88, 94] and empirically corrected collective models i.e. Lorentzian functions [64], but none of these models state explicitly the physical origin of the LEE phenomenon. The LEE has a significant impact in various processes of nuclear physics and astrophysics, e.g. neutron capture reaction rates. In this study we investigate the impact of the LEE together with photo-nuclear cross sections on the nuclear polarizability.

2.4 Photo-nuclear Cross sections

The photo-nuclear cross sections calculated in this work are mainly dominated by the photo-neutron (γ, n) channel for medium and heavy nuclei. For light nuclei the charged particle emission (γ, p) is dominant due to the weaker Coulomb force. There are various experimental methods which can be employed in order to obtain photo-nuclear cross sections data namely,

- Bremsstrahlung radiation.
- Annihilation-photon method.
- Radiative neutron capture.
- Bremsstrahlung tagged photon.

Therefore we will do a brief review on photo-nuclear reactions, focusing on the first two methods listed above. As shown in Fig. 2.17, the interaction of photons with nuclear matter can result in ejection of nucleon(s), dependent on the energy of the incident photon or the photons may be scattered. The latter is referred to as photon scattering reaction (γ, γ'), favorable in studying nuclei at energies below neutron and proton threshold energies, S_n and S_p , respectively.



Figure 2.17: Schematic photonuclear reactions, showing photon scattering and single particle emission.

At moderate energies, electric dipole transitions are predominant in medium and heavy nuclei [97]. This implies that total photo-absorption cross sections,

$$\sigma_{total} = \int \sigma(E_\gamma) dE_\gamma, \quad (2.72)$$

can be calculated using the TRK electric dipole sum rule which shows model independence. To illustrate the TRK sum rule, we shall use the concept of electric dipole transitions of protons and neutrons with effective charges N/A and $-Z/A$, respectively, due to non negligible nucleon-nucleon interactions. The total or integrated cross section, from the double commutator $\frac{1}{2}[D, [H, D]]$, can be written as follows [98],

$$\begin{aligned}
\int \sigma(E_\gamma) dE_\gamma &= \frac{2\pi^2 e^2 \hbar}{mc} \left[\sum_{i=1}^Z \left(\frac{N}{A} \right)^2 f_i + \sum_{j=1}^N \left(\frac{-Z}{A} \right)^2 f_j \right] \\
&= \frac{2\pi^2 e^2 \hbar}{Mc} \frac{NZ}{A} \\
&\simeq \frac{0.06NZ}{A} \text{ [MeV-mb]},
\end{aligned} \tag{2.73}$$

where f_i and f_j represent summed oscillator strength functions associated with proton and neutron transitions, respectively. It is worth noting that the integrated cross section in Eq. 2.73 is derived using only the kinetic energy term of the Hamiltonian. Inclusion of nuclear potentials in the Hamiltonian tend to increase the dipole sum rule, the resulting deviations are measured by the polarizability parameter.

At higher E_γ energies there occur mechanisms such as the quasi deuteron (QD) effect, where a photon particularly interacts with the dipole moment of a deuteron – a proton-neutron pair inside the nucleus [99]. Furthermore, at energies above 140 MeV pion photo-production occurs (charge exchange currents). However, because of the $\frac{1}{E_\gamma^2}$ weight, our polarizability calculations are insensitive to the preceding two mechanisms, therefore we will not consider or accommodate them in the calculation of cross sections.

It is known from Maxwell's equations that accelerating or decelerating charged particles emit radiation. Therefore when an energetic electron moving towards a positively charged atomic nucleus it is accelerated due to the attraction between the two bodies or the electric field of the atomic nucleus, thus producing radiation (photons), this phenomenon is known as *bremsstrahlung*. The energy loss of the electron along its path can be described as follows [100],

$$-\frac{dE_o}{dx} = N_o \int_0^{v_o} h\nu \Phi_\nu d\nu, \tag{2.74}$$

N_o is the number of atoms per unit volume, Φ_ν the cross section of producing a photon energy with frequency ν . The integral can be resolved as,

$$\begin{aligned}
-\frac{dE_o}{dx} &= \frac{E_o}{x_o} \\
&= \frac{4e^2 r_e}{\hbar c} N_o Z^2 \ln \frac{183}{Z^{1/3}}
\end{aligned} \tag{2.75}$$

where x_o is the radiation length and r_e the fine structure constant. There also occurs electron-electron interaction which produces X-ray radiation. The radiation (photons) resulting from energy loss of an electron is then used to initiate the (γ , X) reaction channels. The bremsstrahlung spectrum is observed to be continuous – Gaussian distributed – due to random scattering of electrons producing the radiation.

An alternative method of generating the photons is the annihilation-photon method. This method operates by producing high energy positrons through pair production, thus producing beams of mono-energetic photons. In fact, most of the data in [25] were obtained using the annihilation-photon method. Here, a low mass target is bombarded by the positrons to reduce bremsstrahlung production; hence radiating a mono-energetic beam of photons in the forward direction [25, 101]. The annihilation-photon method is preferred when compared with other methods listed above, due to its ability to produce mono-energetic photons, yielding less contaminated spectra that are simultaneously obtained for the partial photo-neutron cross sections. However, the processes of annihilation and pair production will not be revised as these can be found in atomic physics text books [102].

It is evident that the GDR motion is common to all nuclei and can be complementary described in terms of both the single-particle SM and collective (hydrodynamic) models, for the ground state. Moreover, the GDR decay appears to be structural dependent and driven by asymmetry. The GDR phenomenon results in polarizability of dipole nature, the parameter of interest, that will be computed from photo-nuclear cross sections.

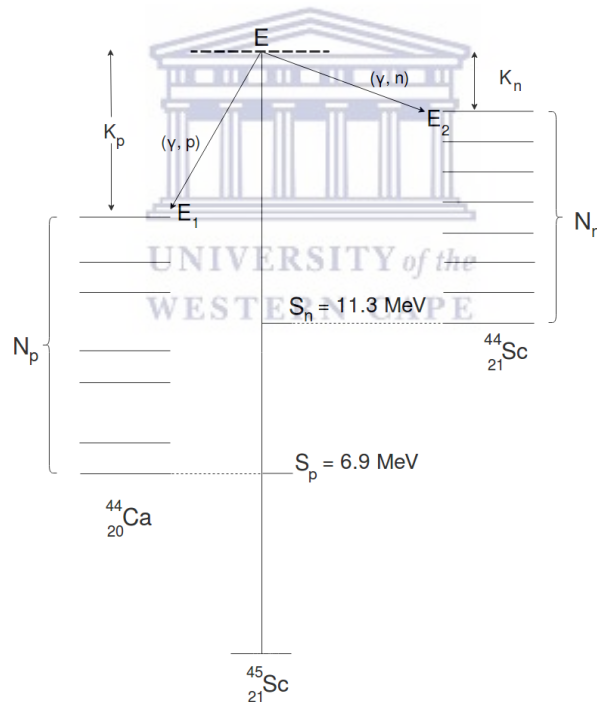


Figure 2.18: Schematic illustration of open proton and neutron channels for the isobar residual nuclei ^{44}Sc and ^{44}Ca .

Prior to the resonance energy, E_{GDR} , the lower energy part (above S_n and S_p) of the GDR cross section is dominated by neutron and proton emission yielding $\sigma(\gamma, n)$, $\sigma(\gamma, p)$ and $\sigma(\gamma, np)$. The statistical competition between $\sigma(\gamma, n)$ and

$\sigma(\gamma, p)$ presents a strong correlation with the N_p/N_n ratio [58],

$$\sigma(\gamma, p)/\sigma(\gamma, n) \propto N_p/N_n, \quad (2.76)$$

where N_p and N_n are the number of available levels below $E_1 = E - S_p - K_p$ and $E_2 = E - S_n - K_n$, i.e. the maximum possible excitation energies of the residual nuclei, respectively, with $E \approx E_{GDR}$ and K_p and K_n the kinetic energies (or penetrabilities) of the emitted protons and neutrons, respectively. Figure. 2.18 illustrates this for the case of ^{45}Sc . One assumes that the compound nucleus at $E \approx E_{GDR}$ emits protons and neutrons carrying out K_p and K_n , respectively. The residual nuclei ($A - 1$ isobars) are formed with maximum possible excitation energies E_1 and E_2 and the number of open proton and neutron channels below E_1 and E_2 determine the dominant nucleon emission channel. In general, the level density increases with excitation energy; hence, in the case of ^{45}Sc where $E_1 < E_2$ it is expected that $N_p/N_n \ll 1$. Moreover, due to the odd-odd nature of ^{44}Sc there are extra states that can be populated implying higher level density compared to the isobaric analogue ^{44}Ca with even-even nature. A similar argument applies for ^{51}V , with residual nuclei ^{50}Ti (even-even) which is in addition semi-magic with $N=28$ and ^{50}V (odd-odd). Trivially, the latter will have a larger level density and $N_p/N_n \ll 1$.

Including the $\sigma(\gamma, p)$ contribution increases the total photo-nuclear cross section and satisfies the TRK sum-rule in the $A \approx 90$ region. This will also be shown for self-conjugate and nuclei considered in this study. Contrarily, in the case of ^{92}Mo it was found $N_p/N_n = 1.95$, possibly suggesting that residual interaction terms must be included in the TRK sum-rule. Additionally, the ratio $\sigma(\gamma, p)/\sigma(\gamma, n)$ allows testing of isospin (T) impurities in T=0 nuclei [58].

The recently found LEE phenomenon, whose meaning and effects are being investigated, permits computations of cross sections at low energies. Therefore yielding more accurate total photo-nuclear cross sections and polarizability values in the quasi-continuum, assuming the validity of the Brink-Axel hypothesis because most of known photonuclear cross sections are measured in the ground state – particularly in Ref. [25].

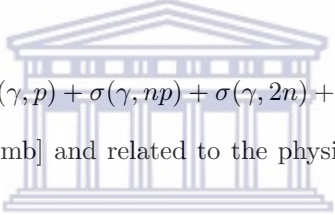
Chapter 3

Data Analysis and Results

Photo-nuclear data of the nuclei ^{45}Sc , ^{50}V , ^{51}V , ^{56}Fe , ^{76}Ge , ^{92}Zr , ^{95}Mo , $^{138,139}\text{La}$ and ^{153}Sm analyzed in this work consist of partial cross sections from various reaction channels. In heavy nuclei the (γ, n) reaction channel generally dominates and measurements of the photo-nuclear cross sections typically start at neutron threshold energies, S_n [25]. Therefore, the total cross section is calculated as follows:

$$\sigma_{total} = \sigma(\gamma, n) + \sigma(\gamma, p) + \sigma(\gamma, np) + \sigma(\gamma, 2n) + \sigma(\gamma, 3n) + \dots \quad (3.1)$$

measured in milli-barns [mb] and related to the physical quantities of interest σ_{-2} values, as follows:


$$\sigma_{-2} := \int_{E_{\gamma min}}^{E_{\gamma max}} \frac{\sigma_{total}(E_{\gamma})}{E_{\gamma}^2} dE_{\gamma}, \quad (3.2)$$

and the nuclear polarizability,

$$\alpha = \frac{\hbar c}{2\pi^2} \int_{E_{\gamma min}}^{E_{\gamma max}} \frac{\sigma_{total}(E_{\gamma})}{E_{\gamma}^2} dE_{\gamma}, \quad (3.3)$$

where $E_{\gamma max}$ and $E_{\gamma min} = 0$ are the maximum and minimum energy of integration. This energy range determines which nuclear reaction dynamics are considered in the calculation. At intermediate energies between S_n and $E_{\gamma} \approx 35$ MeV assuming $S_p > S_n$, the GDR is the dominant mode of excitation yielding,

$$\sigma_{GDR}(E_{\gamma}) = \sigma(\gamma, n) + \sigma(\gamma, p) + \sigma(\gamma, np) + \sigma(\gamma, 2n) + \sigma(\gamma, 2n) + \dots \quad (3.4)$$

At higher energies, ~ 150 MeV, the photo-absorption of a quasi-deuteron (QD) becomes significant, resulting to the following definition of the total cross section

$$\sigma_{total} := \sigma_{GDR}(E_{\gamma}) + \sigma_{QD}(E_{\gamma}). \quad (3.5)$$

However, in this study $E_{\gamma(max)}$ is in the range 20-50 MeV; hence, assuming that $\sigma_{GD}(E_{\gamma})$ contributions above pion threshold are negligible [26, 36, 37, 38]. All the selected nuclei in this study present a LEE of $f(E_{\gamma})$ in the quasi-continuum region, $E_{\gamma} < S_n$. Several mass regions were chosen in order to obtain a systematic study of LEE effects. Therefore, the total photo-nuclear cross sections must also include the LEE cross section data in order to realize the aim of this study as described in the next section. Accordingly,

$$\sigma_{total} = \sigma_{GDR}(E_{\gamma}) + \sigma_{LEE}(E_{\gamma}). \quad (3.6)$$

The multi-polarity of $\sigma_{LEE}(E_{\gamma})$ may include both electric and magnetic components of $f(E_{\gamma})$, i.e. for a particular nucleus, $\sigma_{LEE}(E_{\gamma})$ may be comprised of both electric and magnetic dipole components, yielding total polarizability $\beta_{M1} + \alpha_{E1}$. This has been shown in the case of ^{56}Fe , from angular distribution measurements [86] that were found to be consistent with dipole radiation. Moreover, recent calculations of the LEE in $f(E_{\gamma})$ for ^{44}Sc using large-scale SM calculations show the dominance of the magnetic dipole (M1) component at low E_{γ} [94].

The data are obtained from the International Atomic Energy Agency; Nuclear Data Services (NDS) and National Nuclear Data Center (NNDC). The partial and total photo-nuclear cross sections were obtained from databases under NDS i.e. EXFOR [103] and ENDF [104] in ASCII data file format. Decay and nuclear structure parameters were obtained from the ENSDF database under NNDC. These data were acquired in different eras at various laboratories. To be consistent, the majority of the data analyzed in this work were produced in photo-nuclear experiments performed at Saclay (France), Lawrence Livermore National laboratory (USA) and Moscow State University (Russia). Preference was given to data sets produced from the annihilation-photon method over other aforementioned methods in §2.4 due to its ability to produce mono-energetic photons yielding simultaneously partial photo-nuclear cross sections. The annihilation-photon experimental method is described according to the Saclay laboratory set up in Appendix B. Additionally, the LEE data were obtained from the Oslo Compilation of Level Densities and $f(E_{\gamma})$ [106].

In this chapter the findings from this study are presented, beginning with the systematics where all the assumptions, i.e. validity of the Brink-Axel hypothesis and methods are implemented, followed by discussion where all implications of the results are emphasized.

3.1 Systematics

3.1.1 Interpolation Method

The GDR data could be modeled with Lorentzian functions as explained in the previous chapter in order to calculate the parameters of interest i.e. α , σ_{-2} and σ_{total} . However, an interpolation method has been employed instead to compute the required quantities due to the failure of the unmodified Lorentzian functions to reproduce the LEE, as shown in Fig 3.1.

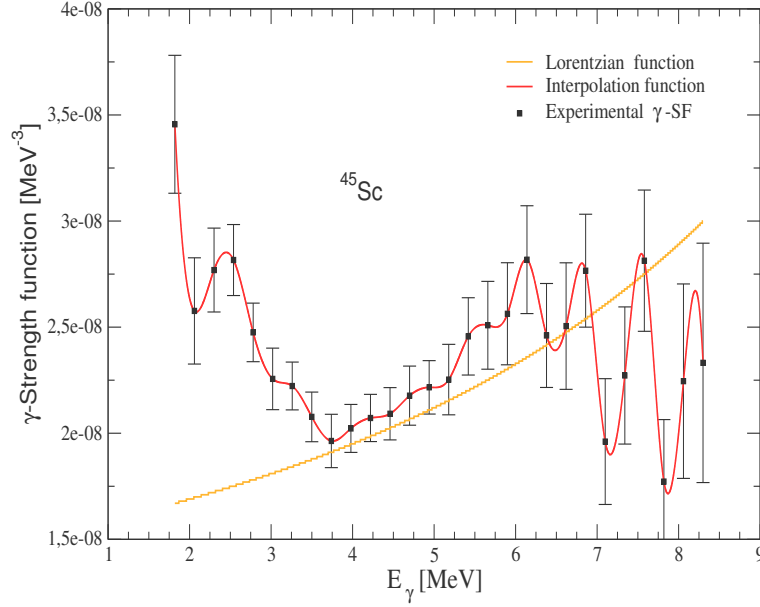


Figure 3.1: Interpolation function (solid red-line) of $f(E_\gamma)$ for ^{45}Sc and the low energy tail of a Lorentzian function (solid orange-line) in the LEE region.

The interpolation method is independent of the physical phenomena and operates by creating a function, cubic in this case, that interpolates (add data) between known or fixed data points. It is recommended that the data spacing (interval) of the independent variables (E_γ) to be small. Preferably ≤ 1 MeV, in order to reduce fluctuations of the interpolating functions, thus reducing systematic errors.

A program that takes in experimental data as input and computes σ_{-2} and σ_{total} values has been written in Python (see Appendix B for a detailed description of how the program operates). The program is divided into four parts as follows,

- Input of energies and cross sections data for a particular nucleus in arrays.
- Interpolation and numerical computation of the integrals, applying the trapezoidal rule method.
- Error propagation.
- Visualization of the data and fitting functions (interpolant) and results.

The data points with high uncertainties, e.g. exceeding 50%, reported from experiment were excluded, thus reducing the error of the interpolation. Around S_n , significant uncertainties are noted as $\sigma(\gamma, n) \rightarrow 0$ this may result from low statistics and indicates the less known structure of nuclei around S_n . Nonetheless, including these data points yields negligible change to σ_{-2} and σ_{total} values.

Table 3.1 presents the σ_{-2} and σ_{total} values of the considered nuclei available in the 1988 atlas of photo-neutron cross sections obtained with mono-energetic photons [25] (upper part) and those produced by the interpolation method (lower part). This comparison shows fair agreement, which proves the good reliance of the interpolation method.

Nucleus	$E_{\gamma_{min}}$ MeV	$E_{\gamma_{max}}$ MeV	σ_{total} Mev-mb	σ_{-2} mb/MeV
⁴⁵ Sc	11.3	28.1	399	1.05
⁵¹ V	11.1	27.8	531	1.65
⁷⁶ Ge	9.4	26.5	733	3.86
⁹² Zr	8.6	27.8	639	3.92
¹³⁹ La	8.8	24.3	1687	8.54
⁴⁵ Sc	11.3	28.1	396	1.06
⁵¹ V	11.1	27.8	449	1.38
⁷⁶ Ge	9.4	26.5	728	2.98
⁹² Zr	8.6	27.8	675	3.01
¹³⁹ La	8.8	24.3	1684	7.80

Table 3.1: The σ_{-2} and σ_{total} values obtained from Ref. [25] (upper part) and the interpolation method (lower part). A thick solid line separates the two methods.

One disadvantage of this method compared to the Lorentzian functions is the inability to estimate or predict the cross sections and $f(E_\gamma)$ in regions with no experimental data, hence independent of physical phenomena. In most cases there is a non-negligible gap between the GDR and LEE data sets, as observed for ¹⁵³Sm in Fig. 2.16, which includes the spin-flip M1 resonance. This gap results in prominent fluctuations of the interpolating function in a small region (i.e. enhanced standard deviation). Therefore, data from (γ, γ') , (n, γ) reactions and Evaluated Nuclear Data Files ENDF [104] are used to fill the gap, where necessary. Alternatively, data reproduced by Lorentzian functions can also be used and these data represent the total cross sections or $f(E_\gamma)$ instead of partial cross sections e.g. $\sigma(\gamma, p)$.

3.2 Results

The LEE data assumed to be of dipole nature obtained from [106] were converted to cross section as follows,

$$\sigma_{LEE}(E_\gamma) = 10\pi^2(\hbar c)^2 g_J f(E_\gamma) E_\gamma \text{ [mb]}, \quad (3.7)$$

where g_J is a statistical factor defined as,

$$g_J = \frac{2J+1}{2J_o+1}. \quad (3.8)$$

For $\sigma_{GDR}(E_\gamma)$ measurements in the ground state, J_o is the ground state spin and J the spin of a compound state. In the case of $J_o = 0$, typical of even-even nuclei, $g_J = 3$ assuming $J = 1$ for electric dipole transitions. Non-zero ground

state spin affects the value of g_J , the GDR strength, $S_{GDR}^{g.s.}$, and the magnitude of σ_{total} .

It is worth noting the magnitude of g_J , as it significantly affects $\sigma_{LEE}(E_\gamma)$ values. According to measurements [94, 95], the LEE originates from the hot-quasi-continuum or highly excited states. The statistical factor in either case has an average value $g_J = 1$ for dipole transitions, particularly for $J \rightarrow J$ and $\Delta J = 1$ transitions. As shown in Fig. 3.2, g_J asymptotically approaches unity for dipole transitions between high spin states; that is, $J \gtrsim 7$. Therefore, the statistical factor in Eq. 3.7 was set to $g_J = 1$ for all nuclei considered consequently resulting to spin independent $\sigma_{LEE}(E_\gamma)$.

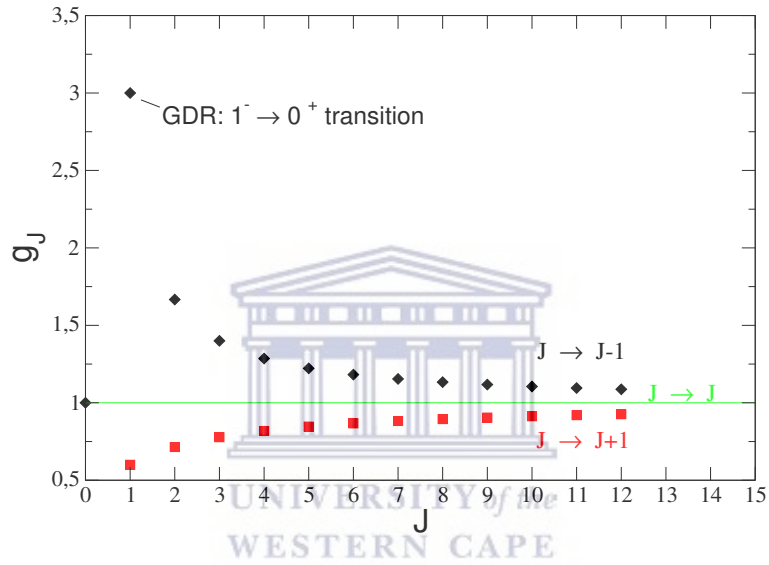


Figure 3.2: Showing the spin distribution of g_J for dipole transitions between states with $J = 1$ to $J = 12$.

The resulting $\sigma_{LEE}(E_\gamma)$ was then added to $\sigma_{GDR}(E_\gamma)$ according to Eq. 3.6 in order to compute the total cross section and its respective moments. As noted, there are missing data between the two aforementioned cross sections in the region $E_{\gamma(max)}^{LEE} - S_n, S_p$, i.e. the maximum energies at which the $f(E_\gamma)$ are measured up to and nucleon threshold energies. Figures 3.3 and 3.4 present the photo-nuclear cross sections for the nuclei studied in this work, showing no irregular behavior of the interpolating functions. The LEE data converted using Eq. 3.7 is shown in squares (green) with respective uncertainties and the experimental GDR cross section in diamonds (blue).

The width of the gap due to missing data varies for each isotope. Figure 3.5 shows for ^{45}Sc a gap width of 2.3 MeV once the $\sigma(\gamma, p)$ cross section is included, which yields a prominent increase on $S_{GDR}^{g.s.}$ and σ_{total} by approximately two orders of magnitude; hence, emphasizing the significance of $\sigma(\gamma, p)$ contributions to σ_{total} in medium mass nuclei.

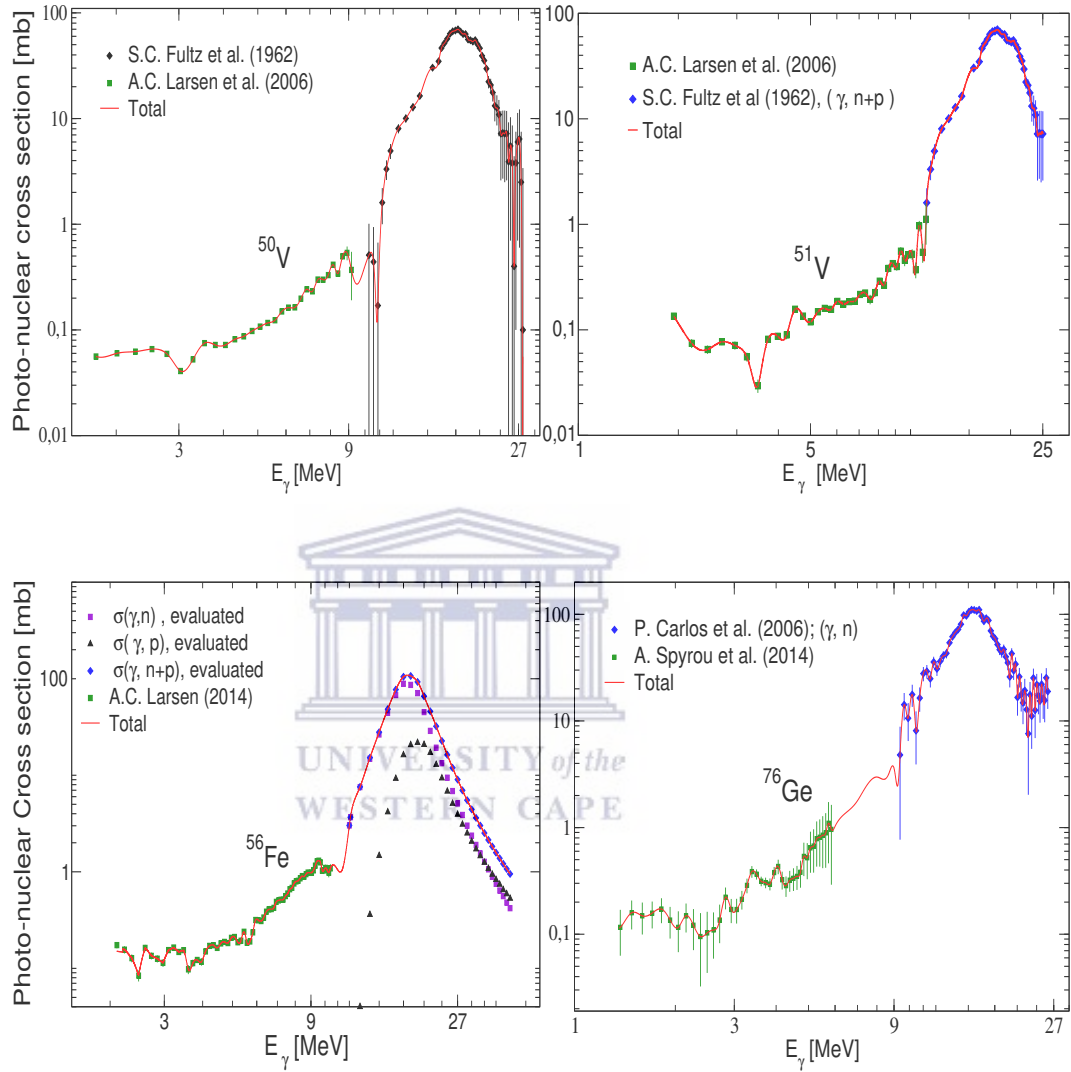


Figure 3.3: Experimental photo-nuclear cross section for ^{50}V , ^{51}V , ^{56}Fe and ^{76}Ge interpolated with a cubic-spline function (red solid line). Experimental data were obtained from references given in Table 3.2.

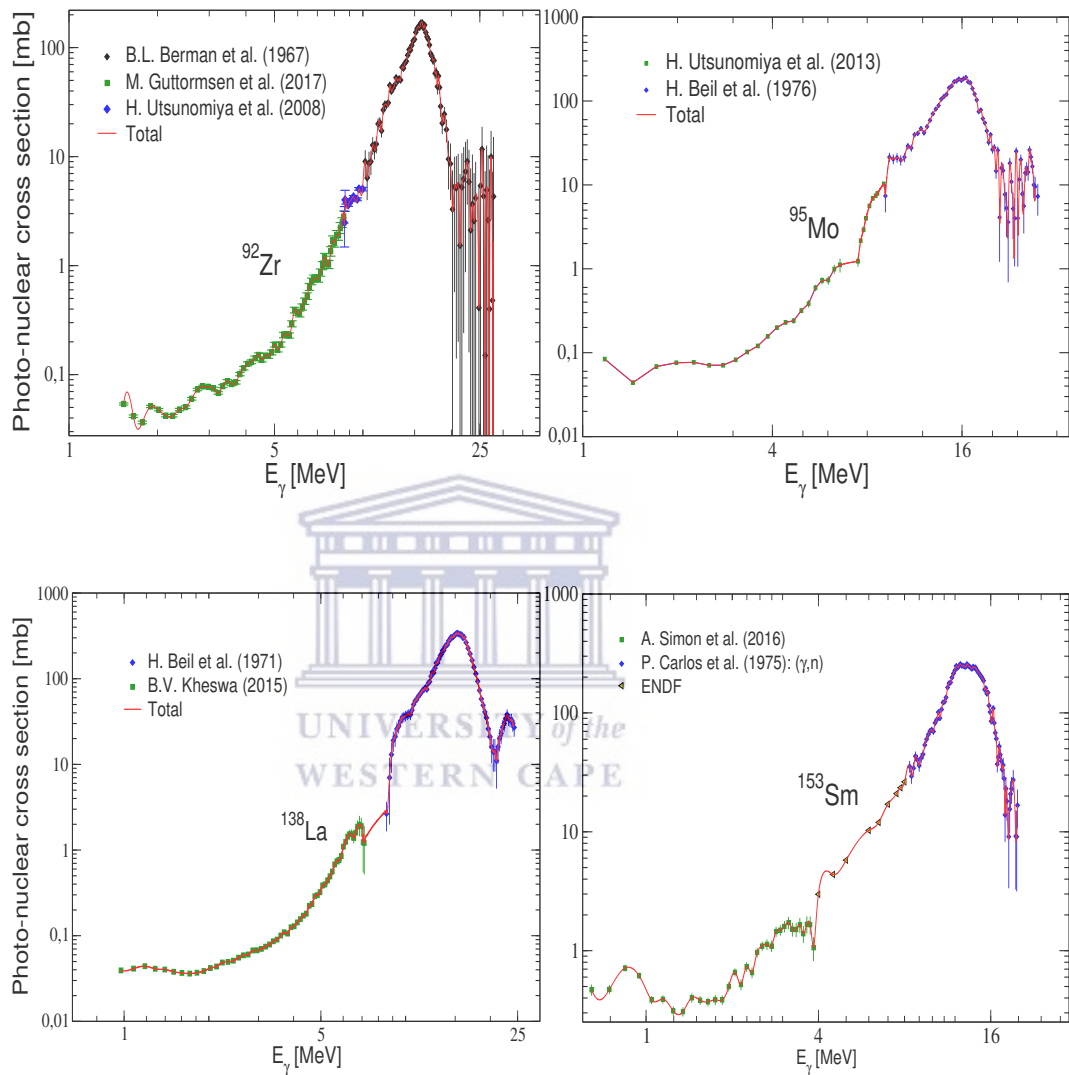


Figure 3.4: Experimental photo-nuclear cross section for ^{92}Zr , ^{95}Mo , ^{138}La and ^{135}Sm interpolated with a cubic-spline function (red solid line). Experimental data were obtained from references given in Table 3.2.

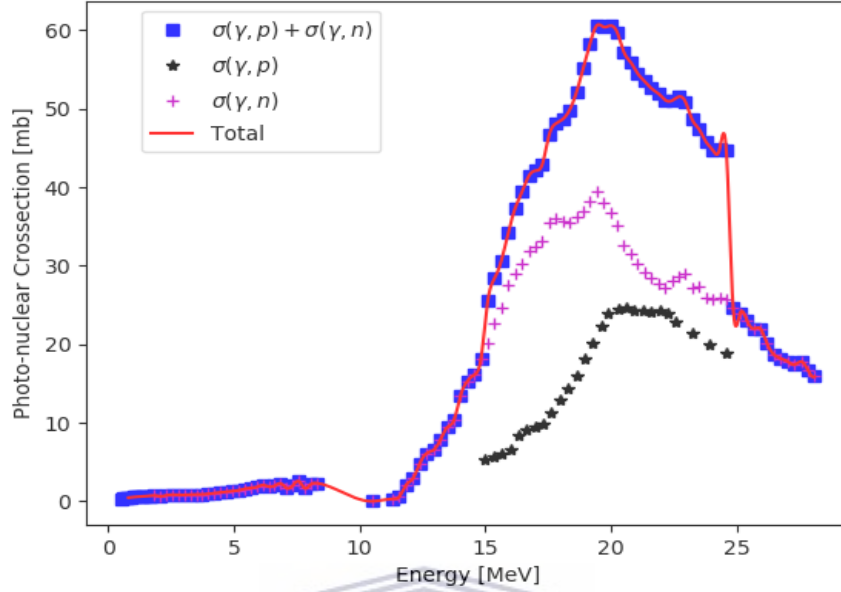


Figure 3.5: Photo-nuclear cross section data for ^{45}Sc including (γ, n) and (γ, p) reaction cross sections. The total cross section (red) line is the sum of these reaction channels. The sudden drop of the total cross section results from missing (γ, p) data at $E_\gamma \geq 25\text{MeV}$.

The interpolation method described above was applied in order to calculate the desired quantities α , σ_{-2} and the polarizability parameter, κ . This method assumes validity of the Brink-Axel hypothesis¹ allowing the combination of $\sigma_{LEE}(E_\gamma)$ and $\sigma_{GDR}(E_\gamma)$, which are measured from states in the quasi-continuum and the ground state, respectively, to calculate total photo-nuclear cross sections. This is done by integrating the interpolant (cubic-spline interpolation function), red solid line in Fig. 3.5, as described in Eqs. 3.2 and 3.3. The interpolant is a piecewise function of cubic polynomials generated between a pair of consecutive data points.

This study investigates the effects and implications of enhancement of $f(E_\gamma)$ at low energies. The overall results are presented in Table 3.2 and Table 3.4. The largest contribution, 10.9% , of $\sigma_{-2}(\text{LEE})$ to $\sigma_{-2}(\text{total})$ is observed for ^{45}Sc , whereas the $\sigma_{-2}(\text{LEE})$ contribution is found negligible for heavy nuclei with a minimum of 0.4% for ^{138}La . A stronger contribution to $\sigma_{-2}(\text{total})$ is expected if the LEE increases at energies approaching $E_\gamma = 0$, as suggested by recent measurements [86, 94]. In nearly-spherical nuclei in the $A \approx 50$ and 90 mass regions the LEE starts at $E_\gamma \approx 3 - 4$ MeV whereas for heavy nuclei the LEE

¹The Brink-Axel hypothesis implies that a GDR can be built on every state in a nucleus and maintains the same shape or parameters

starts on average at a lower $E_\gamma \approx 2$ MeV. Implications of these results will be discussed in the following chapter.

Setting up the low-energy cut off in the up-bend of $f(E_\gamma)$ is not obvious. Although the recent work supports an increasing trend of the LEE at energies below 1 MeV [86, 94], there is little evidence on how $f(E_\gamma)$ behaves approaching $E_\gamma = 0$. Hence, in order to calculate σ_{-2} (LEE), the low-energy cut off has arbitrarily been set at 800 keV for the nuclide considered in this work up to ^{139}La which, in turn, is the typical energy for strong $M1$ isovector transitions in nearly-spherical nuclei [39]. For ^{153}Sm , the low-energy cut off of 645 keV is determined from experiment [83]. Additionally, because of the instability of ^{153}Sm , ^{138}La and ^{50}V , there is no experimental GDR information and instead, data from ^{152}Sm , ^{139}La and ^{51}V have been used in the analysis, respectively, under the assumption that nearby isotopes have equal $f(E_\gamma)$ (see e.g. Refs. [45] and [107]). However, this assumption may not be adequate given the rapid shape transition from weakly deformed in ^{150}Sm to a well-deformed rotor in ^{154}Sm and the realization of shell closures in ^{139}La (N=82) and ^{51}V (N=28).

Nucleus	$E_{\gamma(\min)}$ (MeV)	$E_{\gamma(\max)}$ (MeV)	σ_{-2} (total) ($\mu\text{b}/\text{MeV}$)	σ_{-2} (LEE) ($\mu\text{b}/\text{MeV}$)	C	References
$^{45}_{21}\text{Sc}^*$	0.800	28.10	1840(130)	178	9.7%	[108, 109, 110]
$^{50}_{23}\text{V}$	0.800	27.77	1458(100)	42	2.9%	[111, 53]
$^{51}_{23}\text{V}$	0.800	27.77	1472(100)	49	3.3%	[111, 53]
$^{56}_{26}\text{Fe}^*$	0.800	40.00	2231(155)	141	6.3%	[112, 47]
$^{76}_{32}\text{Ge}$	0.800	26.50	3189(225)	86	2.7%	[113, 114]
$^{92}_{40}\text{Zr}$	0.800	27.8	3131(220)	32	1.1%	[115, 116, 117]
$^{95}_{42}\text{Mo}$	0.800	27.84	4743(330)	79	1.7%	[118, 119]
$^{138}_{57}\text{La}$	0.800	24.30	7983(560)	29	0.4%	[120, 121]
$^{139}_{57}\text{La}$	0.800	24.30	8015(560)	56	0.7%	[120, 121]
$^{153}_{62}\text{Sm}$	0.645	19.98	9999(700)	403	2.7%	[122, 83]

Table 3.2: Low-energy enhancement contribution to the (-2) moment of the total photo-absorption cross section, σ_{-2} , and to the nuclear polarizability parameter, κ . Data have been extracted from EXFOR [103] and ENDF [104]. An asterisk indicates that the calculation includes $\sigma(\gamma, p)$ and C is the percentage contribution of σ_{-2} (LEE) to σ_{-2} (total).

Experimentally, the LEE is observed down to energies ≈ 1.5 MeV for the isotopes considered (excluding ^{153}Sm) as observed in Figs. 3.6 and 3.7, where the LEE data are fitted with cubic polynomials due to the resulting minimal root-mean-square error (RMSE) and allows acceptable extrapolation to lower energies. Fourth order polynomials yield similar results, contrarily for higher order polynomials. The extrapolated data are represented by a dashed blue-line for ^{45}Sc and ^{95}Mo in Fig. 3.8, obtained from the LEE fitting function.

For heavy nuclei, the LEE is only found in ^{105}Cd [123], $^{138,139}\text{La}$ [121] and $^{151,153}\text{Sm}$ [32], where the LEE starts on average at $E_\gamma \approx 2$ MeV, as shown in Table 3.3. The reason for not being widely observed in heavy nuclei, which were studied using the same experimental method, could relate to the unprecedented

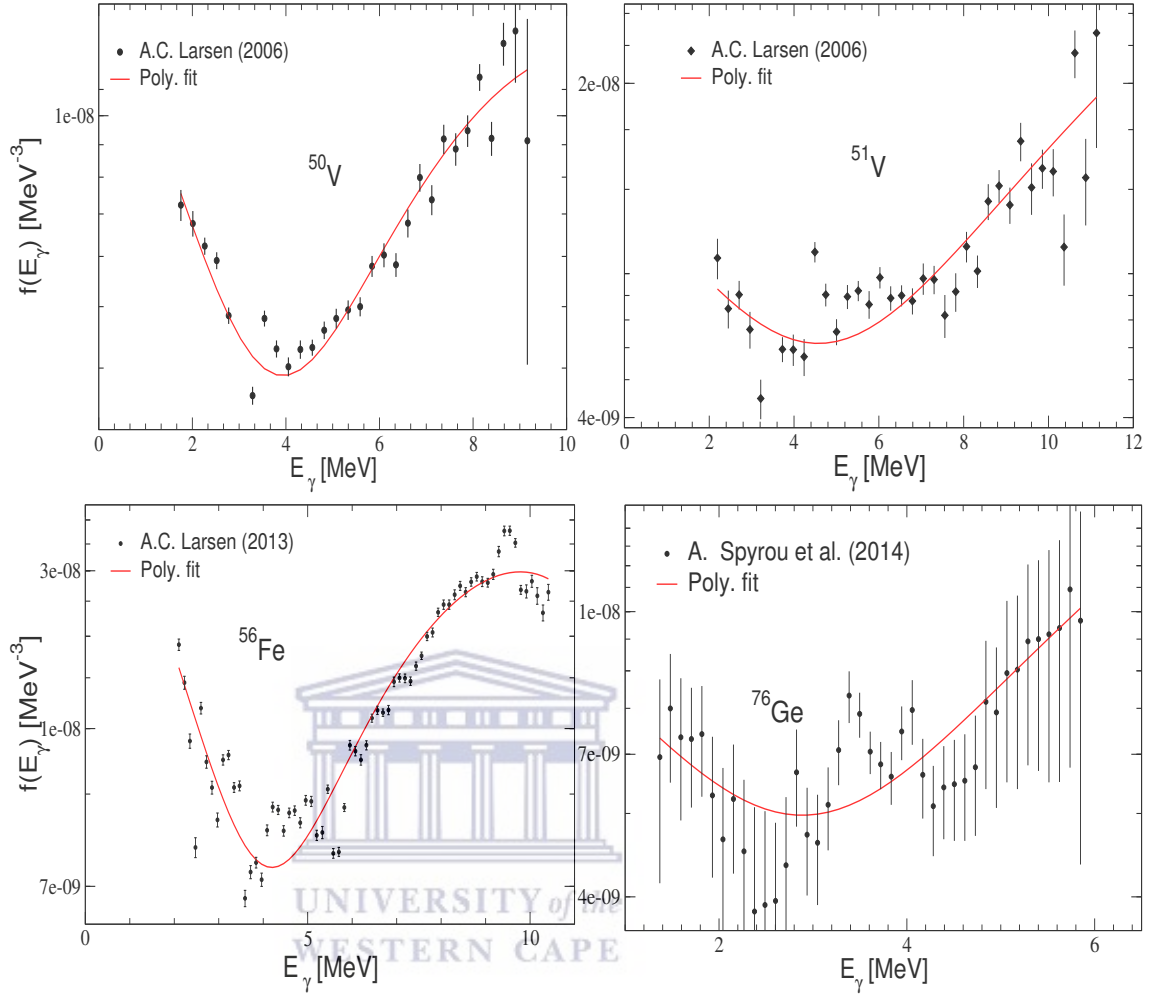


Figure 3.6: $f(E_\gamma)$ for ^{50}V , ^{51}V , ^{56}Fe and ^{76}Ge fitted with a cubic polynomial.

sensitivity achieved by Simon and co-workers in $^{151,153}\text{Sm}$ using high-purity germanium (HPGe) detectors in connection with Compton shields that allow detection of γ energies down to ≈ 500 keV [83].

The contribution of the LEE to the total cross section measuring the effect of the observed enhancement is calculated as follows,

$$C = \frac{\sigma_{-2}(\text{LEE})}{\sigma_{-2}(\text{total})}, \quad (3.9)$$

where $\sigma_{-2}(\text{LEE})$ is calculated between $E_{\gamma(\min)}$ and $E_{\gamma(e)}$, where $E_{\gamma(e)}$ being the approximate energy at which the enhancement of $f(E_\gamma)$ begins. Alternatively, $\sigma_{-2}(\text{without LEE})$ is calculated from $E_{\gamma(e)}$ to $E_{\gamma(\max)}$. Table 3.3 shows $E_{\gamma(e)}$ corresponding to the nuclei considered in this work. The quantity C , also measures the contribution of the LEE on the nuclear polarizability via the linear

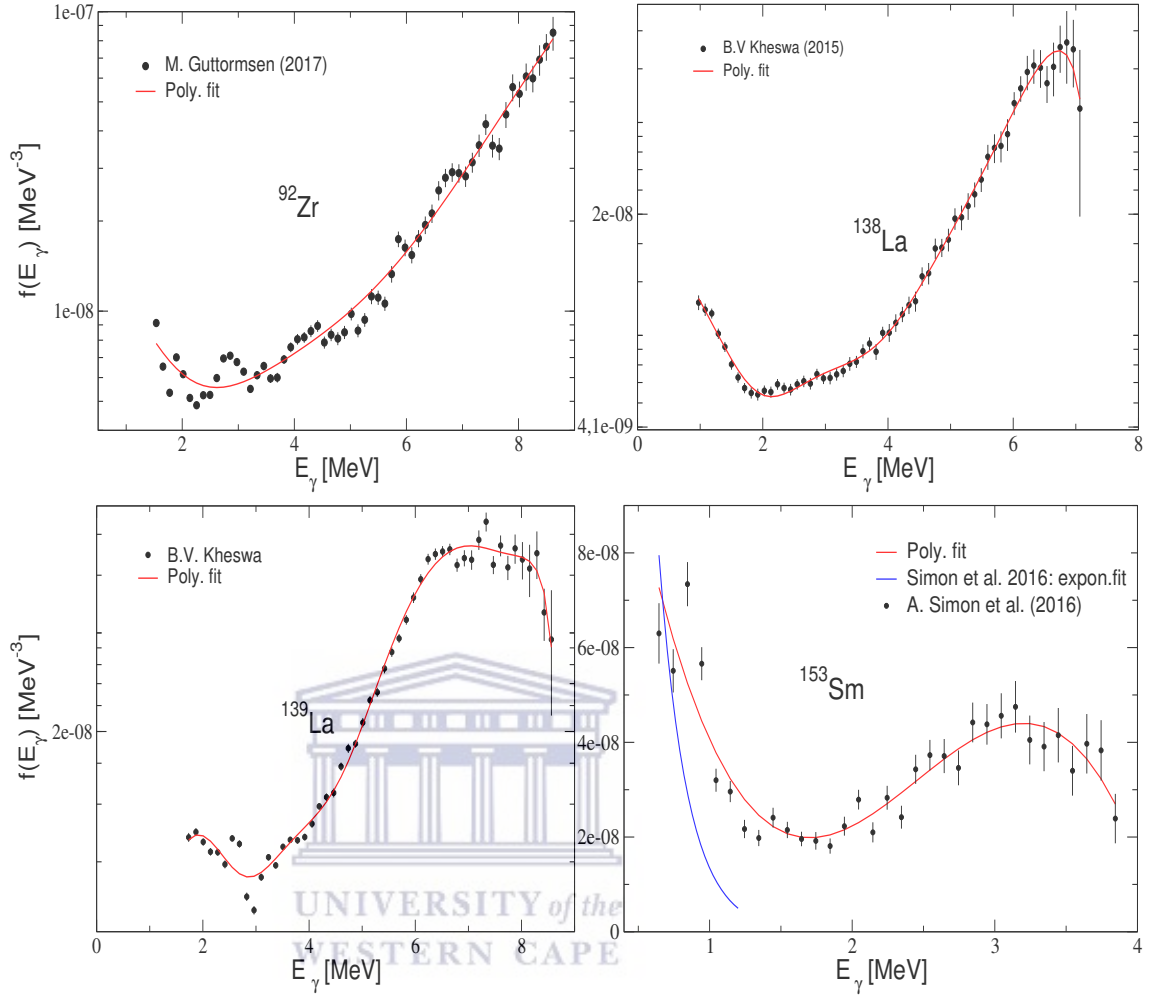


Figure 3.7: $f(E_\gamma)$ for ^{92}Zr and ^{135}Sm fitted with a cubic polynomial. The lanthanum isotopes, $^{138,139}\text{La}$, were fitted with a 4th order polynomials due to the large RMS when fitted with cubic polynomials.

relation of α and σ_{-2} in Eq. 3.3.

	^{45}Sc	^{50}V	^{51}V	^{56}Fe	^{76}Ge	^{92}Zr	^{95}Mo	^{138}La	^{139}La	^{153}Sm
$E_{\gamma(e)}$ [MeV]	3.2	3.1	3.1	3.8	2.3	2.2	2.5	1.9	2.5	1.6

Table 3.3: Approximate threshold energies of the enhancement of experimental $f(E_\gamma)$.

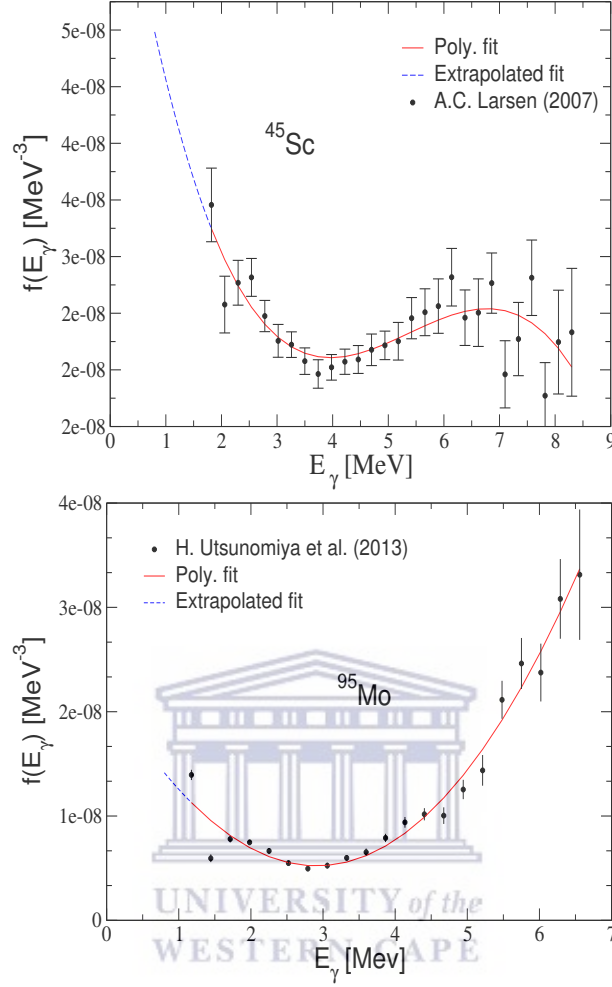


Figure 3.8: $f(E_\gamma)$ for ^{45}Sc fitted with a cubic polynomial, the dash blue line represents the extrapolated data region.

As the $\sigma_{-2}(\text{LEE})$ and $\sigma_{-2}(\text{GDR})$ values involve different measurements the errors reported in Table 3.2 were calculated in quadrature,

$$\Delta \sigma_{-2}(\text{total}) = \sqrt{\Delta \sigma_{-2}(\text{LEE})^2 + \Delta \sigma_{-2}(\text{GDR})^2}, \quad (3.10)$$

where $\Delta \sigma_{-2}(\text{LEE})$ and $\Delta \sigma_{-2}(\text{GDR})$ are calculated as the difference between the upper and lower bounds of σ_{-2} values, whose magnitudes are determined by the uncertainties in the experimental data. These errors are centered around 5% for $\sigma_{-2}(\text{GDR})$ values in most of the considered nuclei.

The polarizability parameters κ reported in Table 3.4 are calculated as follows,

$$\kappa = \frac{\sigma_{-2}}{2.38A^{5/3}}, \quad (3.11)$$

where κ measures the deviation of the GDR effects from hydrodynamic model predictions. A value of $\kappa = 1$ implies consistency of the hydrodynamic model predictions with experimental measurements, as shown in Fig. 1.3. This is the case for all considered nuclei, except ^{45}Sc and ^{56}Fe with $\kappa = 1.35$ and 1.13, respectively.

Nucleus	κ	κ
	(with LEE)	(without LEE)
$^{45}_{21}\text{Sc}^*$	1.35	1.17
$^{50}_{23}\text{V}$	0.89	0.85
$^{51}_{23}\text{V}$	0.87	0.85
$^{56}_{26}\text{Fe}^*$	1.13	1.07
$^{76}_{32}\text{Ge}$	0.97	0.96
$^{92}_{40}\text{Zr}$	0.70	0.69
$^{95}_{42}\text{Mo}$	1.00	0.99
$^{138}_{57}\text{La}$	0.90	0.90
$^{139}_{57}\text{La}$	0.90	0.89
$^{153}_{62}\text{Sm}$	0.95	0.90

Table 3.4: Low-energy enhancement contribution to the nuclear polarizability parameter, κ .

Further evaluation of our results can be done by comparison with the parameter-free σ_{-2} values from Ref. [27] which are described for $A \geq 3$ as follows,

$$\sigma_{-2}(A) = \frac{1.83A^2}{A^{1/3} - 1.27} \mu\text{b/MeV}, \quad (3.12)$$

resulting from introducing mass dependency of $a_{sym}(A)$ which was obtained from a global fit of binding energies of isobaric nuclei [127],

$$a_{sym}(A) = 28.32(1 - 1.27A^{-1/3}), \quad (3.13)$$

where $\frac{S_s}{S_v} \approx 1.27$ is the surface-to-volume ratio with $S_v \approx 28.32$ MeV the bulk symmetry energy coefficient. Consequently, this model accounts for Coulomb interaction energy and shell corrections. Figure 3.9 below shows κ values in Table 3.4 and calculated $\delta = \sigma_{-2}/\sigma_{-2}(A)$ values. These ratios (κ and δ) fairly agree for the heavy nuclei $^{138,139}\text{La}$ and ^{153}Sm , whereas there are evident deviations for the considered lighter nuclei particularly for ^{45}Sc , $^{50,51}\text{V}$, ^{56}Fe and ^{76}Ge . Furthermore, smaller ratios are noted for nuclei with or near neutron magic-numbers $N = 28$ and $N = 50$ suggesting the presence of shell effects. The M1 effects, not considered in the hydrodynamic model, could yield a more general and inclusive comparison of the results.

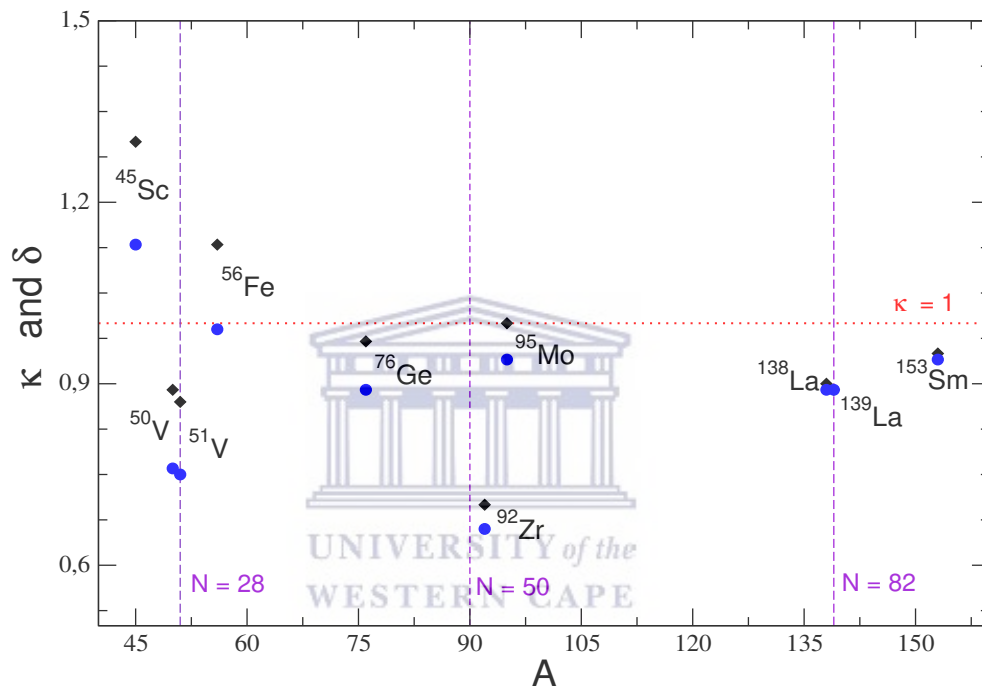


Figure 3.9: Comparison of the obtained results with the hydrodynamic model predictions with mass dependent symmetry $a_{sym}(A)$ and $a_{sym} = 23$ MeV. The blue circles represent δ values and black diamonds κ values, with a similar pattern.

Chapter 4

Discussion and Conclusion

4.1 Discussion

4.1.1 Photo-proton cross section

The impact of the missing $\sigma(\gamma, p)$ measurements on σ_{total} is significant, in particular for light mass nuclei. This is shown in Table 4.1 for even-even self-conjugate nuclei with isospin quantum number,

$$T_z = \frac{1}{2}(N - Z) = 0, \quad (4.1)$$

where $T_z = 0$ implies complete symmetry of protons and neutrons. Therefore assuming isospin symmetry, this allows testing of photo-neutron and photo-proton cross section contributions to σ_{total} , simultaneously evaluating isospin symmetry breaking. The ratio $\sigma(\gamma, p)/\sigma(\gamma, n)$ was calculated and presented in Table 4.1, rounded off to the nearest integer. It is observed that $\sigma(\gamma, p)/\sigma(\gamma, n) > 1$ in all the considered self-conjugate nuclei, which indicates dominance of the $\sigma(\gamma, p)$ channel and, hence, violates isospin symmetry. The magnitude of $\sigma(\gamma, p)/\sigma(\gamma, n)$ varies with the difference of nucleon between proton and neutron threshold energies, $|S_p - S_n|$. In general, the cross sections or $f(E_\gamma)$ are monotonically increasing functions of E_γ between S_p and S_n (e.g. see Fig. 3.5). This behavior emphasizes the significance of $\sigma(\gamma, p)$ cross section measurements omitted when $S_p \leq S_n$ [25]. Physically, in light mass nuclei the low S_p indicates loosely bound nuclear systems due to weak Coulomb interaction, also violating the isospin symmetry. Figure 4.1 shows that including $\sigma(\gamma, p)$ to the total cross section yields σ_{-2} values close to those predicted for $A \geq 3$ [27], similarly for α .

Furthermore, an evaluation of $S_p - S_n$ was done for magic and semi-magic nuclei with $N = 20, 28, 50$ and 82 . The S_p and S_n difference is observed to be increasing with decreasing mass number, A , as shown in Fig. 4.2. This emphasizes the importance of $\sigma(\gamma, p)$ contributions, particularly for light nuclei. However, the N_p/N_n ratio determines σ_{total} and σ_{-2} values. Additionally, below particle threshold energies, soft resonances and the LEE also contribute to the σ_{total} and σ_{-2} values.

Nucleus	S_p (MeV)	S_n (MeV)	$\sigma_{-2}(\gamma,p)$ (mb/MeV)	$\sigma_{-2}(\gamma,n)$ (mb/MeV)	$\sigma_{-2}(\text{total})$ (mb/MeV)	$\frac{\sigma(\gamma,p)}{\sigma(\gamma,n)}$
^{12}C	15.95	18.72	0.253	0.073	0.326	4
^{16}O	12.13	15.66	0.254	0.098	0.352	3
^{20}Ne	12.84	16.86	0.252	0.090	0.342	3
^{24}Mg	11.69	16.53	0.397	0.109	0.506	4
^{28}Si	11.58	17.17	0.559	0.200	0.759	3
^{32}S	8.86	15.05	1.219	0.190	1.409	6
^{40}Ca	8.33	15.64	1.239	0.210	1.449	6

Table 4.1: Ratios of proton to neutron emission reaction cross sections, particle threshold energies, experimental (γ, p) and (γ, n) cross sections. The cross sections were calculated using the interpolation method in this work.

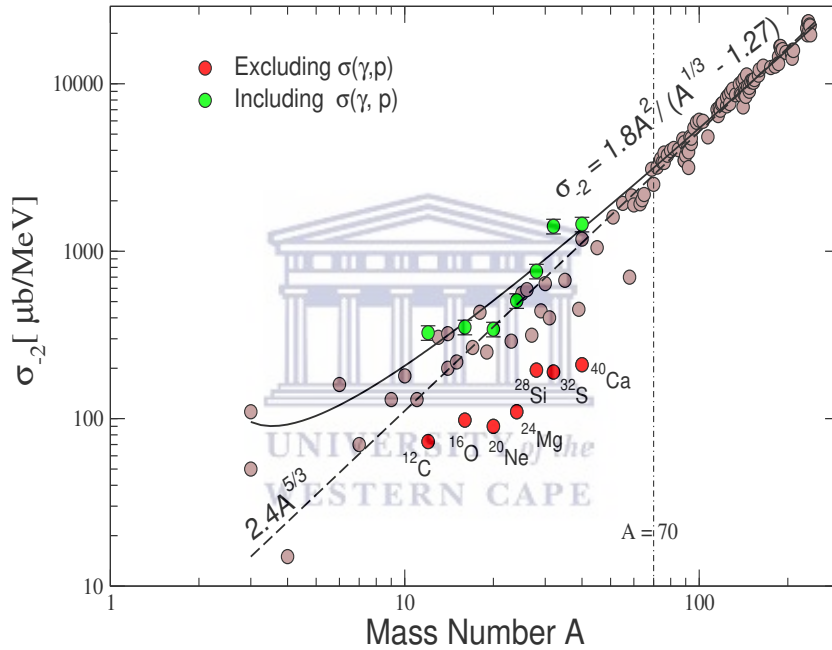


Figure 4.1: Second moment of photo-nuclear cross sections of self-conjugate nuclei, with and without the $\sigma(\gamma, p)$ cross sections, emphasizing the significance of photo-proton cross sections.

4.1.2 LEE and shell effects

More intriguing are the small overall contributions to σ_{-2} (with and without LEE) values found in nuclei close to or having a magic number. When compared with Eq. 1.6 and 3.12, these nuclides present evident deviations from GDR effects (i.e. $\delta, \kappa \neq 1$) with smaller values of $\kappa \approx 0.90$ in $^{50,51}\text{V}$ ($N \approx 28$) and $^{138,139}\text{La}$ ($N \approx 82$), and specially for ^{92}Zr ($N \approx 50$ and $Z = 40$) with $\kappa = 0.70(3)$. In contrast, heavy nuclei away from shell closures present polarizability parameters consistent with $\kappa = 1$; except perhaps for ^{153}Sm , where one used the ^{152}Sm data for the GDR region and a cut-off of $E_\gamma = 645$ keV.

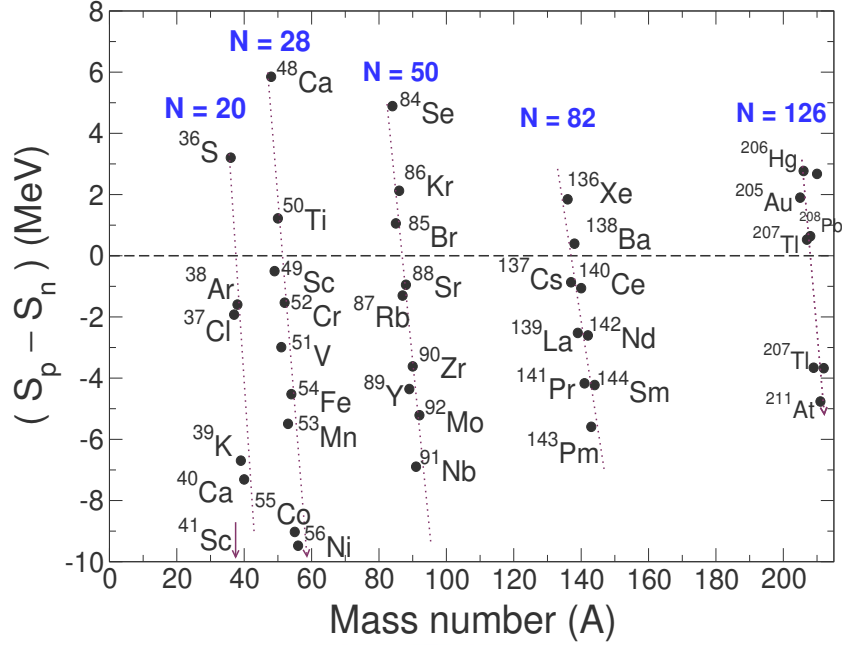


Figure 4.2: Nucleon threshold energy differences for magic and semi-magic nuclei (black circles) for $N = 20, 28, 50, 82$ and 126 isotones. A significant fraction of these nuclei have low S_p energies compared to S_n in concordance with closed shells properties

This recurrent behavior to the one previously observed in the photo-neutron cross-section data for the $N = 50, 82$ and 126 isotones, indicates the continuing influence of shell effects in the quasi-continuum region up to the neutron threshold. As shown in Table 3.2 and inset (d) in Fig. 4.3, this is consistent with the smaller LEE contribution to the total σ_{-2} values of $^{50,51}\text{V}$ ($N \approx 28$) with respect to the neighboring ^{45}Sc and ^{56}Fe nuclide. Although there is no $\sigma(\gamma, p)$ data available for $^{50,51}\text{V}$, (γ, p) contributions will relatively be much weaker for ^{51}V because of the much lower level density of the open proton channel (even-even ^{50}Ti with $N = 28$) as compared with the open neutron channel (odd-odd ^{50}V).

The values listed in Table 3.2 are presented in Fig. 4.3, including overall σ_{-2} values of ground states as a function of A extracted from photo-neutron cross sections using mono-energetic photon beams and determined above neutron threshold to an upper limit of $E_{\gamma_{max}} \approx 20 - 50$ MeV [25]. The data include the GDR region and are representative for nuclei above $A \gtrsim 50$ (except for ^{58}Ni [58], where neutron emission is generally the predominant decay mode.). This may not be true for semi-magic number nuclei ($N = 20, 28, 50, 82$ and 126) where proton separation energies predominantly lie at much lower energies than neutron thresholds, as illustrated in Fig 4.2.

Sudden drops of σ_{-2} (and κ) values are evident for the $N = 50, 82$ and 126

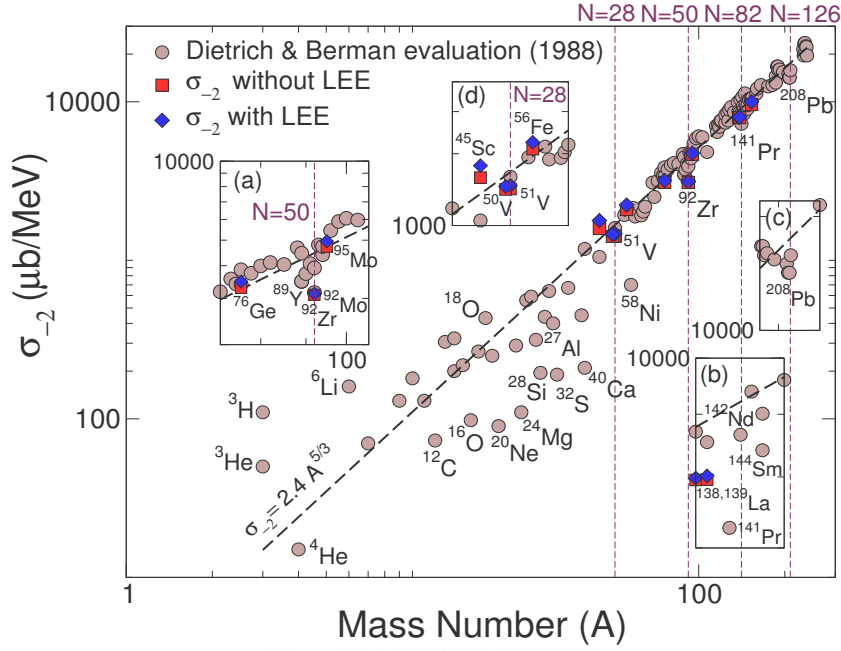


Figure 4.3: σ_{-2} vs A on a log-log scale from the photo-neutron cross-section evaluation [25] and σ_{-2} data listed in Table 3.2 excluding (squares) and including (diamonds) the LEE contributions. For comparison, Eq. 1.6 (dashed line) is plotted.

isotones in the insets (a), (b) and (c) of Fig. 4.3, respectively. The σ_{-2} values are directly affected by $E_{\gamma(\min)}$ and $\sigma(\gamma, p)$, as observed for ^{45}Sc in Fig. 3.5 including $\sigma(\gamma, p)$ increases $S_{GDR}^{g.s.}$ by approximately 1.5 orders of magnitudes. Above both proton and neutron separation energies, the photo-absorption cross section in the lower energy part of the GDR is controlled by the statistical competition between $\sigma(\gamma, p)$ and $\sigma(\gamma, n)$ contributions, which presents a strong correlation with the level density ratio N_p/N_n between the open neutron and proton channels [110],

$$\sigma(\gamma, p)/\sigma(\gamma, n) \approx N_p/N_n . \quad (4.2)$$

This ratio also depends on the neutron and proton penetrabilities, K_n and K_p , respectively, which are the kinetic energies of the escaping nucleons. The preceding dependence is shown in §2.4 where E_1 and E_2 determine the energies at which level densities N_p and N_n are measured, respectively.

The photo-absorption cross-sections $\sigma(\gamma, n) + \sigma(\gamma, p)$ are reasonably available in the $N = 50$ isotones, with the latter being indirectly determined from $(e, e'p)$ measurements [110]. The $\sigma(\gamma, p)$ contribution is particularly important for ^{92}Mo , with $N_p/N_n \approx 1.95$, and decreases for the lighter $N = 50$ isotones, with $N_p/N_n \approx 0.66, < 0.28$ and 0.09 for ^{90}Zr , ^{89}Y and ^{88}Sr , respectively [118], as the isospin quantum number T_z increases signifying distinct behavior of protons and neutrons. The $\sigma(\gamma, p)$ contribution extracted from the N_p/N_n ratio

only applies to the lower energy half of the GDR, and $\sigma(\gamma, n)$ contributions still remain greater. Once $\sigma(\gamma, p)$ contributions are taken into account, the total photo-absorption cross section satisfies the TRK sum rule [118],

$$\frac{\sigma(\gamma, n) + \sigma(\gamma, p)}{0.06NZ A^{-1}}. \quad (4.3)$$

For the ^{92}Mo case, there remains $\approx 35\%$ $\sigma(\gamma, p)$ contribution to the total photo-absorption cross section [110], which explains the sharper drop in the σ_{-2} value shown in Fig. 4.3(a). More conspicuous are the drops of σ_{-2} values in ^{89}Y , ^{141}Pr and ^{208}Pb – where $\sigma(\gamma, n)$ contributions strongly dominate – which could provide evidence for shell effects. Clearly, direct measurements of $\sigma(\gamma, p)$ contributions are crucially needed for singly- and doubly-magic nuclei.

4.1.3 Paramagnetism in the quasi-continuum

Table 3.2 shows that the LEE has a substantial contribution to σ_{-2} values in medium-mass nuclei (^{45}Sc and ^{56}Fe) away from the $N = 28$ shell closure, being largest for ^{45}Sc with $\approx 11\%$ increase. Coincidentally, enhanced paramagnetism is expected and also observed for nuclei in the $A \approx 50$ mass region [71, 72] occupying the $1f_{7/2}$ and $2p_{3/2}$ shells, which is the case for ^{45}Sc and ^{56}Fe . In fact, according to the IPM, enhanced paramagnetism is expected for nuclei populating shells with high multiplicities. These support the prominent M1 character of the LEE already predicted from SM calculations for ^{45}Sc [95] and assigned with a dipole character from angular distribution measurements for ^{56}Fe [86], which can be described as induced permanent magnetic dipole moments or paramagnetism in the quasi-continuum.

As illustrated in Fig. 4.4, comparing ^{45}Sc and ^{153}Sm , this enhancement partly arises because of the inverse mass dependence of E_{GDR} and the fact that the LEE starts at lower E_γ as A increases (see Table 3.3). In fact, Table 3.2 shows that the LEE has a negligible contribution of $\lesssim 3\%$ to the total σ_{-2} values of heavy nuclei with $A \geq 76$. Following the preceding deductions: the LEE for light nuclei may be more pronounced and dominated by the magnetic dipole component, supported by SM calculations [94] and χ_p measurements [72].

4.2 Conclusion

Drops of σ_{-2} values ($\kappa < 1$) for several nuclei with, or close to, neutron magic numbers $N = 28, 50, 82$ and 126 , suggest that the SM remains valid at high excitation energies, from the quasi-continuum to the GDR region; in agreement with Balashov's SM interpretation of the GDR as a system of independent nucleons plus the residual interaction [124]. The deviations from GDR effects, are plausibly not related to $E1$ transitions because of the nature of Eq. 1.6. These together with the continuing influence of shell effects, strongly support the M1 interpretation of the LEE by large-scale SM calculations [88, 93, 94, 95, 96]. Moreover, The empirical evidence for shell effects (with and without LEE) suggests that the generalized Brink-Axel hypothesis allows for structural changes

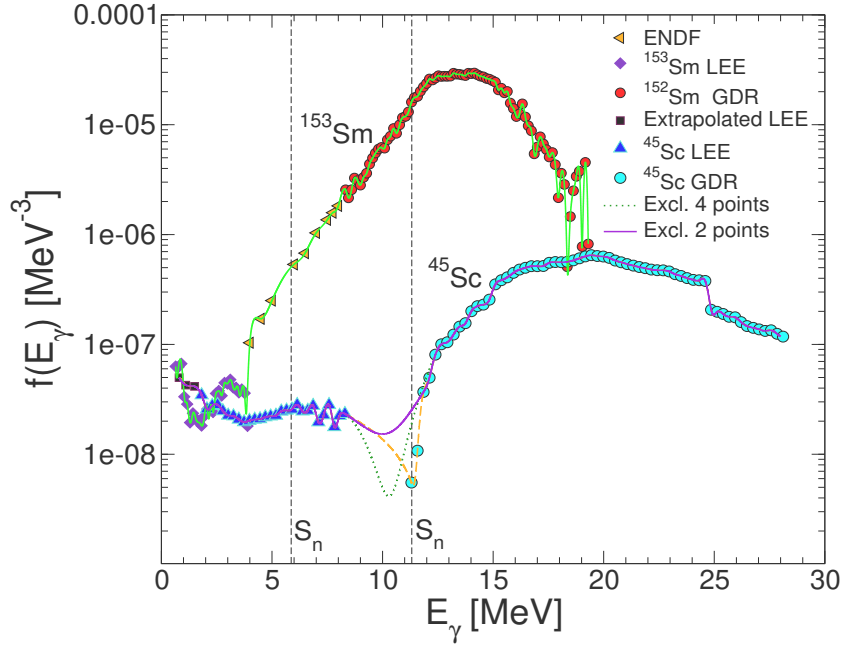


Figure 4.4: $f(E_\gamma)$ vs E_γ on a log scale showing the interpolation to the data (solid line) for ^{45}Sc and ^{153}Sm .

and is, therefore, more universal than originally expected. Following from conservation of the GDR parameters measured in the ground and excited states. This conclusion is also supported by the work of Larsen and collaborators [85], where the general $f(E_\gamma)$ trends are found to be preserved for different bin energies.

Finally, the induction of permanent magnetic dipole moments or paramagnetism in the quasi-continuum region is confirmed, due to the predominant $M1$ character of the LEE and sensitivity to low- E_γ . This is in agreement with previous SM calculations and IPM predictions of an enhanced paramagnetism for the ground states of nuclei with large occupation number of the shells [71]. Determining the magnetic properties that also govern the $M1$ operator. The origin of this paramagnetism can be inferred from SM calculations, which can distinguish between single-particle spin-flips and collective isovector excitations by decomposing the relevant $M1$ strength into their spin and orbital components [39]. It is evident from this work that σ_{-2} values are extremely sensitive measures of the long-range correlations in the nuclear wave functions. This work, therefore, opens new research avenues to investigate the existence and evolution of shell closures at high-excitation energies from σ_{-2} measurements and emphasizes the importance of $\sigma(\gamma, p)$ measurements, particularly for medium and light mass nuclei.

Appendix A

A.1 Nuclear Symmetry Energy

Herein we discuss the properties of symmetry energy in nuclear systems. Symmetry energy also appears in astrophysics, playing an essential role in understanding astrophysical processes like supernovae [125, 126]. In a nuclear system, the symmetry, $a_{sym}(A)$, energy measures the variation of binding energy as the neutron to proton difference (N-Z) changes, alternatively the ratio (N:Z) [125]. This means $a_{sym}(A)$ results from asymmetry $(N - Z)/A$ of having excess neutrons or protons.

The symmetry energy is one of the parameters that are prominent and drive the GDR, acting as a restoring force [2]. In the hydrodynamic model treatment it is assumed that the energy density $a_{sym}(A)(\rho_n - \rho_p)^2/\rho$ is distributed uniformly throughout the nucleus. Therefore, $a_{sym}(A)$ certainly does affect the GDR, also vital in determination of the equation of state [125, 126].

The mass dependence of $a_{sym}(A)$ was long established and recent developments show that [127],

$$a_{sym}(A) = S_v \left(1 - \frac{S_s}{S_v A^{1/3}} \right) \text{MeV}, \quad (\text{A.1})$$

where $S_v \approx 28.32$ MeV is the bulk symmetry energy coefficient and $\frac{S_s}{S_v} \approx 1.27$ the surface to volume ratio. The preceding definition of $a_{sym}(A)$ was obtained from a global fit to the binding energies of isobaric nuclei with $A \geq 10$, [127, 128]. The mass dependency allows us to explore it using various methods such as GDRs, photo-absorption cross sections and binding energies. A complete manuscript evaluating $a_{sym}(A)$ using the aforementioned methods is yet to be published.

Herein we focus on interpretations of $a_{sym}(A)$ using GDR parameters and photo-absorption cross sections. These interpretations relate $a_{sym}(A)$ with the parameter of interest i.e. nuclear polarizability, discussed in §2.2.3. In terms of the photo-absorption cross-section the symmetry energy is [18],

$$a_{sym}(A) = \frac{e^2 R^2 \pi^2}{20 \hbar c} \frac{A}{\sigma_{-2}} \simeq 5.2 \cdot 10^{-3} \frac{A^{5/3}}{\sigma_{-2}} \text{MeV}. \quad (\text{A.2})$$

Eq. A.2 above also known as the Migdal sum rule shows the direct relation between $a_{sym}(A)$ and the nuclear polarizability via σ_{-2} . Also explaining the observed large polarizability of light nuclei.

In a hydrodynamic model modified by B. Berman and S. Fultz [129], the dipole resonance was shown to have symmetry energy dependence as follows,

$$E_{GDR} \simeq \frac{\hbar R}{2.08A} \left[\frac{a_{sym} 8NZ}{m} \left(1 - \left(\frac{\Gamma_R}{2E_{GDR}} \right)^2 \right) \right]^{1/2}, \quad (\text{A.3})$$

and deduced that for a nucleus with a well defined radius R it follows that,

$$a_{sym}(A) = 9.93 \times 10^{-4} \left(\frac{A^{8/3}}{NZ} \right) \frac{E_{GDR}^2}{1 - \left(\frac{\Gamma_R}{2E_{GDR}} \right)^2}. \quad (\text{A.4})$$

To an acceptable agreement the preceding expressions reproduce the saturation property of symmetry energy, around 23 MeV implying insensitivity to the N/Z ratio, as shown in Figs. A.1 and A.2. The observed general decrease of $a_{sym}(A)$ for light nuclei explains the enhanced polarizability of loosely-bound light nuclei.

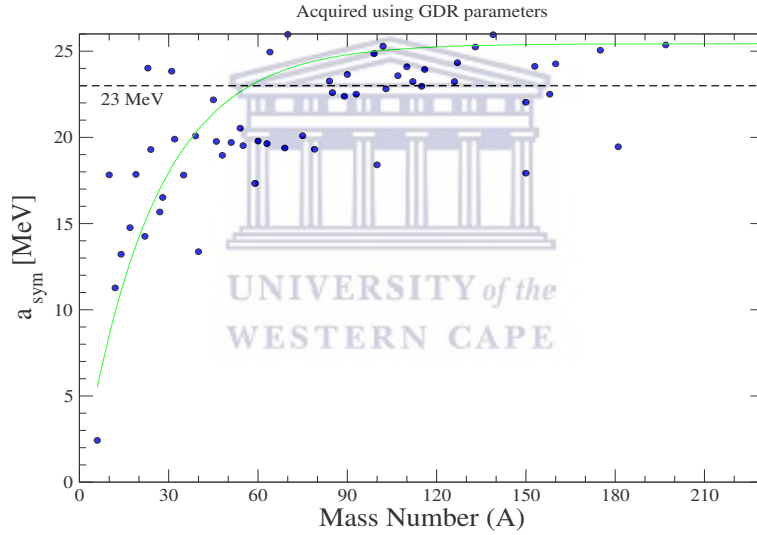


Figure A.1: Symmetry energy extracted from GDR parameters (blue circles), the color line is the fit using Eq. A.4.

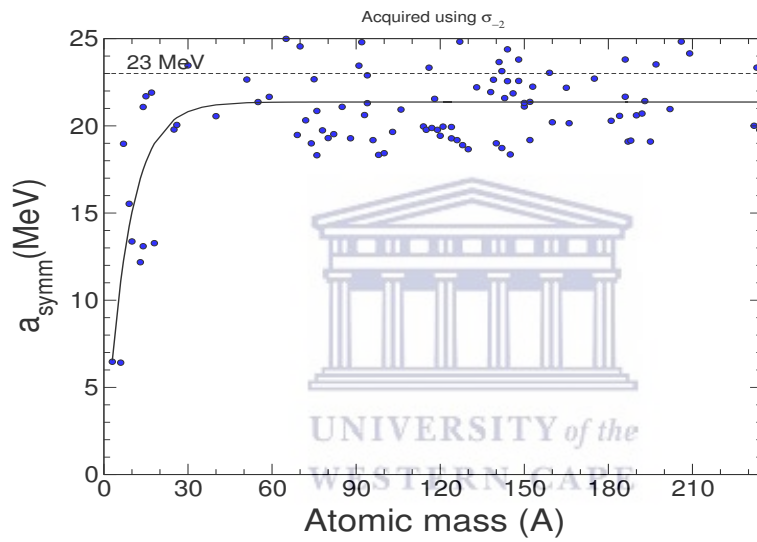


Figure A.2: Symmetry energy extracted from σ_{-2} (blue circles), fitted using Eq. A.2.

Appendix B

B.1 Interpolation Code

A code written in Python, that calculates the required cross sections and their respective moments i.e. σ_{total} , σ_{-2} & σ_{-1} is presented below. Values assigned to parameters in the code below are those of ^{138}La and can be easily changed according to the desired output.

The energies and cross sections data are loaded in arrays whose lengths are dependent on the region of interest and experimental limitations. A one dimensional cubic interpolation function was defined, one dimensional implying there is one independent variable, E_γ in this case. Data reproduced by the interpolating function is stored in a file named *output_data_138La.dat*. One can execute this code in terminal or Python GUI by navigating to the directory with the .py file and use the command: *python filename.py*. The integration limits can be controlled in the *xint* array. The main purpose of this program is to calculate total photonuclear cross sections and their moments, using cubic-spline interpolation, where the interpolant is a piecewise function of cubic polynomials generated between a pair of consecutive data points. This was done using a numerical integration method. Minimizing the increments of energy, h in Eq. B.1, to order 10^{-3} MeV reduces the error (systematic) of integration to negligible values, the error is determined from the cross section values yielded by the interpolation function. The output can be represented in graphs see Fig. B.1.

The error $d\sigma$ of the CTR can be obtained as a difference between the numerical result of the integral and the CTR integral value.

$$d\sigma = \int_{E_\gamma(\min)}^{E_\gamma(\max)} \sigma(E_\gamma) dE_\gamma - h \left[\frac{\sigma(E_\gamma(\min)) + \sigma(E_\gamma(\max))}{2} + \sum_{k=1}^{N-1} \sigma(E_\gamma(\min) + kh) \right] \quad (\text{B.1})$$

where the cross section $\sigma(E_\gamma)$ values are generated by the interpolant, h is the energy increment and N is the number of trapezoids.

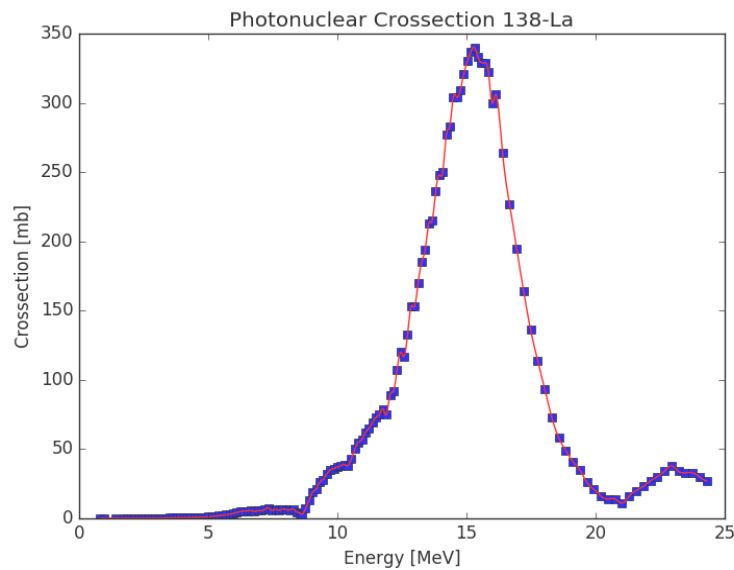


Figure B.1: Photonuclear cross section of ^{138}La showing the interpolation function $f(E_\gamma)$, red solid line.

```
### Libraries
```

```
from numpy import arange
from scipy.interpolate import interp1d
import numpy as np
import matplotlib.pyplot as plt
from scipy.integrate import trapz
import numpy
import math
```

```
### DATA INPUT
```

```
x = np.array([]) #Energy [MeV]
y = np.array([]) #Cross-section [mb]
```

```
### INTERPOLATION & INTEGRATION
```

```
f = interp1d(x,y,kind = 'cubic') # Cubic spline, Interpolating function
```

```
xint = np.arange(0.800,27.84,0.001) # Energy array
yint = f(xint) # Cross sections by the Interpolating func.
yint2 = f(xint)/(xint**2) # E1(-2)sigma data
f_X1 = (1/((1)*(math.pi**2)*(197.326)**2))*(yint/10*xint) ## photon strength function
```

```
with open("output_data_138La.dat", "w") as out_file: # Saving data into a file: Cross section
    for i in range(len(xint)):
```

```

        output_string = ""
        output_string += str(xint[i])
        output_string += " " + str(yint[i])      # storing data in column format
        output_string += "\n"                  # new line
        out_file.write(output_string)
        #print output_string                    # Printing Interpolation data(optional)

with open("gsf_output_data_138La.dat", "w") as out_file: ## Gamma-Strength functions file
    for i in range(len(xint)):
        output_string = ""
        output_string += str(xint[i])
        output_string += " " + str(f_X1[i])
    output_string += "\n"
    out_file.write(output_string)
    #print output_string                        ## Printing Interpolation data

## NUMERICAL INTEGRATION

h = 0.001
summ = 0

for i in range(0,len(xint)):
    summ = summ + yint2[i]

summ2 = (yint2[0] + yint2[len(xint)-1])*0.5
numeric_int = h*(summ2+summ)

## COMPOSITE TRAPEZOIDAL RULE INTEGRATION

sigma_total = numpy.trapz(yint,x,axis = 0)      # Total crossection integral
sigma_(-2) = numpy.trapz(yint2,xint,axis = 0)  # E1(-2)sigma integral

## REPORT

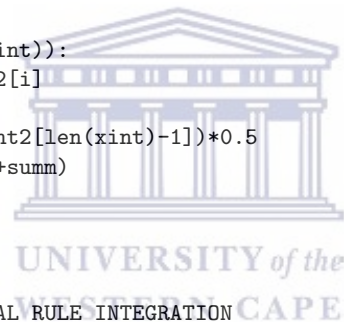
print "REPORTING INTEGRALS"
print "Raw_Total_sig(g,*): ", sigma_total , "mb-MeV"      # The Integral
print "(-2)_sig(g,*): ", sigma_(-2) , "mb/MeV"          # (-2)sigma_value
print "error :",abs(b-numeric_int)                        # Error

### PLOTS FOR VISUALISATION

plt.plot(x,y,'s',c='b')
plt.plot(xint,yint,'-',c='r')
plt.xlabel('Energy [MeV]')
plt.ylabel('Crossection [mb]')
plt.title('Photonuclear Crossection')

plt.show()                                              # Displaying a graph

```



B.2 Saclay annihilation photon method

The simplest experimental set up of the Saclay electron linear accelerator (linac) is shown in Fig. B.2.

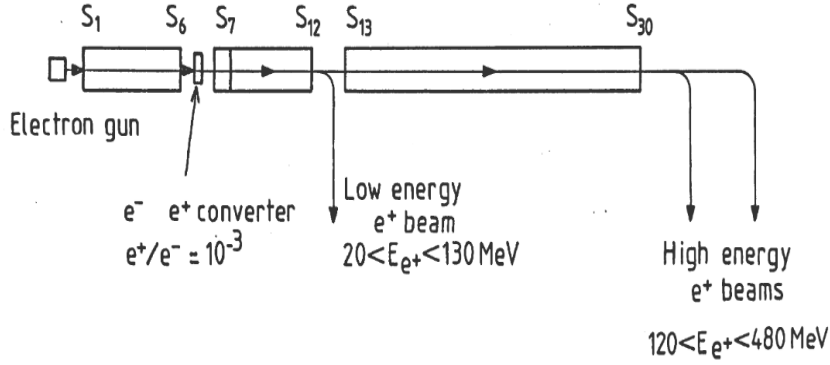


Figure B.2: Schematic of the Saclay linac, accelerating positrons [132] at desired energies towards a low-Z target.

At the converter, S₆, in Fig. B.2 an electron beam with energy around 85 MeV hits a converter, e.g. a 3mm thick gold (Au) target, and positrons are produced by pair production. These positrons (e⁺) are accelerated and simultaneously trapped in a strong magnetic field to reduce spacial cross section of the positron beam, then deflected to the experimental areas using bending magnets. The positrons then bombard a low Z target, e.g. ⁹Be, thus producing photons that initiate a nuclear reaction.

An improved method of the in-flight annihilation of positrons was developed. The peculiarity of this method is annihilation-tagging by a photon. The Saclay 720 MeV linear accelerator facility delivered 130-150 MeV tagged photons, see Fig. B.3. The electron-positron annihilation process dominantly produces two photons that scatter at different angles θ_1 and θ_2 , named hard- γ and soft- γ respectively, Fig. B.4 illustrates this process.

The hard- γ induces the photo-nuclear reaction under study, photon energies measured in the lab reference frame are related to the emission angles θ_i (for $i = 1, 2$) by [132],

$$E_{\gamma i} = \frac{(E_+ + m_e)m_e}{E_+ + m_e - P_+ \cos \theta_i}, \quad (\text{B.2})$$

where E_+ , P_+ are energy and momentum of the incident positron.

At large angles i.e. $\theta_2 \approx 90^\circ$ the variation in the energy of the soft- γ 's is slower thus favoring accurate measurements of the hard- γ energies. This process is in coincidence with the bremsstrahlung radiation, affecting the statistics

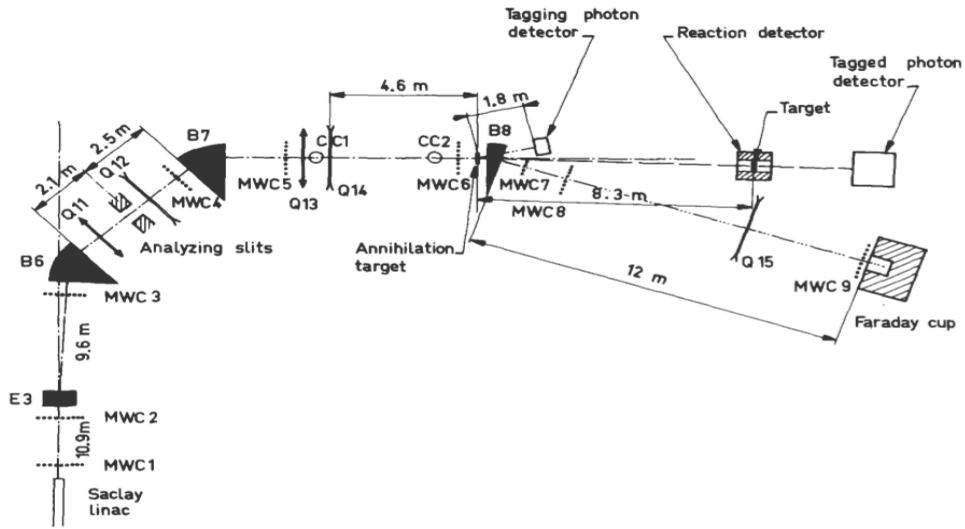


Figure B.3: Schematic view of the Saclay experimental set up, showing positron and photon beam transport elements [131].

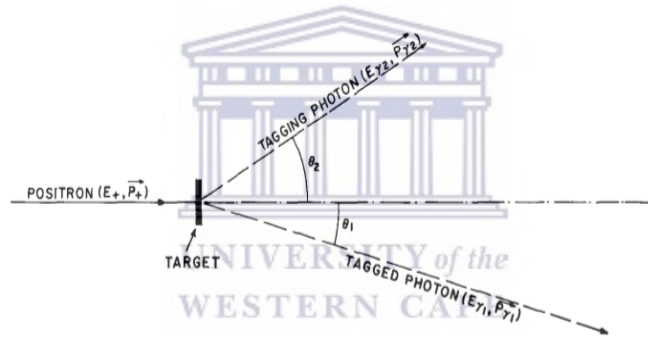


Figure B.4: The annihilation process shown in lab reference frame [131].

of useful events measured and optimal photon rate. To counteract or reduce the bremsstrahlung radiation a low- Z target is used since the bremsstrahlung radiation energy is proportional to Z^2 as shown in the preceding chapter. A flux of incident positron that did not annihilate, pass through the low- Z target and are stopped using a Faraday cup and scintillator detectors were used to measure γ -energies. Further details of the Saclay Lab experimental set-up and data acquisition systems can be found in reference [132]. However, major developments have taken place since the era of the experimental set up described above [133]. The annihilation photon method is preferred due to its ability to produce monoenergetic photons allowing simultaneous measurements of the partial photon-neutron cross sections which are in competition in the GDR region yielding σ_{total} .

Bibliography

- [1] <https://sites.google.com/site/fysikkenhm/det-periodiske-system/radioaktivitet/saadab-navigererer-du-paa-isotopkortet>
- [2] A. B. Migdal, J. Phys. USSR **8**, 331 (1944).
- [3] H. Steinwedel, J. H. Jensen, and D. Jensen, Phys. Rev. **79**, 1019 (1950).
- [4] M. Goldhaber and E. Teller, Phys. Rev. **74**, 1046 (1948).
- [5] G. C. Baldwin and G. S. Klaiber, Phys. Rev. **71**, 3 (1947).
- [6] A. B. Migdal, J. Exptl. Theoret. Phys. U.S.S.R. **15**, 81 (1945).
- [7] K. Hebeler and A. Schwenk, Eur. Phys. J. A **50**, 11 (2014).
- [8] M. Centelles, X. Roca-Maza, X. Viñas, and M. Warda, Phys. Rev. Lett. **102**, 122502 (2009).
- [9] J. Piekarewicz *et al.*, Phys. Rev. C **85**, 041302(R) (2012).
- [10] A. W. Steiner, M. Prakash, J. M. Lattimer and P. J. Ellis, Phys. Rep. **411**, 325 (2005).
- [11] C. Bertulani and J. Piekarewicz, (Eds.) *Neutron Star Crust*, Nova Science Publishers (2012).
- [12] J. M. Lattimer, Nucl. Phys. A **928**, 276 (2014).
- [13] J. M. Lattimer, and M. Prakash, Phys. Rep. **333-334**, 121 (2000).
- [14] J. M. Pearson, N. Chamel, A. F. Fantina and S. Goriely, Eur. Phys. J. A **50**, 43 (2014).
- [15] C. F. von Weizsäcker, Z. Phys. **96**, 431 (1935).
- [16] H. A. Bethe and R. F. Bacher, Rev. Mod. Phys. **8**, 82 (1936).
- [17] J. S. Levinger, *Nuclear Photo-Disintegration* (Oxford University Press, Oxford, 1960).
- [18] A. B. Migdal, A. A. Lushnikov and D. F. Zaretsky, Nucl. Phys. A **66**, 193 (1965).
- [19] O. Bohigas, N. van Giai and D. Vautherin, Phys. Lett. B **102**, 105 (1981).

- [20] Z. Zhang, Y. Lim, J. W. Holt, C. M. Ko, Phys. Lett. B **777**, 73 (2018).
- [21] D. Gambacurta, M. Grasso, O. Vasseur, Phys. Lett. B **777**, 163 (2018).
- [22] J. Piekarewicz et al., Phys. Rev. C **85**, 041302 (2012).
- [23] X. Roca-Maza et al., Phys. Rev. C **88**, 024316 (2013).
- [24] X. Roca-Maza et al., Phys. Rev. C **92**, 064304 (2015).
- [25] S. S. Dietrich and B. L. Berman, Atom. Data Nucl. Data Tables **38**, 199 (1988).
- [26] J. S. Levinger, Phys. Rev. **107**, 554 (1957).
- [27] J. N. Orce, Phys. Rev. C **91**, 064602 (2015).
- [28] O. Häusser *et al.*, Nucl. Phys. A **212**, 613 (1973).
- [29] W. J. Vermeer *et al.*, Aust. J. Phys. **35**, 283 (1982).
- [30] F. C. Barker, Aust. J. Phys. **35**, 291 (1982).
- [31] W. J. Vermeer *et al.*, Phys. Lett. B **122**, 23 (1983).
- [32] M. K. Raju *et al.*, Phys. Lett. B **777**, 250 (2018).
- [33] P. von Neumann-Cosel, Phys. Rev. C **93**, 049801 (2016).
- [34] N. Paar, D. Vretenar, E. Khan, and G. Colo, Rep. Prog. Phys. **70**, 691 (2007).
- [35] J. Birkhan et al., Phys. Rev. Lett. **118**, 252501 (2017).
- [36] L. W. Jones and K. M. Terwilliger, Phys. Rev. **91**, 699 (1953).
- [37] D. W. Kerst and G. A. Price, Phys. Rev. **79**, 725 (1950).
- [38] J. Ahrens, H. Gimm, A. Zieger and B. Ziegler, Il Nuovo Cimento A, Vol. **32**, N. 3, 364 (1976).
- [39] J. N. Orce *et al.*, Phys. Rev. Lett. **97**, 062504 (2006).
- [40] S. K. Bogner, R. J. Furnstahl, and A. Schwenk, Prog. in Part. Nucl. Phys. **65**, 94 (2010).
- [41] D. Brink, Ph.D. thesis, Oxford University, 1955 (unpublished).
- [42] P. Axel, Phys. Rev. **126**, 671 (1962).
- [43] M. Guttormsen *et al.*, Phys. Rev. Lett. **116**, 012502 (2016).
- [44] J. S. Levinger and H. A. Bethe, Phys. Rev. **78**, 115 (1950).
- [45] M. Guttormsen *et al.*, Phys. Rev. C **71**, 044307 (2005).
- [46] M. Wiedeking *et al.*, Phys. Rev. Lett. **108**, 162503 (2012).
- [47] A. C. Larsen *et al.*, Phys. Rev. Lett. **111**, 242504 (2013).

- [48] A. C. Larsen and S. Gorieli, Phys. Rev. C **82**, 014318 (2010).
- [49] J. J. Gaardhøje, Annu. Rev. Nucl. Part. Sci. **42**, 483 (1992).
- [50] K. A. Snover, Ann. Rev. Nucl. Part. Sci. **36**, 545 (1986).
- [51] A. Schiller and M. Thoennessen, Atom. Data Nucl. Data Tables **93**, 549 (2007).
- [52] J. N. Orce *et al.*, Phys. Rev. C **86**, 041303(R) (2012).
- [53] A. C. Larsen *et al.*, Phys. Rev. C **73**, 064301 (2006).
- [54] M. N. Harakeh and A. Woude, *Giant Resonances: Fundamental High-frequency Modes of Nuclear Excitation*, Oxford University Press (2001).
- [55] W. Bothe and W. Gentner, Z. Physik **3-4**, 236 (1937).
- [56] W. D. Myers *et al.*, Phys. Rev. C **15**, 6 (1977).
- [57] N. Frascaria, Nucl. Phys. A **569**, 111 (1994).
- [58] R. Bergère, (1976), Lecture Notes in Physics Vol. **61**, Springer-Verlag New York, Berlin, Heidelberg.
- [59] M. Baranger, E. Vogt, Adv. in Nucl. Phys. **7**, 229 (2012).
- [60] C. E. Porter and R. G. Thomas Phys. Rev. **104**, 483 (1956).
- [61] W. Hauser and H. Feshbach, Phys. Rev. **87**, 366 (1952).
- [62] E. M. Burbidge, G. R. Burbidge, W. A. Fowler, and F. Hoyle, Rev. Mod. Phys. **29**, 547 (1957).
- [63] J. Kopecky and M. Uhl, Phys. Rev. C **41**, 1941 (1990).
- [64] A. C. Larsen and S. Gorieli, Phys. Rev. C **82**, 014318 (2010).
- [65] J. Kopecky *et al.*, Phys. Rev. C **47**, 312 (1993).
- [66] J. Kopecky and M. Uhl, Report INDC(NDS)-335 (IAEA Vienna, 1935).
- [67] S. K. Kataria, V. S. Ramamurthy and S. S. Kapoor, Phys. Rev. C **18**, 549 (1978).
- [68] D. J. Griffiths, *Introduction to electrodynamics* 2nd edition, Prentice-Hall Inc. New Jersey (1989).
- [69] J. B. Marion, S. T. Thornton, *Classical dynamics of particles and systems*, 5th edition, Cengage Learning (2003).
- [70] N. F. Mott and I. N. Sneddon, *Wave Mechanics and its applications*, Oxford University Press, London (1948).
- [71] W. Knüpfner and A. Richter, Phys. Lett. B **107**, 325 (1981).
- [72] W. Knüpfner and A. Richter Z. Phys. A **320**, 253 (1985).
- [73] A. N. Andreyev *et al.*, Nature **405**, 430 (2000).

- [74] K. Alder and A. Winther, *Electromagnetic Excitation*, North-Holland, Amsterdam (1975).
- [75] M. Danos, Nucl. Phys. **5**, 23 (1958).
- [76] J. A. Kuehner *et al.*, Phys. Lett. B **115**, 437 (1982).
- [77] S. Goriely and E. Khan, Nucl. Phys. A **706**, 217 (2002).
- [78] E. Khan *et al.*, Nucl. Phys. A **694**, 103 (2001).
- [79] A. C. Larsen *et al.*, Phys. Rev. C **76**, 044303 (2007).
- [80] M. Guttormsen *et al.*, Phys. Rev. C **71**, 044307 (2005).
- [81] A. Schiller *et al.*, Nucl. Instr. Meth. Phys. Res. A **447**, 498 (2000).
- [82] M. Guttormsen *et al.*, Nucl. Instr. Meth. Phys. Res. A **255**, 518 (1987).
- [83] A. Simon *et al.*, Phys. Rev. C **93**, 034303 (2016).
- [84] M. Weideking *et al.*, Phys. Lett. **108**, 162503 (2012).
- [85] A. C. Larsen *et al.*, J. Phys. G **44**, 064005 (2017).
- [86] M. D. Jones *et al.*, Phys. Rev. C **97**, 024327 (2018).
- [87] E. Litvinova and N. Belov, Phys. Rev. C **88**, 031302(R) (2013).
- [88] R. Schwengner, S. Frauendorf and A. C. Larsen, Phys. Rev. Lett. **111**, 232504 (2013).
- [89] R. Schwengner *et al.*, Phys. Rev. C **66**, 024310 (2002).
- [90] U. Agvaanluvsan, A. C. Larsen, R. Chankova, M. Guttormsen, G. E. Mitchell, A. Schiller, S. Siem, and A. Voinov, Phys. Rev. Lett. **102**, 162504 (2009).
- [91] N. Pietralla *et al.*, Phys. Rev. Lett. **83**, 1303 (1999).
- [92] C. Fransen *et al.*, Phys. Rev. C **67**, 024307 (2003).
- [93] B. A. Brown and A. C. Larsen, Phys. Rev. Lett. **113**, 252502 (2014).
- [94] K. Sieja, Phys. Rev. Lett. **119**, 052502 (2017).
- [95] K. Sieja, EPJ Web of Conferences **146**, 05004 (2017).
- [96] A. C. Larsen *et al.*, Phys. Rev. C **97**, 054329 (2018).
- [97] J. S Levinger, Annu. Rev. Nucl. Sci. **4**, 13 (1954).
- [98] E. Hayward, *Photonuclear Reactions*, National Bureau of Standards Monograph 118, Washington D.C (1970).
- [99] A. Fasso, Nuclei and Atoms (Numerical Data and Functional Relationships in Science and Technology), Springer-Verlag, Vol 11 (1990).

- [100] H. Bethe and W. Heitler, Proceedings of the Royal Society A **146**, 83 (1934).
- [101] C. Tzara, C. R. Academy of Science **56**, 245 (1957).
- [102] W. S. Francis, M. W. Zamansky and H. D. Young, University Physics, 6th ed., Addison-Wesley (1981).
- [103] <https://www-nds.iaea.org/exfor/exfor.htm>
- [104] <https://www.nndc.bnl.gov/ensdf/>
- [105] https://tendl.web.psi.ch/tendl_2015/tendl2015.html
- [106] <http://www.mn.uio.no/fysikk/english/research/about/infrastructure/OCL/nuclear-physics-research/compilation/>
- [107] M. Guttormsen *et al.*, Phys. Rev. C **68**, 064306 (2003).
- [108] A. Vessiere *et al.*, Nucl. Phys. A **227**, 513 (1974).
- [109] A. C. Larsen *et al.*, Phys. Rev. C **76**, 044303 (2007).
- [110] K. Shoda, Nucl. Phys. A **239**, 397 (1975).
- [111] S. C. Fultz *et al.*, Phys. Rev. **128**, 2345 (1962).
- [112] S. S. Borodina *et al.*, Moscow State Univ. Inst. of Nucl. Phys. Rep., 6 (2000).
- [113] P. Carlos *et al.*, Nucl. Phys. A **258**, 365 (1976).
- [114] A. Spyrou *et al.*, Phys. Rev. Lett. **113**, 232502 (2014).
- [115] B. L. Berman *et al.*, Phys. Rev. **162**, 1098 (1967).
- [116] M. Guttormsen *et al.*, Phys. Rev. C **96**, 024313 (2017).
- [117] H. Utsunomiya *et al.*, Phys. Rev. Lett. **100**, 162502 (2008).
- [118] H. Beil *et al.*, Nucl. Phys. A **227**, 427 (1974).
- [119] H. Utsunomiya *et al.*, Phys. Rev. C **88**, 015805 (2013).
- [120] H. Beil *et al.*, Nucl. Phys. A **172**, 426 (1971).
- [121] B. V. Kheswa *et al.*, Phys. Lett. B **744**, 268 (2015).
- [122] P. Carlos *et al.*, Nucl. Phys. A **225**, 171 (1974).
- [123] A. C. Larsen *et al.*, Phys. Rev. C **87**, 014319 (2013).
- [124] V. V. Balashov, J. Exptl. Theoret. Phys. U.S.S.R. **42**, 275 (1962).
- [125] M. Baldo and G. F. Burgio, Prog. in Part. and Nucl. Phys. **91**, 203 (2016).
- [126] C. J. Horowitz, E. F. Brown *et al.*, Nucl. Part. Phys. **44**, 9 (2014).
- [127] J. Tian, H. Cui, K. Zheng, and N. Wang, Phys. Rev. C **90**, 024313 (2014).

- [128] M. Wang, G. Audi, A. H. Wapstra, F. G. Kondev, M. MacCormick, X. Xu, and B. Pfeiffer, *Chin. Phys. C* **36**, 1603 (2012).
- [129] B. L. Berman and S. C. Fultz, *Rev. Mod. Phys.* **47**, 73 (1975).
- [130] J. de Boer and J. Eichler, *Adv. Nucl. Phys.* **1**, 1 (1968).
- [131] P. Argan *et al.*, *Nucl. Inst. Meth.* **228**, 20 (1984).
- [132] Ph. Catillon, *Lecture Notes in Physics* **108**, 201 (1979).
- [133] <http://irfu.cea.fr/dphn/en/index.php>

